

## **THÈSE**

Pour obtenir le grade de

**DOCTEUR DE la Communauté UNIVERSITÉ  
GRENOBLE ALPES**

Spécialité : **Physique de la Matière Condensée et du Rayonnement**

Arrêté ministériel : 7 Août 2006

Présentée par

**Andrea CORNA**

Thèse dirigée par **Marc SANQUER**  
et codirigée par **Xavier JEHL**

préparée au sein **du laboratoire de transport électronique quantique et supraconductivité,**  
**du service de photonique électronique et ingénierie quantiques,**  
**de l'institut nanosciences et cryogénie,**  
**du CEA Grenoble**  
et de **l'école doctorale de physique de Grenoble**

# **Single Spin control and readout in silicon coupled quantum dots**

Thèse soutenue publiquement le **20 Janvier 2017**,  
devant le jury composé de :

**Hervé COURTOIS**

Université Grenoble Alpes et Institut Néel/CNRS, Président

**Gwendal FÈVE**

Laboratoire Pierre Aigrain/ENS Paris, Rapporteur

**Dominique MAILLY**

Centre de Nanosciences et de Nanotechnologies/CNRS et Université Paris-Sud,  
Rapporteur

**Marc SANQUER**

PHELIQS/INAC/CEA et Université Grenoble Alpes, Directeur de thèse

**Xavier JEHL**

PHELIQS/INAC/CEA et Université Grenoble Alpes, Invité





A Salha





# Abstract/Résumé

## Abstract

In the recent years, silicon has emerged as a promising host material for spin qubits. Thanks to its widespread use in modern microelectronics, silicon technology has seen a tremendous development. Realizing qubit devices using well-established complementary metal-oxide-semiconductor (CMOS) fabrication technology would clearly favor their large scale integration. In this thesis we present a detailed study on CMOS devices in a perspective of qubit operability. In particular we tackled the problems of charge and spin confinement in quantum dots, spin manipulation and charge and spin readout.

We explored the different charge and spin confinement capabilities of samples with different sizes and geometries. Ultrascaled MOSFETs show Coulomb blockade up to room temperature with charging energies up to 200 meV. Multigate devices with larger geometrical dimensions have been used to confine spins and read their states through spin-blockade as a way to perform spin to charge conversion. Spin manipulation is achieved by means of Electron Dipole induced Spin Resonance (EDSR). The two lowest valleys of silicon's conduction band originate as intra and inter-valley spin transitions ; we probe a valley splitting of 36  $\mu$ eV. The origin of this spin resonance is explained as an effect of the specific geometry of the sample combined with valley physics and Rashba spin-orbit interaction. Signatures of coherent Rabi oscillations have been measured, with a Rabi frequency of 6 MHz. We also discuss fast charge and spin readout performed by dispersive gate-coupled reflectometry. We show how to use it to recover the complete charge stability diagram of the device and the expected signal for an isolated double dot system. Finite bias changes the response of the system and we used it to probe excited states and their dynamics.

## Résumé

Au cours des dernières années le silicium est apparu comme un matériau hôte prometteur pour les qubits de spin. Grâce à la microélectronique moderne, la technologie du silicium a connu un formidable développement. Réaliser des qubits utilisant la technologie bien établie de fabrication CMOS de semi-conducteurs favoriserait clairement leur intégration à grande échelle. Dans cette thèse nous présentons les travaux effectués dans une perspective des qubits CMOS. En particulier, nous avons abordé les problèmes de confinement des charges et des spins dans les boîtes quantiques, la manipulation des spins et la lecture des charges et des spins.

Nous avons exploré les différentes propriétés de confinement de charge et de spin dans des échantillons de tailles et de géométries différentes. Les MOSFETs de taille extrêmement réduites montrent du blocage de Coulomb jusqu'à température ambiante, avec des énergies de charges jusqu'à 200 meV. Les dispositifs multi-grilles avec des dimensions géométriques plus grandes ont été utilisés pour confiner les spins et lire leur état par blocage de spin, en réalisant ainsi une conversion spin / charge. La manipulation des spins est réalisée au moyen d'un dipôle électronique induisant la résonance de spin (EDSR). Les deux plus basses vallées de la bande de conduction du silicium sont visibles sous forme de transitions de spin intra et inter-vallées. Nous observons une levée de dégénérescence de vallée d'amplitude 36  $\mu$ eV. La résonance de spin que l'on observe résulte de la géométrie spécifique de l'échantillon, de la physique des vallées et de l'interaction spin-orbite de type Rashba. Des signatures de manipulation cohérente, sous forme d'oscillations de Rabi, ont été mesurées, avec une fréquence de Rabi de 6 MHz. Nous discutons également de la lecture rapide des charges et des spins effectuée par réflectométrie dispersive couplée à la grille. Nous montrons comment l'utiliser pour reconstruire le diagramme de stabilité de charge du dispositif et le signal attendu pour un système à double boîte isolé. La tension de polarisation finie modifie la réponse du système et nous l'avons utilisée pour sonder les états excités et leur dynamique.

# Contents

<b>Introduction</b>	<b>1</b>
<b>1 Single Electron Transistor from low to Room temperature</b>	<b>5</b>
1.1 Devices fabrication . . . . .	6
1.2 Results . . . . .	8
1.2.1 Single dot device . . . . .	8
1.2.2 Double dots device . . . . .	12
1.3 Role of surface roughness . . . . .	14
1.4 Conclusions . . . . .	16
<b>2 Spin manipulation</b>	<b>17</b>
2.1 Device . . . . .	17
2.1.1 RF antenna . . . . .	19
2.1.2 Selection . . . . .	26
2.2 Setup and device connection . . . . .	30
2.3 Stability diagram and bias spectroscopy . . . . .	32
2.4 Magneto-transport and spin blockade . . . . .	35
2.4.1 Spin blockade theory . . . . .	35
2.4.2 Lifting of spin blockade . . . . .	38
2.4.3 Magnetotransport measurements . . . . .	42
2.5 Electron Dipole-induced Spin Resonance . . . . .	45
2.5.1 Relaxation phenomena and Bloch equations . . . . .	48
2.5.2 Continuous-Wave Spin Resonance . . . . .	48
2.6 Spin-Valley Resonance . . . . .	56
2.6.1 Spin-valley blockade . . . . .	61
2.7 Towards coherent control with EDSR . . . . .	63
2.7.1 Setup and calibration . . . . .	65
2.7.2 Results . . . . .	68

2.8	Origin of EDSR . . . . .	68
2.8.1	Permanent magnetism . . . . .	68
2.8.2	Spin-Orbit and Valley mixing modelling . . . . .	69
2.8.3	Tight-binding results . . . . .	73
2.9	Conclusions . . . . .	75
<b>3</b>	<b>Reflectometry - Dual-channel gate dispersive readout</b>	<b>77</b>
3.1	Device and measurement setup . . . . .	78
3.2	Dispersive readout signal . . . . .	80
3.3	Results . . . . .	81
3.4	Modeling of out-of-equilibrium response . . . . .	82
3.5	Conclusions . . . . .	87
	<b>Conclusions</b>	<b>89</b>
	<b>Bibliography</b>	<b>93</b>
	<b>Appendix A Device fabrication</b>	<b>105</b>
A.1	Fabrication steps . . . . .	105
A.2	E-beam/DUV hybrid lithography . . . . .	110
	<b>Appendix B Device selection</b>	<b>113</b>
B.1	Probe station . . . . .	116

# Introduction

In recent years quantum computing has gone through a massive development and widespread interest. The key element of an architecture for a quantum computer is the qubit, the quantum analogous of the classical boolean bit. In these thesis we will study some key technologies and phenomena to possibly build a qubit in a scalable silicon spin quantum architecture. In particular we will analyze the aspect of spin and charge confinement, manipulation and read-out.

Recently several quantum computer architectures have been proposed and realized. The point is to find materials and engineer a system where qubit can be physically realized, initialized, controlled, read and coupled together to implement quantum algorithms on top of them. Due to the intrinsically probabilistic nature of quantum mechanism and unavoidable decoherence phenomena, error correction is an import part of an architecture to obtain a fault-tolerant computation. A qubit is essentially a quantum two-level system, so any system in which we can select a subset of level, initialize to a known state, manipulate and read is a possible candidate. Possible candidate are the polarization of a photon [1], the spin of an electron [2] or a nucleus [3], a charge position [4], magnetic flux [5] or many others. All these system can live on a different platform, like trapped ions [6], molecules probed by Nuclear Magnetic Resonance [7], superconducting circuits, color centers in diamonds, dopants or quantum dots in semiconductors.

Solid states system have the great advantage to make possible the realization of very compact qubits and possibly scalable architectures. Superconducting qubits[8] have achieved great advancements in terms of coherence time, fidelity and scalability[9], realizing also quantum computer prototypes with few qubits [10, 11].

Another promising architecture is represented by spin qubits in semiconductors. qubits are made by one or more spins confined in a quantum dot or a dopant in a semiconducting substrate. The size of these objects is very small, thus enabling a large scaling needed for a real quantum computer. Moreover the semiconductor technologies developed for micro and nano electronics provides an advanced and well-established technological platform.

Early experiments have been performed in lateral quantum dots in GaAs/AlGaAs heterostruc-

tures [12–14]. Two-dimensional electron gas in Gallium-arsenide quantum-well has a great electron mobility and low-electron density, so it's easy to locally deplete the gas and define very tunable quantum dots [15]. However, gallium and arsenic have a non-zero nuclear spin, so thought hyperfine interaction with the trapped electron, they induce decoherence.

By contrast silicon has a much lower concentration of non-zero nuclear spins and it can be isotopically purified to achieve extremely long coherence times [16]. Moreover there is a larger knowledge and technology available for the fabrication, thanks to the development in the microelectronic industry. On this purpose we recently realized the first qubit employing a CMOS (Complementary Metal-Oxide-Semiconductor) industry-standard fabrication process [17]. This paved the road for a possible integration with driving and readout electronics on-chip [18]

The goal of this thesis is to study and develop the building blocks to realize a quantum computer in a silicon CMOS platform. In particular, we focused on the aspect needed to realize a single qubit using MOSFET-like structures made with the Trigate Silicon-On-Insulator technology [19]. In this manuscript we investigate how to create silicon quantum dots of different sizes and confine charges. We will look also how to bound and probe a specific spin with spin blockade and how to rotate the spin orientation with Spin Resonance. Finally we explore how to probe the charge and spin states through dispersive readout with the goal of a fast readout.

Contrary to the qubit reported in [17] which employs the spin of an hole, we will focus on the electron spin. The behavior of electrons in silicon have been intensively studied [20] and their physics is well known. On the contrary holes have been investigated less and building good low-temperature devices is more challenging [21, 22]. Their small mobility leads to an higher sensibility to surface roughness and the higher Spin-Orbit Interaction can increase the coupling to charge noise.

## Contents

In chapter 1 we will investigate the behavior of ultrascaled silicon MOSFET. We present the peculiarities of the fabrication process to achieve very small dimension and the room-temperature pre-characterization process. We study the electrical behavior in a wide range of temperature, from room temperature down to 300mK. The different confinement mechanisms are investigated and a model is proposed. Coulomb blockade with large charge energies is obtained for system with one or two dots in series, in selected cases even up to room temperature.

In chapter 2 we investigate spin manipulation through spin resonance. We show a sample geometry tailored for this purpose and how mass-characterize it at room-temperature. We simulate the microwave behavior of the on-chip antenna and how it can be used to drive spin resonance. Low temperature measurement are used to investigate spin blockade as a way for spin initialization and readout. We show signature of spin resonance and the effect of the valleys in the silicon conduction band. A theoretical model with numerical simulation is presented to explain the origin of the resonance signal. Selected measurement of a possible coherent spin manipulation (Rabi oscillation) are also presented.

Finally in chapter 3 we study gate coupled dispersive readout as a mean to perform sensitive readout of a double dot system. We explain how dispersive readout works, how to implement it and what it probes. We show charge stability diagram of the double dot system and all the charge transitions that take places. A model to explain the specific features of the recorded lineshapes is proposed. We employs this model to derive the charge dynamics and the relaxation rates between excited and ground state.

In appendix A we show the Trigate fabrication process. We explain its peculiarities and the modifications in the process flow to tailor it for quantum devices.

In appendix B we briefly explain the room-temperature selection process and the semi-automatic probe-station used for that purpose.





# Chapter 1

## Single Electron Transistor from low to Room temperature

The quest for electronic circuits using single atoms and molecules took off with the rise of nanosciences. Atom switch [23], single atom contact [24], single atom transistor [25–28, 20] are various examples of nanodevices where the electric current is driven through the atomic orbitals of a weak link in an elementary circuit. Despite proof of concept demonstrations, these objects still suffer from many drawbacks: they are very fragile and their interfacing to the macroscopic world is extremely challenging. Most of them can hardly be integrated into standard, scalable semiconductor processes, and reveal their atomic properties only at low temperature.

On the other hand, reliable silicon CMOS transistors become smaller and smaller. The most advanced design to date is the nanowire (NW) CMOS transistor which consists of an etched quasi-one dimensional undoped silicon channel covered by a gate and connected to the heavily doped source and drain contacts. Nanowire transistors have better immunity to short-channel effects than Fin-FET and planar transistors thanks to the very good electrostatic control of the channel by the gate. Because this NW transistor benefits from the maturity of silicon processing and technology, it is attractive to use it as a platform for a room temperature single artificial atom (AA) transistor, i.e. a tiny channel where carriers are strongly confined in all 3 dimensions and controlled one-by-one by gates. Such AA shall display the excellent features inherited from the CMOS fabrication: established technology with no use of an expensive electron beam lithography, standardization and mass production, steady improvement in materials and processes, etc.

Here we present such an artificial atom transistor, tunable with a combination of top gate and backgate voltages, for which the atomic-like features can be tracked continuously from low to room temperature. This CMOS artificial atom exists in both  $n$ - and  $p$ -type transistors.

The design combines small diameter channel (3.4 nm) and long (25 nm) spacers separating the gate (G) from the heavily doped source (S) and drain (D) electrodes, in order to enhance confinement and Coulomb interactions. Despite the very small size of these artificial atoms (a few nanometers) the fabrication is massively parallel. Although the process variability is large at this scale, several working samples have been already produced. This chapter is an extract of our article “Quantum dot made in metal oxide silicon-nanowire field effect transistor working at room temperature” [29].

## 1.1 Devices fabrication

Top-down silicon NWs [30] as well as Chemical Vapor Deposition (CVD) grown silicon nanowires [31, 32] have both reached the 2 to 8 nm diameter range. These devices show strong transverse confinement thanks to the small cross-section of the NW. Isolation from the S-D contacts by longitudinal confinement is then the key to reach the AA regime where the interplay between Coulomb blockade and quantum confinement regulates the addition spectrum. For CVD grown silicon NWs, the S-D contacts are usually Schottky barriers between metallic electrodes and the nanowire [32, 33]. Here instead of Schottky contacts we used highly doped silicon contacts (source and drain), and decoupled them from the channel by introducing 25 nm long intrinsic silicon nanowire spacers (non-overlapped S-G geometry). These spacers play the role of long linker molecules in single atom transistors [25]. The transmission through the spacers can also be controlled by the substrate bias. A quantum dot is formed below the gate by the electric field, and it accumulates electrons (or holes) [34, 35]. Overall, these spacers present several advantages. First, they preserve the electrostatic control over the channel – and therefore the AA tunability – even at short gate lengths (10 nm). Second, they limit the screening of the electron interactions by the S-D electrodes. Third, they prevent the lateral diffusion of source and drain dopants in the channel. Fourth, it has been shown that long and thin resistors are more efficient than thin tunnel barriers to prevent parasitic cotunneling in metallic single electron transistors [36]. This is reminiscent of using quantum point contacts [37] or resistive circuits [38] in order to observe charging effects and Coulomb blockade [39].

Specifically, our AAs are made in thin ( $\approx 3.4$  nm diameter) etched nanowires (see figure 1.1). An omega-shaped gate ( $\Omega$ -gate) sets the transverse electric field locally. The fabrication process is similar to the one explained in appendix A. E-beam lithography has not been employed, only standard DUV 193 nm deep-UV (DUV) lithography has been used. Following the nanowire patterning, a resist trimming process is performed in order to reduce the NW width down to 10 nm. A 7 nm thick oxidation further reduces their diameter down to

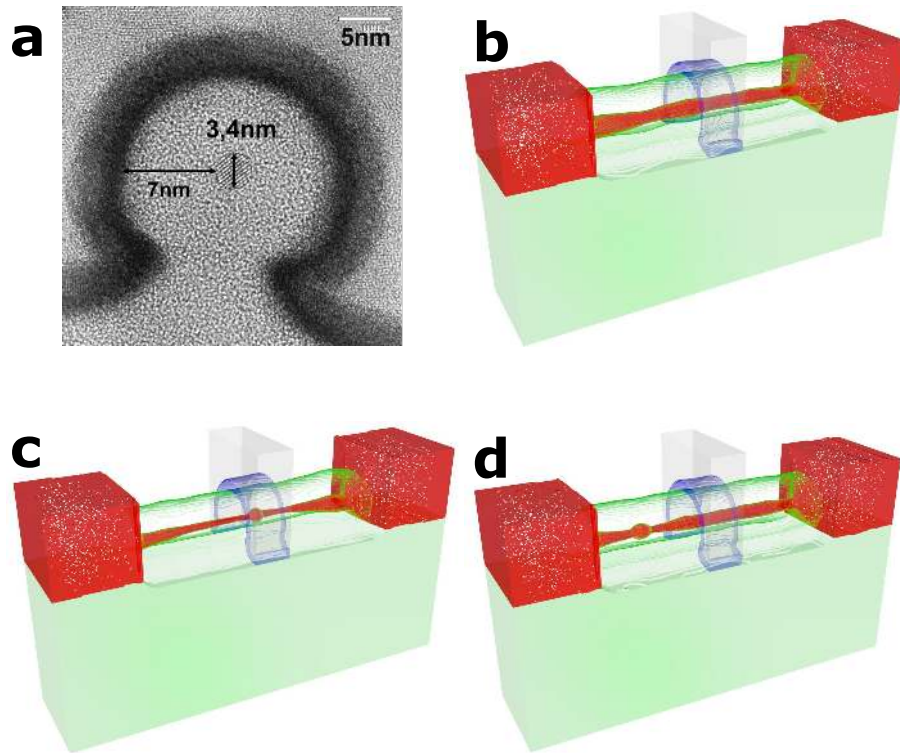


**Figure 1.1 Geometry, simulations** a) TEM image showing the cross section of the 3.4 nm diameter silicon nanowire, the 7 nm thick SiO<sub>2</sub> gate oxide, the 1.9 nm HfSiON and the 5 nm ALD TiN/poly Silicon gate. b-d) Models used for the simulations b) A *n*-type device with moderate surface roughness (wire diameter 3.4 nm; surface roughness rms  $\Delta = 0.25$  nm). Silicon is in red, SiO<sub>2</sub> in green, HfO<sub>2</sub> (HfSiON) in blue, TiN gate in grey, Si<sub>3</sub>N<sub>4</sub> otherwise. The silicon substrate is not represented. The white dots are arsenic donors in the source and drain. This device has a charging energy around 90 meV. c) A *n*-type device with strong surface roughness including a 4 nm long dot under the gate. d) A *p*-type device with strong surface roughness including a 7 nm long dot under the source spacer, and a very long, ~30 nm long dot under the gate and drain spacer.

$\approx 3.4$  nm and protects the wires for the rest of the fabrication. Pattern edge roughness becomes increasingly important as the features become smaller. The line-edge and line-width roughness of the patterns directly result from the initial roughness of the resist. This is significant after resist trimming, with the formation of several constrictions and possibly quantum dots. Other fabrication steps are identical. Devices are simple MOSFET structures with only one gate. Spacers are 25 nm long.

This integration scheme based on a CMOS process allows for an easier implementation of contacts, spacers, top and bottom gates – all crucial building blocks of a reliable artificial atom. Although room temperature single electron transistors have already been reported in

small silicon structures [40–43] and have been constantly improved up to date [30, 44], none of the previous demonstrations used standard CMOS integration and – with the exception of Ref. [45] – all of them were fabricated with e-beam lithography.

Figure 1.1a shows a TEM image of the cross-section of a device while Figs. 1.1b-d show structural models used for electrical simulations. The line-edge roughness of the patterns is critical at this scale and directly results from the initial roughness of the resist (see figure S1 in the supporting information). Figs. 1.1b-d are therefore possible scenarios for the experimental data discussed below: a moderate surface roughness disorder (b); and a strong surface roughness defining a quantum dot either below the gate (c) or below the spacers (d).

## 1.2 Results

We present here the results of two different measured samples. Both of the devices shows room-temperature oscillations. The first one is a *n*-MOS device; as explained it shows a single dot behaviour at all temperatures. The second one is a *p*-MOS device, which shows a double-dot behaviour at low temperature.

### 1.2.1 Single dot device

The linear S-D conductance of this device is plotted in Figure 1.2a at various temperatures between 4.2 K and 300 K. Here five resonances can be identified at  $V_{g,i} \approx 0.7$  V, 1.0 V, 1.2 V, 1.37 V and 1.45 V ( $i = 1 - 5$ ).

The effect of the back gate (see figure 1.2b) is qualitatively simple: the resonances are simply shifted in gate voltage as the substrate bias is varied but they are not suppressed. A modulation of the amplitude of  $I_{ds}$  is also observed, which can be due to the ionization of a coupled impurity [46]. Yet, lines of finite conductance in the  $I_{ds}$  versus  $(V_g, V_b)$  plot are characteristic of the transport through a single AA, and not of two dots in series (which would lead to discrete triple points or more complicate patterns). Furthermore the AA resonances in the *n*-type sample have a large  $\alpha_g = 0.75$  (determined from the  $I_{ds}(V_g, V_d)$  plot in figure 1.2c). Therefore, we conclude that this AA is below or very near the top gate, as in figure 1.1c.

The first resonance at  $V_{g,1} = 0.7$  V carries a small resonant current at 300 K and no more detectable current below  $T = 200$  K. Thus, this first electron state is weakly tunnel coupled to the source and to the drain. At room temperature thermal activation of carriers increases the transmission through the nanowire under the spacers, which remains compatible with Coulomb blockade as shown in Ref. [37]. The resonances at larger  $V_g$  become increasingly

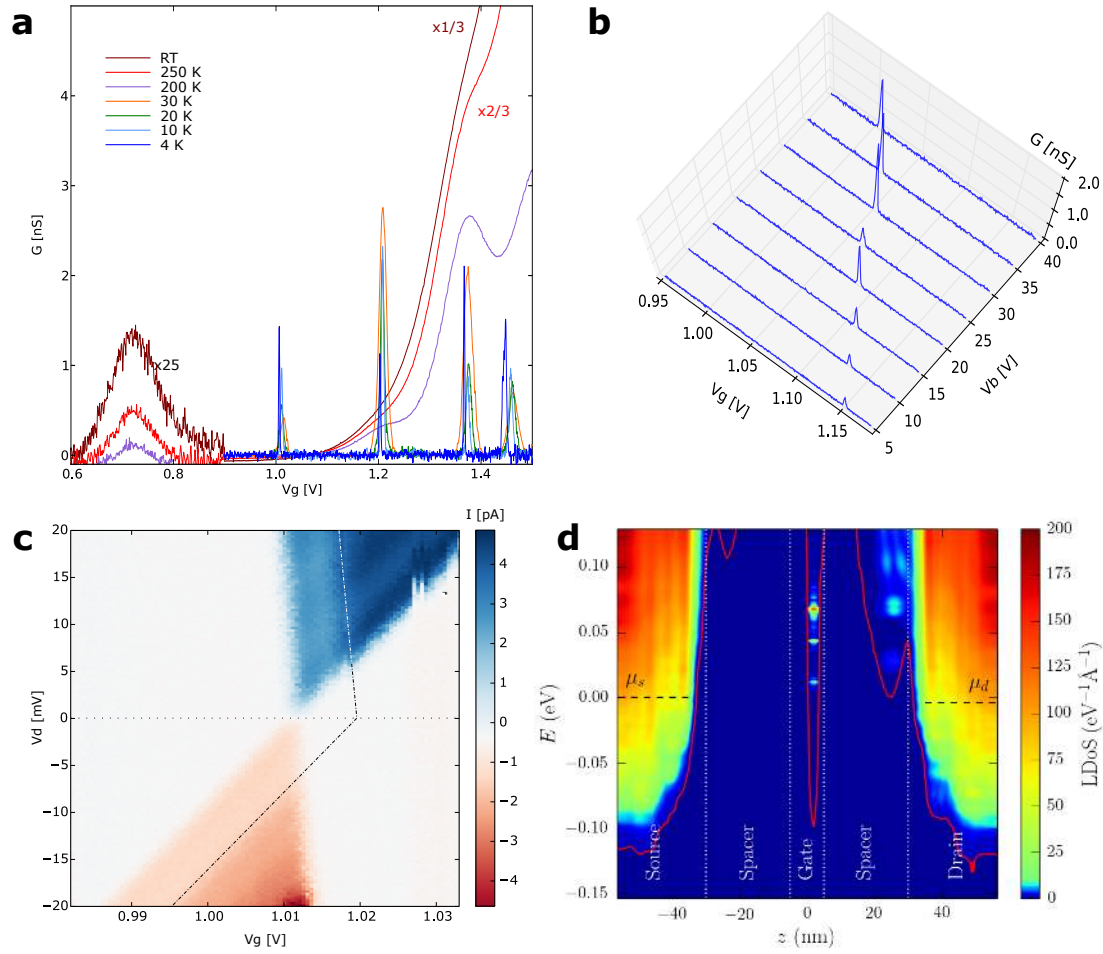


**Figure 1.2 Conductance characteristics and Coulomb oscillations for a *n*-type sample** a) Temperature dependence of  $G(V_g) = \frac{\delta I_{ds}}{\delta V_d}$  at  $V_b = 40$  V. A first resonance appears at 300 K near  $V_g = 0.7$  V. Only four resonances are identified at  $T = 4.2$  K in this  $V_g$  range. b)  $I_{ds}(V_g, V_b)$  at  $T = 4.2$  K around the second resonance. No triple point – as in figure 1.4 – but a single line appears in the  $I_{ds}(V_g, V_b)$  plot, which is indicative of a single dot. c)  $I_{ds}(V_g, V_d)$  at  $T = 4.2$  K around the second resonance. The first excited state (dashed-dotted line) appears 5 meV above the ground state for the resonance near  $V_g = 1$  V. The lever arm parameter is  $\alpha_g = 0.75$ . The large  $\alpha_g$  confirms that the AA is centered under the top gate. d) Simulation of the confinement potential and Local Density of States (LDoS) in a *n*-type sample with a  $\sim 4$  nm long dot (the AA) under the gate. The red line is the potential landscape in the channel, while the horizontal, black dashed lines are the Fermi levels in the source ( $\mu_s$ ) and drain ( $\mu_d$ ). Three quasiparticle states can be resolved in the dot under the gate.

sharper as the temperature decreases. The peaks at  $V_g = 1.0$  V, 1.2 V, and 1.37 V have similar width at different temperatures but the value of the conductance  $G_i^{res}$  at resonance as well as

its temperature dependence varies from peak to peak. Below  $T = 30$  K,  $G_i^{res}$  is given by:

$$G^{res}(V_g) \approx \frac{e^2}{4k_B T} \frac{\Gamma_s \Gamma_d}{\Gamma_s + \Gamma_d}, \quad (1.1)$$

where  $\Gamma_{s(d)}$  is the tunneling rate to the source (drain), and the full width at half maximum of the resonance is given by  $3.52 \frac{k_B T}{e\alpha_g}$ , which is characteristic of a thermally broadened resonant tunneling regime.

The resonance near  $V_{g,2} = 1.0$  V can be well fitted by a thermally broadened resonant tunneling lineshape (see figure 1.3):

$$G_2(V_g) \approx \frac{e^2}{4k_B T} \frac{\Gamma_{s,2} \Gamma_{d,2}}{\Gamma_{s,2} + \Gamma_{d,2}} \cosh^{-2} \left( \frac{\alpha_g e (V_g - V_{g,2})}{2k_B T} \right) \quad (1.2)$$

The full width at half maximum (FWHM) is hence set by the effective electronic temperature whatever the tunneling rates  $\Gamma_{s(d),2}$  ( $\text{FWHM} \approx 3.52 \frac{k_B T}{e\alpha_g}$ ). The fitted electronic temperature is 5.8 K (resp. 10.4 K, 21.8 K, 32.6 K) at  $T = 4.2$  K (resp. 10 K, 20 K, 30 K). The shift of the peak with  $V_g$  ( $e\alpha_g \Delta V_g \simeq k_B T$ ) between 4.2 K and 30 K has been explained in Ref. [47] for spin-degenerate states (with different  $\Gamma_{s,2}$  and  $\Gamma_{d,2}$ ). The resonant conductance  $G_2^{res}$  is consistent with  $\Gamma_{s,2} \simeq 18$  MHz  $\ll \Gamma_{d,2}$ .

For  $i \geq 3$  the temperature dependence of  $G_i^{res}$  is non-monotonic between  $T = 4.2$  K and  $T = 30$  K, pointing out the contribution of a nearby, thermally accessible excited state to the resonant conductance, or to the temperature dependence of the tunneling rates. At higher temperature (200 K-300 K) a quasi continuum of states becomes accessible and contributes to the drain current at large  $V_g$ . Equivalently the tunnel rates strongly increase with temperature. This is not the case for the resonances near  $V_{g,2} = 1.0$  V and  $V_{g,3} = 1.2$  V, so that the conductance is larger by several orders of magnitude at 4.2 K than at 300 K for these peaks. The addition energy of the one-to-two (resp. two-to-three, three-to-four, four-to-five) electrons in the channel is 230 (resp. 150, 130, 60) meV taking into account the lever arm parameter  $\alpha_g = 0.75$ .

Simulations confirm this scenario. Figure 1.2d shows the local density of states (LDoS) computed in the  $n$ -type device of figure 1.1c, near the gate voltage where the first electron tunnels into the dot. The calculation was performed for  $T = 150$  K because at lower temperatures some of the resonances become too narrow to be accurately resolved by the NEGF solver. There is only one, 4 nm long and diameter dot located near the center of the channel. The dot is isolated from the bulk source and drain by lateral confinement within the spacers and by the dielectric mismatch between the nanowire and the embedding oxides (image charge self-energy corrections). Indeed both raise the conduction band of the wire

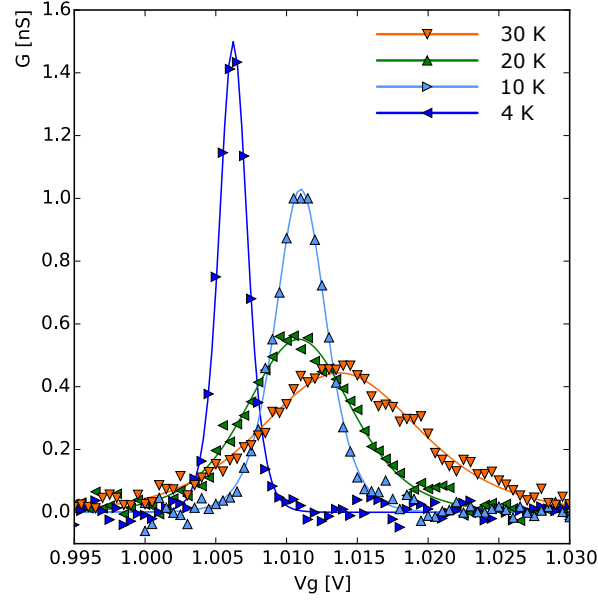


Figure 1.3 Temperature dependence of the resonance near  $V_{g,2} = 1.0$  V in the  $n$ -type sample. The symbols are the experimental points. The solid lines are the fits by the thermally broadened resonant tunneling theory (effective electron temperature as the fit parameter, see text).

well above the Fermi level of the contacts (the barrier is up to 300 meV high). Three well resolved energy levels can be identified inside the dot. The calculated addition energy for the second electron is  $U = 196$  meV. The dot is well coupled to the gate, the lever arm parameter  $\alpha_g = 0.83$  being close to the experimental one (0.75).

Simulations show that the orbital excitation in the channel always lie more than 15 meV above the ground state even in the absence of SR. Yet transport spectroscopy at finite  $V_d$  reveals a single excited state at  $V_d \simeq 5$  meV as a plateau of current for both polarities (see figure 1.2c). The separation between the ground and the first excited state (5 meV) is therefore much smaller than the calculated splitting between the orbital excitation. Consequently, the first excited state observed in figure 1.2c is most likely the valley orbit split ground orbital level in the AA. Indeed, the calculated valley-orbit splitting of the ground state resonance is strongly dependent on the shape of the dot and can range from a few to a few tens of meV.

In our samples a very good transmission through the 25 nm long spacers can be achieved for any temperature by adjusting the back gate voltage. The fact that the resonant current at  $T = 4.2$  K is comparable to the current measured at 300 K proves that any parasitic stochastic Coulomb blockade effect can be eliminated in our devices by a proper choice of the control voltages. In contrast to our results for the  $n$ -type sample, Shin *et al.* [48] have observed current resonances at room temperature which, however, split into multiple peaks at low

temperature. Furthermore, the current at the resonances decreases as the temperature is reduced. The regular pattern of split peaks and their drain voltage dependence can be attributed (a) to the effect of valley splitting of orbital levels [30], (b) to a possible parasitic effect due to granularity in the gate stack [49] or (c) to the appearance of multiple dots in series.

### 1.2.2 Double dots device

We present now a sample with a double-dot behaviour. In figure 1.4a we report the linear  $I_{ds} - V_g$  characteristics measured at various temperatures in a  $p$ -MOS device with a small drain current. A broad resonance can be resolved at 300 K, and splits in two sharp resonances at  $T = 4.2$  K. In figure 1.4a, the back gate voltage  $V_b$  has been adjusted in order to recover a high resonant current at low temperature – otherwise the current decreases by orders of magnitude between  $T = 77$  K and  $T = 4.2$  K. Such a decrease of the current is also visible in Ref. [30] and Ref. [43], where no back gate bias was applied. The splitting of the resonance and decrease of the current suggest the presence of two dots in series. The detuning (level misalignment) between the two dots results in a suppression of current at low temperature, unless the levels are properly realigned by the back gate electric field. This hypothesis is confirmed by the  $I_{ds}(V_g, V_b)$  plot on figure 1.4b, where the current appears in a sequence of coupled triple points. The charging energy  $U$  of these dots and lever arm parameter to the gate  $\alpha_g = \frac{\delta\Phi}{\delta V_g}$  ( $\Phi$  being the potential in the dot) can be determined from the  $I_{ds}(V_g, V_d)$  plots. The larger is  $\alpha_g$ , the stronger is the electrostatic coupling between the dot and the top  $\Omega$ -gate. One of the dots has a charging energy  $U \simeq 60$  meV and a lever arm parameter  $\alpha_g \simeq 0.47$ . This dot is presumably located near the top gate [34, 35]. The other dot – the AA – has a larger charging energy  $U \simeq 140$  meV and a smaller  $\alpha_{g,AA} \simeq 0.34$ . It is likely located under a spacer and is induced by enhanced surface roughness.

In order to validate this scenario, we have calculated the charging energies and lever arm parameters of quantum dots with different sizes and positions along the nanowire. Figure 1.4d shows the LDoS computed in the device of figure 1.1d, which is the only geometry found that reproduces the overall experimental picture. In this device, we have introduced two constrictions under the source spacer that delimit a 4 nm diameter and 7 nm long dot (the AA), while a much longer dot extends from the gate to the drain spacer. The position and size of this 7 nm dot have been chosen to match the experimental charging energy and lever arm parameter of the AA. The other long dot results from random, gaussian surface roughness with rms  $\Delta = 0.25$  nm. Its charging energy is  $U \simeq 45$  meV, and its lever arm parameter is greater than 0.6, which suggests that the experimental accumulation dot is a little shorter on the gate side. There is one well defined resonance in the AA (the excited state being almost 50 meV below), and a few broader resonances in the long dot. The long



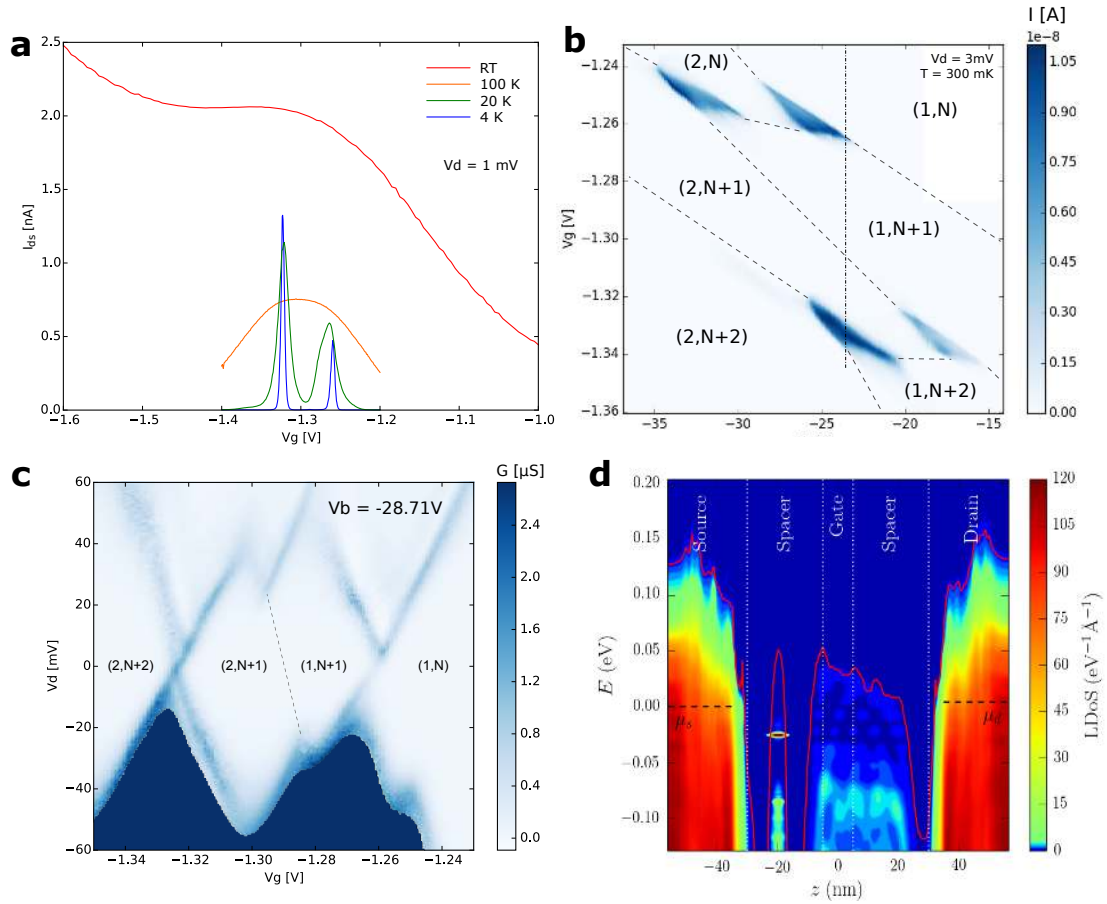


Figure 1.4  $I_{ds}(V_g)$  characteristics and Coulomb oscillations for a p-type sample. a) Temperature dependence of  $I_{ds}(V_g)$  ( $V_d = 1$  mV). The resonance near  $V_g = -1.3$  V at  $T = 300$  K splits in two resonances at  $T = 4.2$  K. The back gate voltage  $V_b = -30$  V is adjusted in order to recover a high resonant current level at  $T = 4.2$  K. b)  $I_{ds}(V_g, V_b)$  at  $T = 4.2$  K and  $V_d = 0.15$  mV around the split resonance. The current appears at a series of coupled triple points that characterise double dots in series: One dot with a charging energy  $\simeq 60$  meV is accumulated below the gate and modulates the current through the artificial atom (AA) under the spacers with a charging energy of  $\simeq 140$  meV. At  $T = 300$  K the accumulation dot does not block the current and a single resonance due to the AA is observed (see text). c)  $G(V_g, V_d)$  at  $T = 4.2$  K along the dashed line of panel b. A charging energy of 60 meV can be deduced for the accumulation dot. The sawtooth pattern is due to the addition of one hole in the AA [46, 49]. d) Simulation of the confinement potential and Local Density of States (LDoS) in a p-type sample with a  $\sim 4$  nm long dot under the source spacer (the AA), and a  $\sim 30$  nm long dot under the gate and drain spacer. The red line is the potential landscape in the channel, while the horizontal, black dashed lines are the Fermi levels in the source ( $\mu_s$ ) and drain ( $\mu_d$ ). The resonances in the channel give the energy and spatial extension of the quasiparticle states. There is one well defined quasiparticle state in the AA.

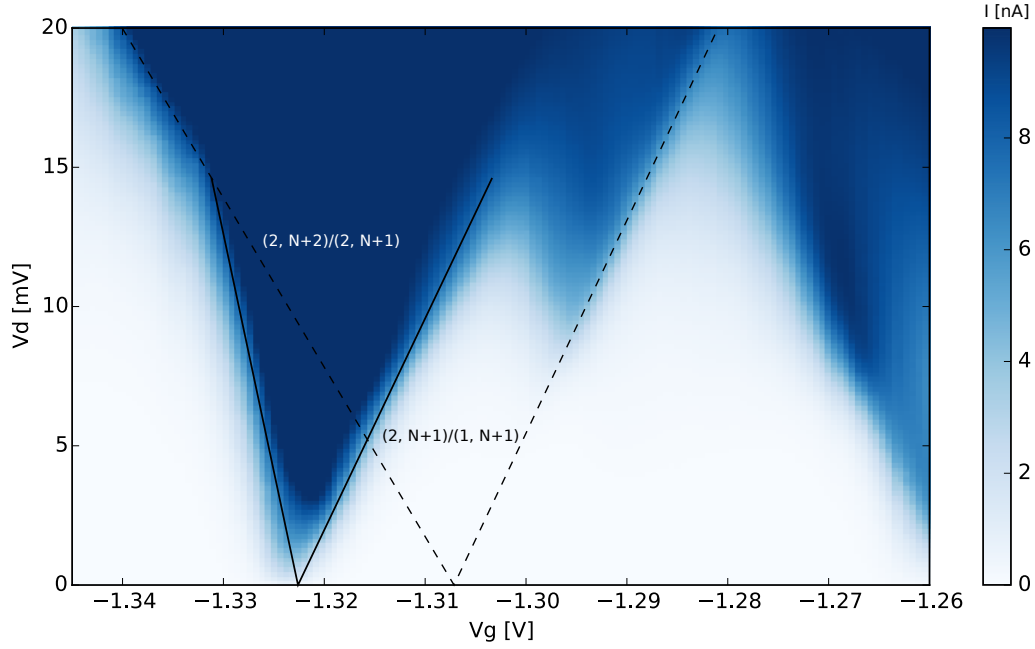


Figure 1.5  $I_{ds}(V_g, V_d)$  at  $T = 4.2$  K for the  $p$ -type sample. The edges of the two cotunneling diamonds (see text) are marked with lines as guides for the eyes.

dot would typically contain around 4 – 5 holes (injected from the drain) when the ground state energy level in the AA comes in resonance with the source.

figure 1.5 shows the  $(V_g, V_d)$  stability diagram of figure 1.4c based on  $I_{ds}$  instead of  $G$ . The current flows only by cotunneling through the artificial atom at the  $(2, N + 2) \rightarrow (2, N + 1)$  and  $(1, N + 1) \rightarrow (1, N)$  transitions. The lever arm parameter  $\alpha_g \simeq 0.47$  of the quantum dot can be estimated from the shape of the main diamond. Another diamond is barely visible on figure 1.5. It is due to the cotunneling through the quantum dot at the  $(2, N + 1) \rightarrow (1, N + 1)$  transition. The lever arm parameter  $\alpha_{g,AA} \simeq 0.34$  of the AA has been estimated from this other diamond.

The addition energy for the  $1h/2h$  transition is around 140 meV. It has been evaluated as the width of the 1 hole region ( $\Delta V_g \simeq 400$  mV, not shown) multiplied by the lever arm parameter  $\alpha_{g,AA}$ .

### 1.3 Role of surface roughness

The local density of states (LDoS) in the conduction band of a smooth  $n$ -type device ( $\Delta = 0$ ) is plotted in figure 1.6a, at the gate voltage just before the first electron tunnels into the

nanowire. There is large, about 175 meV conduction band offset between the S/D and the entrance of the nanowire channel visible on the LDoS. This offset results from quantum confinement and exchange-correlation effects. As a consequence, the chemical potentials of the source and drain are around 50 meV below the conduction band edge of the nanowire, and a Schottky-like barrier appears between the highly-doped contacts and the insulating channel. The potential in the channel takes a near harmonic form whose depth is controlled by the gate; the first few quasiparticle states in this potential are clearly resolved on figure 1.6a as resonances in the LDoS of the channel.

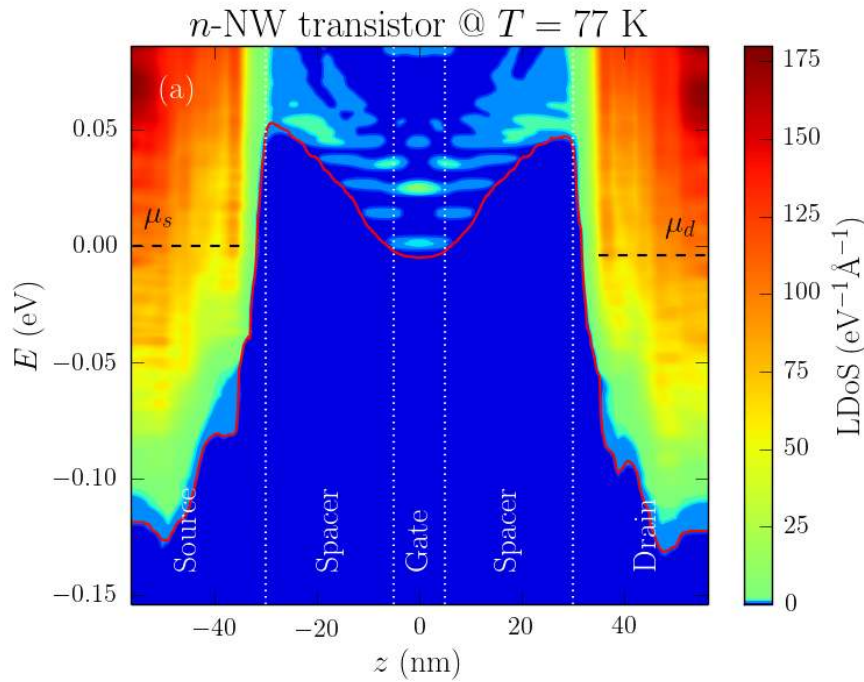


Figure 1.6 LDoS in a smooth  $n$ -type sample. The red line is the potential landscape in the channel, while the horizontal, black dashed lines are the Fermi levels in the source ( $\mu_s$ ) and drain ( $\mu_d$ ). The resonances in the channel give the energy and spatial extension of the quasiparticle states of the nanowire. They are broadened by the coupling with the S/D and phonons. The calculations were performed at  $T = 77$  K. Note that the color scale is non linear at small LDoS, in order to emphasize the (small) LDoS in the channel with respect to the (very large) LDoS in the contacts

This is different from the simulation with larger surface roughness presented in figure 1.2d. In this case the SR disorder leads to formation of the dots in the potential and raises barriers between these dots (the top of the barrier is at  $E = 97$  meV on figure 1.6b). Although the potential remains deeper under the gate, the distribution of localized states is completely different from figure 1.6. The charging energy  $U_{12}$  tends to increase with disorder. It is

$U_{12} \simeq 65$  meV in the smooth device of figure 1.6a and reaches  $U_{12} \simeq 90$  meV in the rough device of figure 1.2d..

We can conclude from figure 1.6 that room temperature Coulomb blockade with addition energies in the 200 meV range requires much stronger localization along the nanowire. Etching and oxidation can indeed carve narrow constrictions along some nanowires (see figure 1.4). Addition energies near 200 meV can be achieved in  $\sim 4$  nm long dots (with 4 nm diameter) separated from the rest of the channel by  $\lesssim 2$  nm diameter constrictions.

## 1.4 Conclusions

In summary, we have fabricated 3.4 nm diameter nanowire  $\Omega$ -gate MOSFETs with deliberately long offset spacers (25 nm) and short gate length (10 nm) using DUV lithography and standard 300 mm CMOS process. Such a design isolates the channel from the source and the drain and enhances Coulomb interactions within the channel. As a result, these devices show robust addition spectra characteristic of artificial atoms. The shape and location of these artificial atoms depend on line edge roughness along the nanowire but the most prominent source of disorder, i.e. the presence of few cavities in series can be managed thanks to the control by both front and back gate voltages. The addition energy can reach up to 230 meV depending on the surface roughness. The orbital excited state is several 10 meV above the ground state and the measured valley orbit splitting is around 5 meV in  $n$ -type devices, a large value for a quantum dot [50]. These devices bridge conventional MOSFETS with SETs, and show that Coulomb interactions within the channel are bound to play an increasingly important role in the physics and design of the next generations of silicon devices. Finally, the on-chip integration of these artificial atoms with CMOS peripheral modules controlling their operation is very easy, since large size transistors are made with the very same CMOS technology [44].

# Chapter 2

## Spin manipulation

In this chapter we investigate spin manipulation through spin resonance. We show a sample geometry tailored for this purpose and how mass-characterize it at room-temperature. We simulate the microwave behaviour of the on-chip antenna and how it can be used to drive spin resonance. Low temperature measurement are used to investigate spin blockade as a way for spin initialization and readout. We show signature of spin resonance and the effect of the valleys in the silicon conduction band. A theoretical model with numerical simulation is presented to explain the origin of the resonance signal. Selected measurement of a possible coherent spin manipulation (Rabi oscillation) are also presented.

### 2.1 Device

We want to study a system made by two coupled quantum dots in series. They should exhibit spin blockade for spin readout and show detectable transport down to the few-electron regime. To perform spin manipulation, we want a high frequency oscillating magnetic field applied to the spin confined in to the dots.

The dots are created on a 30nm-wide, 12nm-thick silicon nanowire, with two 35nm-long metallic gates over that. Spacing between the gates is about 30nm and this area is filled with 30nm wide spacers. These gates behaves as accumulation gates and create a dot underneath them. The NW section in-between is not gated and acts as tunnel barrier linking the two dots; the same is valid for the link between the dots and the leads (see section B and [51, 17, 52] for more details). In the latter case, the tunnel barrier has been shortened on purpose with a long annealing that diffused dopants from the leads; in this way the system is sensible to first-electron tunnel events.

In order to generate the oscillating magnetic field to drive the spin rotation we use a on-chip coplanar stripline antenna (see section 2.1.1). To accommodate the antenna close enough to

sample, the accumulation gates should be slightly redesigned. Both gates comes from one side of the nanowire and are cut on its edge. So instead of a “full” tri-gate cross section that embrace the nanowire on three sides (see figure A.2), the gates cover only one side and the top (see cross section in figure 2.2a). This new gate geometry is only partially self-aligned; this shortcoming is compensated by the large spacers that covers all the active area between the two gates. However, the electrostatic control is lowered and very sensible to the small variation of gate lithography (see section 2.1.2). On the other side, the RF antenna has been placed. Since it can be DC biased, it acts also as global side gate. Given the smaller electrostatic coupling compared to the accumulation gates, dots will likely be accumulated in the opposite corner. In figure 2.1 a 3D rendering and SEM image of the sample (without backend connections)

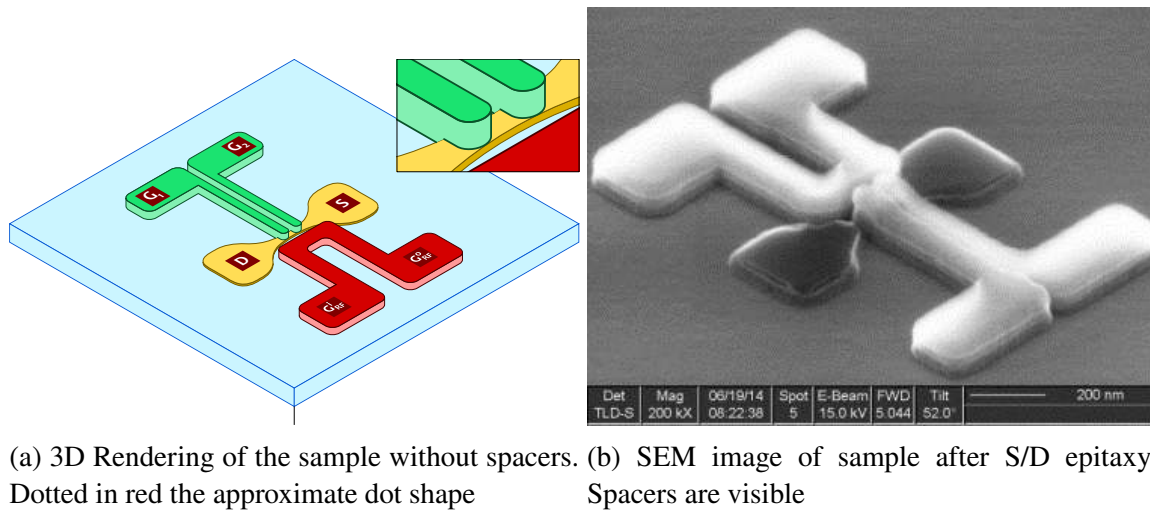


Figure 2.1 The sample

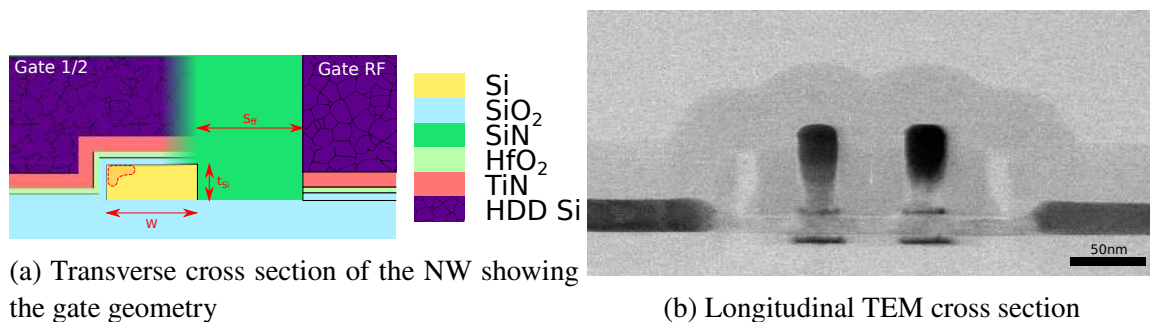


Figure 2.2 Sample cross sections

### 2.1.1 RF antenna

The role of the antenna is to deliver a gigahertz oscillating magnetic field to the confined spin. We aim to target a bandwidth roughly from 8 to 20GHz. In traditional ESR, this role is fulfilled by a macroscopic microwave cavity. This cavity is designed in a way to have stationary modes and the samples is placed in a position where the magnetic field oscillation are maximum (antinode) and the electrical field is minimum (node). It's crucial to minimize the radiated electrical field, because it heats the sample and leads to parasitic effects (such as photon assisted tunnelling) that can hide or suppress ESR signal.

Instead of a cavity we employed an on-chip coplanar stripline (CPS) [13]. In our case is basically a side gate connected on both sides to pass a current (see the red object in figure 2.1a). The resulting wire is parallel to the silicon nanowire and the generated magnetic field ( $B_1$ ) should be perpendicular to the substrate surface. If the static magnetic field ( $B_0$ ) is applied “in-plane” (parallel to the surface), the two fields are always perpendicular:  $B_0 \perp B_1$ . The antenna is made from the same layer of accumulation gates and the lowermost layer is made by TiN, which is a superconductor (see 2.1.1).

To maximize magnetic field and minimize electric field, we want drive the stripline with an odd-transmission mode, where the voltage polarity on the sides of the stripline is opposed. The opposite is an even-mode transmission, where the ends oscillates together. The transmission line connecting the stripline is crucial to deliver such mode and not dissipate power to the environment. The device coupling a waveguide (like a coaxial cable) with a stripline is called *balun*; it couples an unbalanced line (waveguide) to a balanced line (stripline). A fully integrated balun has been studied in details in [53]. Our design is constrained by the backend design, which is done only for DC connections and cannot be tuned. To resolve this issue, we simulated the RF behaviour of the stripline and its connections to properly evaluate their performances.

In figure 2.3a we can see the mask level for the backend. In orange are drawn the “IN” and “OUT” bonding pads for the stripline. The stripline is connected to the backend through tungsten vias. In figure 2.3b we can see a TEM cross section showing the two copper metal levels (identical on the mask), the copper vias connecting them and the tungsten via. Below the backend lines there is a metallic plane, which is a leftover of the gate level after the EBL lithography (green in the image). It effectively acts as a ground plane (GP) for the transmission lines, thus we talk about microstrip transmission lines, even if it's not assured that they are  $50\Omega$  matched. To properly ground this ground plane we bonded all the pads near the sample. These pads were made for devices with other purpose and not implemented in our fabrication process; these pads reach the GP with several tungsten vias. The pre-

metal dielectric (the dielectric that separate the device itself from the backend lines) is made by approximately 40nm of SiN and 260nm of SiO<sub>2</sub>, so the capacitance created by the pads with the GP is not negligible: for 70x70μm pads it's approximately equal to 0.64 pF. Given this big capacitance, we didn't bond the "OUT" bond pad, since the ground return at high frequency is fully provided by the ground plane. Since the GP is bonded with several bond wires, the total impedance to the ground is low, contrarily to one single bond wire (see the lumped element model of the circuitry in figure 2.3c). As positive side effect, the "OUT" pad behave as on-chip DC-block; the antenna is open on one side for the DC, so it can be easily used as side gate.

Another thing that has to be taken into account is the bonding wire length. As rule of thumb, one millimetre of bonding wire add 1 nH of inductance; due to constrains of the sample size, pad arrangement and the chip carrier, the length of our bonding wire is about 6mm, which leads to a non-negligible inductance of 6nH.

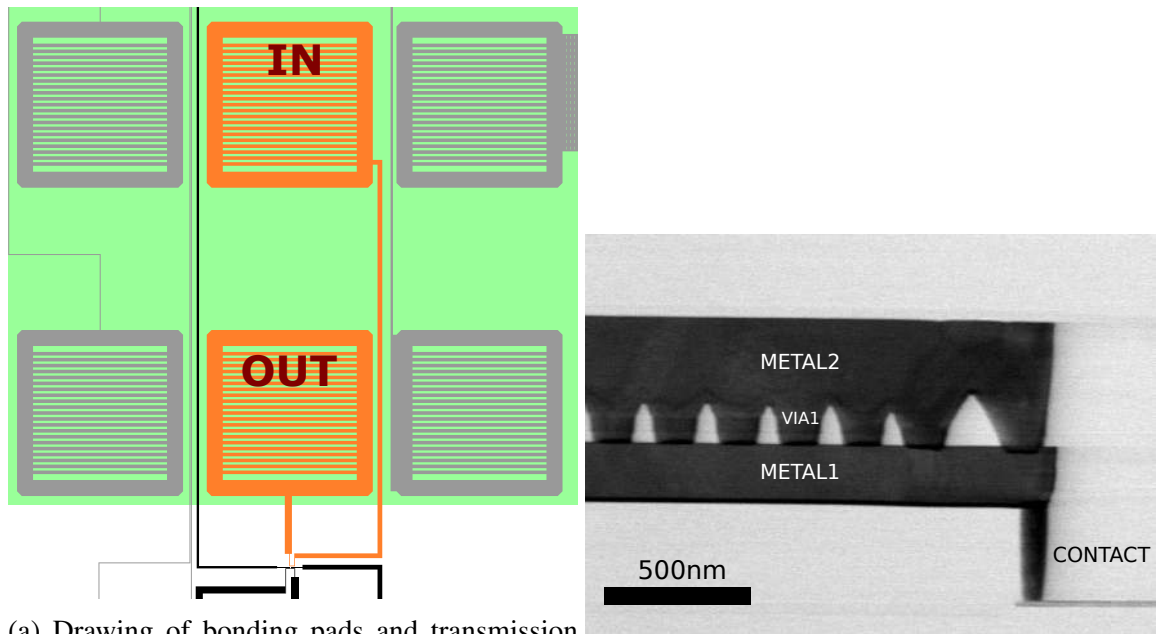
### Superconductivity

As stated before, the titanium-nitride in the antenna is well-known superconductor [54]. This greatly helps to reduce as much as possible the self-heating due the microwave, since it reduce the joule heating to the flow of current. TiN is a disordered superconductor with critical temperatures up to 4.5K [55]. Its properties are strongly dependent on the film thickness, which in our case is only 5nm. To characterize this film, we performed transport measurements on a straight wire with the same material stack and similar width (in centre, extension are larger to accommodate contact pads). The wire has been contacted twice on both side to perform 4-wire resistance measurements.

In figure 2.4a we can see the resistance as function of temperature and we clearly remark that we have a superconducting transition around 1.3K. The Resistance before the transition (about 1050Ω, which gives a sheet resistance of  $R_S = 18.1 \Omega/\square$ ) is lower than the expected one for a so thin TiN film [54]; this is consistent with a metal stack above the thin film. The critical current is up to 0.5μA at low temperature (figure 2.4b). Up to 0.9T the film is still superconducting, with as critical current of about 0.3μA (figures 2.4c 2.4d). The multiple peaks that are visible at low magnetic field are due to wider cross sections of the wire that undergoes transition at higher current and can be ignored.

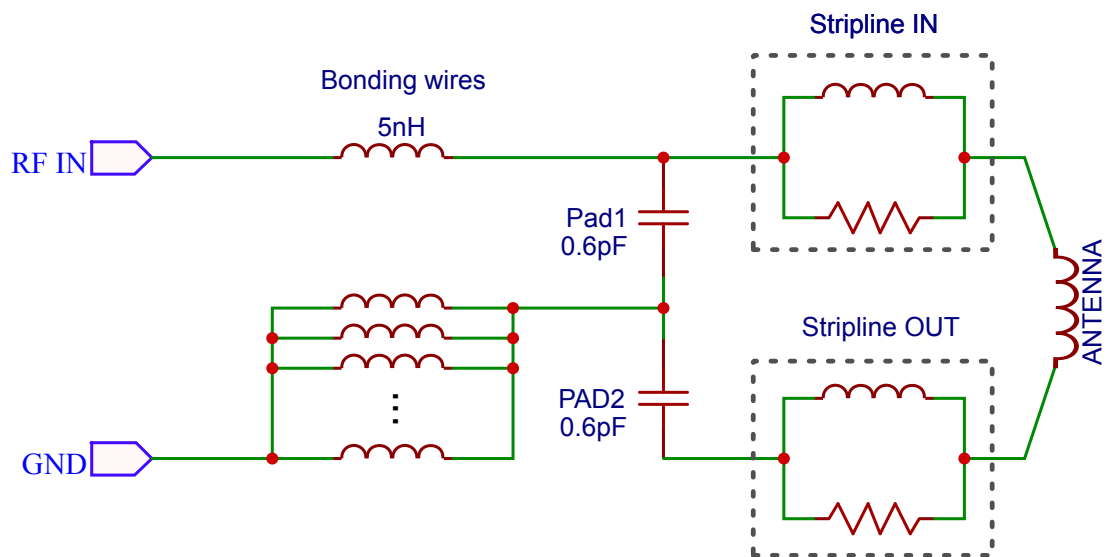
From these measurements we can estimate the kinetic inductance ( $L_S$ ), which is a critical parameter for our simulations. The normal state resistivity cannot be evaluated directly from our measurements because of the others materials in the stack, so it has been estimated from similar samples in literature to be  $\rho_{XX} = 17.5\mu\Omega\text{m}$ . The superconducting energy gap at zero





(a) Drawing of bonding pads and transmission lines

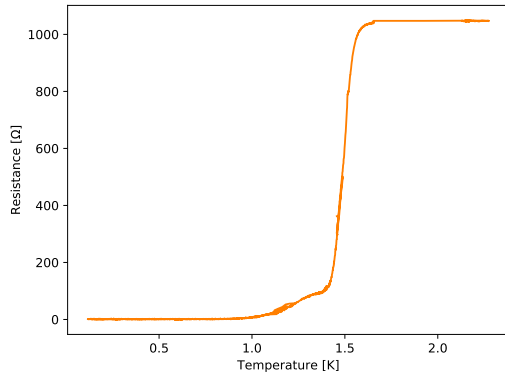
(b) TEM Cross section of the transmission lines



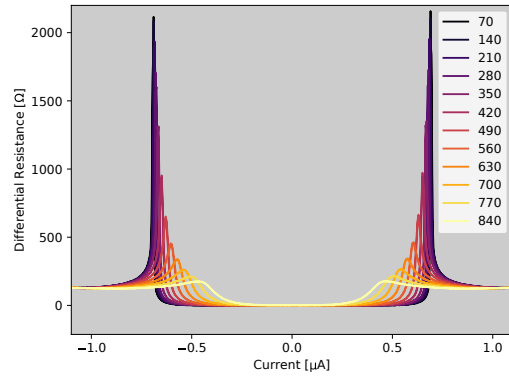
(c) Lumped elements diagram of the antenna circuitry

Figure 2.3 Details of the antenna's transmission lines

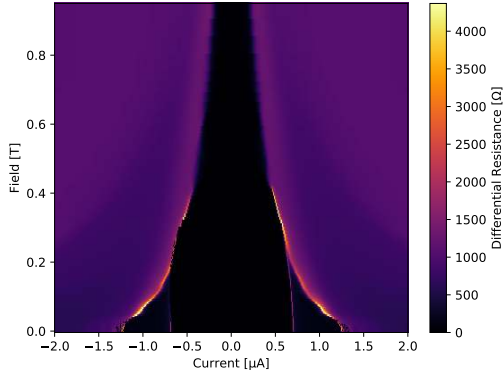
temperature, has been estimated from BCS theory  $\Delta(0) = 1.764k_B T_C \approx 0.2\text{meV}$  [56] and from that the magnetic penetration depth  $\lambda(0) = \sqrt{\frac{\hbar\rho_{xx}}{\pi\mu_0\Delta(0)}} = 3.8\mu\text{m}$  [57]. Finally the kinetic inductance is given by  $L_S = \frac{\mu_0\lambda^2(0)}{d} = 3.2\text{nH}/\square$ . This value is pretty high for our purposes, but it's normal given the thickness of the superconducting film. Thus at high frequency the current flow would probably be divided between the superconductor and the metallic polysilicon, which has a sheet resistance of  $R_P = 18.1\Omega/\square$



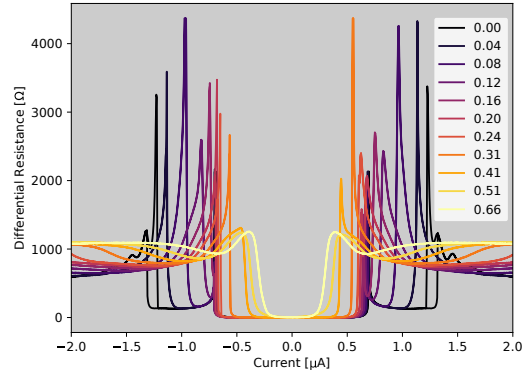
(a) Resistance at different temperatures



(b) Superconducting gap at different temp. (mK)



(c) Evolution of superconducting gap in field

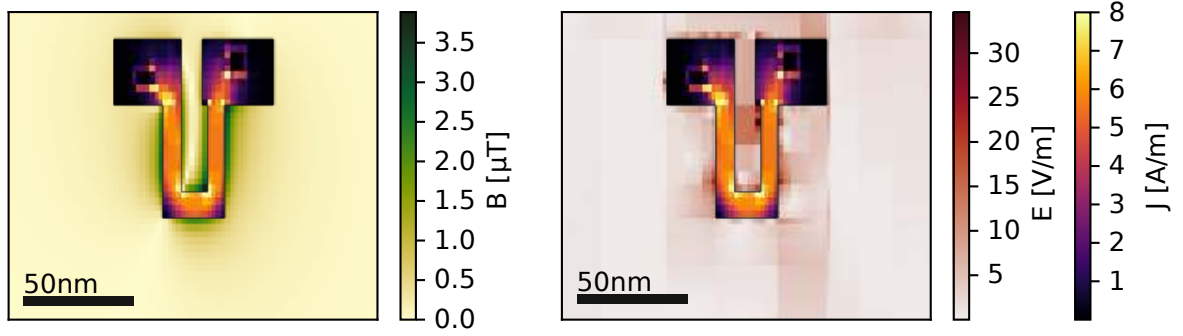


(d) Superconducting gap at different fields (T)

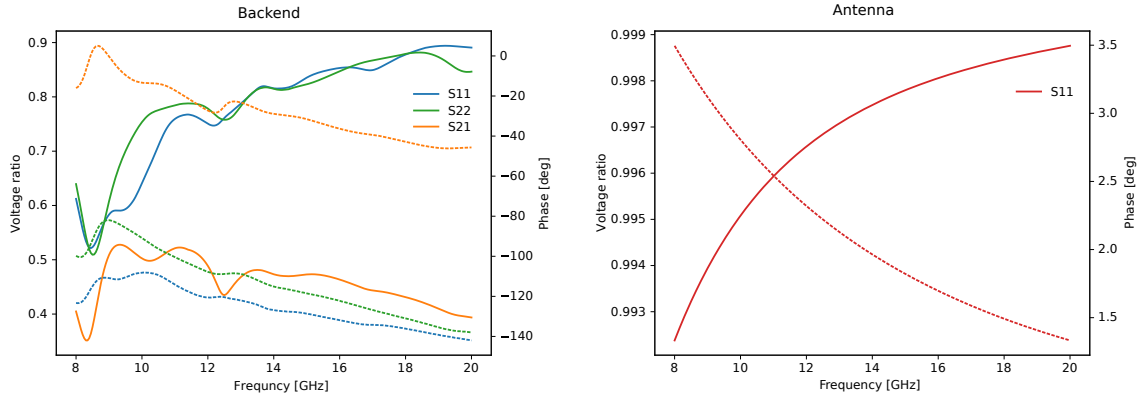
Figure 2.4 Measurements of superconductivity of RF line

## Simulations

To evaluate the performance of the antenna, we simulated its microwave behaviour. The goal of these simulations was to show that the antenna can generate an oscillating magnetic field on the dots site and evaluate its magnitude. Moreover we evaluated the electrical field and



(a) Simulation of magnetic and electric fields in the sample



(b) S-Params for the backend section and the antenna. Plain lines are for the magnitude, dashed lines are for the phase

the heat dissipated. We employed Sonnet [58] which is a planar electromagnetic simulation software. It can simulate the response of multi-port 2D structures at microwave frequencies. We used it to evaluate the S matrix of our system and the current density distribution. We simulated the antenna its backend connections and bonding pads as reported. The characteristic dimensions spans from the 80nm of the antenna width to the 70 $\mu$ m of the bonding pads; to evaluate behaviour on small features we need a fine meshing of the structure, which leads to enormous computations time and memory. Thus we divided the circuit in the backend part and the antenna part, evaluated separately with different meshing and accuracy. We calculated the S matrix of both structures; for the antenna we expect a short-circuit behaviour, so a  $S_{11}$  close to one (fully reflective). The backend on the contrary should be a good transmission line, with small reflected power. In figure 2.5b we can see that the antenna is an almost perfect short, while the backend reflections are not negligible; however the transmission coefficient  $S_{21}$  is still reasonable. We can use these values to evaluate the effective voltage that

reaches the antenna; the ratio of the input voltage to the output voltage is given by

$$V_{\text{ratio}} = \frac{S_{21}}{1 - S_{22}A_{11}}$$

where  $A_{11}$  is the reflection coefficient from the antenna. In figure 2.6 we can see this ratio evaluated for the backend alone and the same, but coupled to a  $50\Omega$  port with 6nH inductance in series to simulate the bonding wire. The voltage ratio is severely reduced in the second case. To complete the picture of the signal attenuation, we measured the attenuation of the RF lines in the fridges. It's approximately linear with the frequency (in GHz):

$$\text{Attenuation} = (-30.1 - 0.81 \cdot f)\text{dB}$$

Putting everything together, we find that for a signal on the top of the cryostat of +10dBm at 10GHz, we deliver an oscillating voltage of roughly 1mV.

From this value, we can simulate the current density in the antenna and the electric field radiated. To calculate the magnetic field, we used the Biot-Savart law. For a current in a 2D plane we have

$$\begin{aligned} \mathbf{B}(\mathbf{r}) &= \frac{\mu_0}{4\pi} \int \int_S \frac{\mathbf{J}(\mathbf{r}') \times (\mathbf{r} - \mathbf{r}')}{|\mathbf{r} - \mathbf{r}'|^3} d\mathbf{s}' = \\ &= \frac{\mu_0}{4\pi} \hat{\mathbf{k}} \int \int_S \frac{J_X(x', y')(y - y') - J_Y(x', y')(x - x')}{((x - x')^2 + (y - y')^2)^{3/2}} dx' dy' \end{aligned}$$

In figure 2.5a we can see the current density in the antenna and the distribution of the fields for a perfect odd mode. Around the antenna we get few micro-Tesla and Volts/meter. In figure 2.7 the fields are plotted for a cut perpendicular to antenna. We can see that the magnetic field on the nanowire is about 0.5μT, which can leads to a Rabi frequency (for g=2) CHECK

$$f_{\text{rabi}} = \frac{g\mu_b B_1}{h} = 14\text{kHz}$$

The simulated heat flux generated by the antenna is about 40 μW.

## Perspectives

Given the results of the simulations, our design can be improved in a next iteration. The antenna showed that a gigahertz magnetic field can be generated on-chip with a side gate. Titanium nitride is a good superconductor, with decent critical field and perfect compatibility with CMOS fabrication. However its limited thickness (5nm) harms both critical current and kinetic inductance, which limits the performance of the antenna in terms of thermal

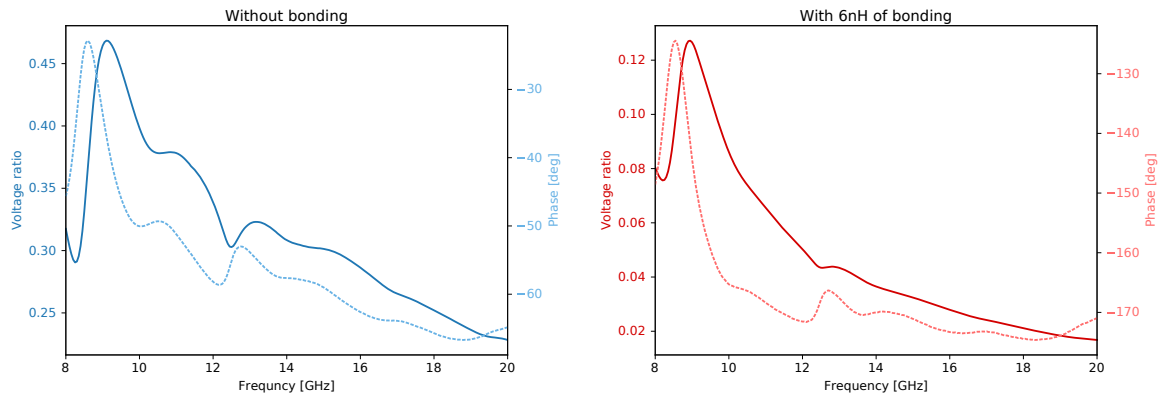


Figure 2.6 Simulations of the voltage attenuation for the copper backend without the bonding wire contribution (left) or with it (right). Plain lines are for the magnitude, dashed line are for the phase shift

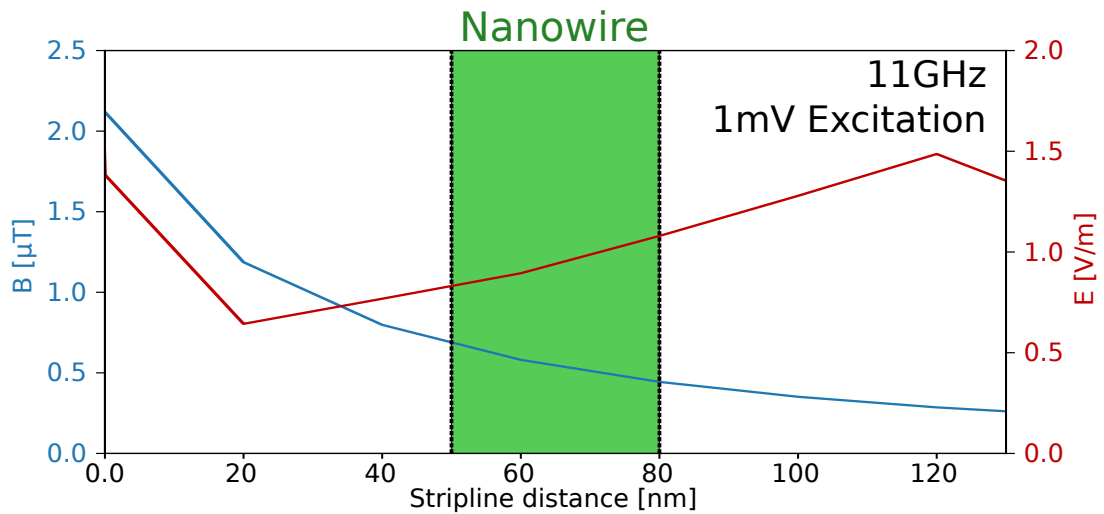


Figure 2.7 Simulations of generated fields (magnetic blue, electric red) as function of the distance from the stripline. In green is indicate the silicon nanowire

dissipation. One possible solution is to switch the gate technology to the so-called *gate-last*. In such case, the polysilicon layer is replaced by a metal, and that can be used to greatly increase the thickness of the superconductor. The layout of the antenna can be improved, by making a longer and wider wire instead of a sharp “U” shape. The backend connections should be tailored for microwave operations; 50-ohms port should be employed instead of simple DC-pads. A proper balun must be realized to propagate the correct differential modes and suppress the common ones. If permitted by the lithography, it should be done on the gate level instead of the metal level, in order to profit as much as possible of the presence of a superconductor. Another possibility is to use a full CPW design, with an antenna shorted at both sides as done in [59]. This design compared to CPS plus an integrated balun is much simpler to be implemented, since in the end it’s only a terminated CPW, which is relatively straightforward. However the generated magnetic field is only half of the CPS-based designs. Finally the sample holder should be designed with the sample in mind and minimize the length of the bonding wires, which is a major source of attenuation.

### 2.1.2 Selection

Samples with the required characteristic can be found in wafer 25 of batch “SiAM-2” (see table B.3). Twenty devices has been manufactured on this wafer and is essential to select the right one for the low temperature measurements. We performed a series of DC measurements at room temperature with the semi-automatic probe station and we employed a custom metric to rate the quality of the samples and infer some aspect of their low temperature behaviour. We took into account several criteria to compose the benchmark. First of all the mandatory “MOSFET” requirements:

- Undetectable gate leakage current for all the gates
- Threshold voltages must be reasonable; i.e. less than few volts
- Sizable field effect for all gates; i.e.  $I_{ON}/I_{OFF}$  ratio
- Accumulation gates must be able to turn off the device; i.e. the  $I_{OFF}$  current should be small
- The  $I_{ON}$  current should be sizeable

Then a series of specific requirements specific to this geometry:

- Accumulation gates should behave similarly

- Sub-threshold slope of accumulation gates is expected to be large (due to non-covering gates) but not excessive
- The side gate should have a moderate field effect and should be as effective as possible

DIBL (Drain-Induced Barrier Lowering) and parameters linked to the behaviour of drain bias has not been taken into account.

We performed a series of six measurement for each device, as explained on the table 2.10. One gate has been swept, while the other have been kept in “Open” or “Closed” position. The voltages are specific of the gate stack materials and thickness.

The Set A (measurements *OSC* and *SOC*) tests the both of the accumulation gates when the RF gate is “closed”, so when it’s pushing the electrons against the opposite corner. The two traces tends to be very similar, because the corners of the accumulation gates are less susceptible to large variations. In Set B (measurements *OSO* and *SOO*) on the contrary the gate Rf is “open”, so it’s attracting the electrons on its side. In this case the traces differs, because the electrons are mostly accumulated below the whole accumulation gate and their extremities. These edges positions are more sensitive to variations in lithography, so it gives an hint about the real shape of the gate and how much is covering the nanowire. Finally the third Set C (measurements *OOS* and *CCS*) check the effectiveness of the RF gate. Since is relatively fare away from the sample (compared to the other gates), it can’t switch ON or OFF the conduction, but only modulating it when the other gates are “open”. When they are “closed” is expected to have no effect.

As an example, in figures 2.8a and 2.8b the plots of these measurements with the relative SEM image (2.8f) of a tested sample (sample (8,0)). From the photos we can see that Gate1 is partially covering the nanowire, while Gate2 goes a little beyond the nanowire edge. This is mirrored into the electrical measurements; while Set A measurements are indistinguishable, in the Set B they differs. The lower threshold and the higher sub-threshold slope for Gate1 compared to Gate2 is the consequence of their geometrical differences. By regrouping measurements of Set A and B by the swept gate (so measurements *OSC/OSO* and *SOC/SOO*, figures 2.8c and 2.8c), we can see that the threshold voltages are shifted more by the RF gate when Gate1 is swept compared to Gate2. In fact Gate2 screen more the electric field of the RF gate than Gate1. Finally Set C (figure 2.8e) shows us more in detail how much the RF gate is effective in modulating the current. It’s pretty remarkable that tiny variations on the lithography greatly influence the transport behaviour even at room temperature.

On the contrary device (5,5) has similar gates, as can be seen in SEM image 2.9d. Its electrical characteristics (figures 2.9a and 2.9b) are thus much more regular and the gates work almost identically. From that we developed a series of parameters as benchmark:

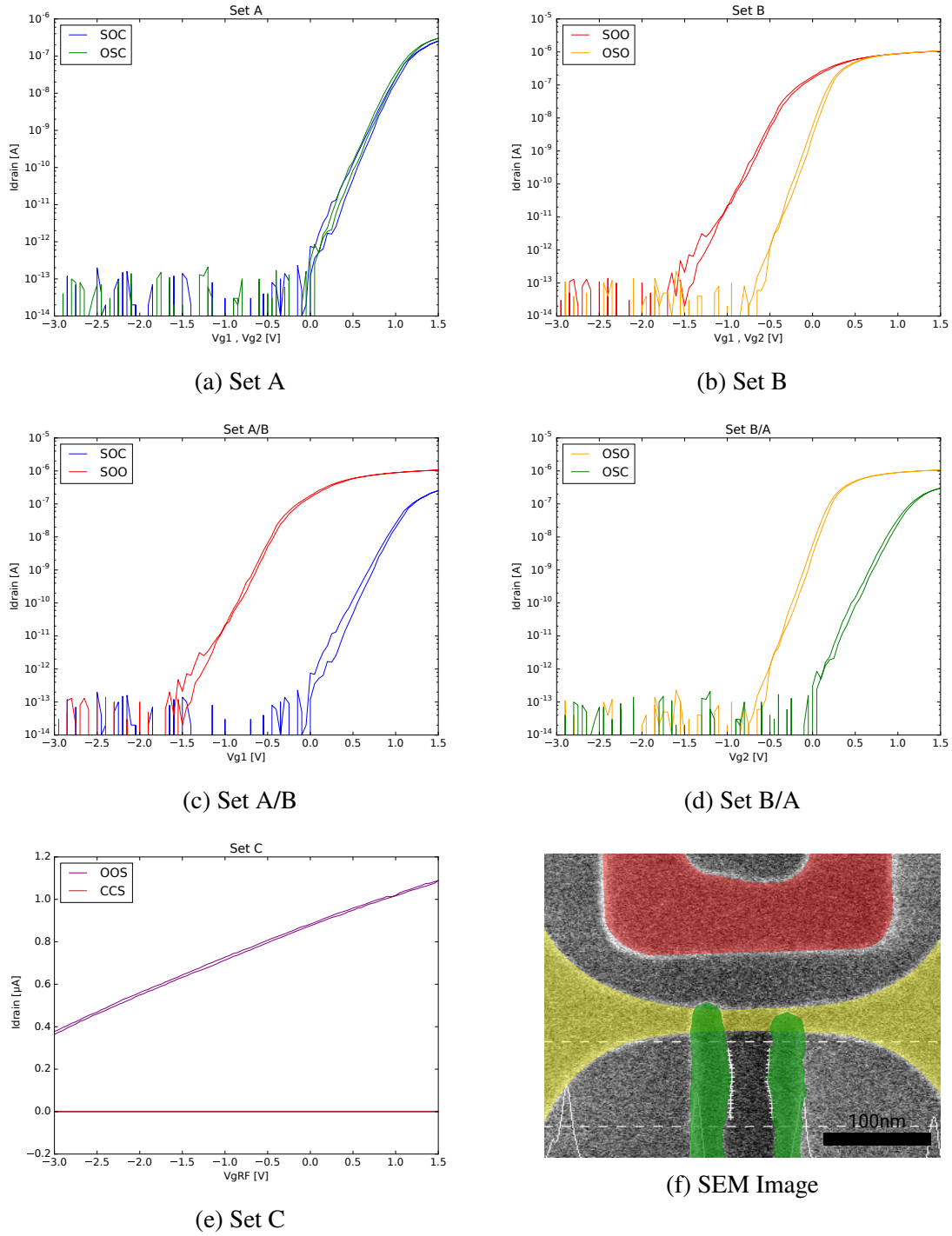
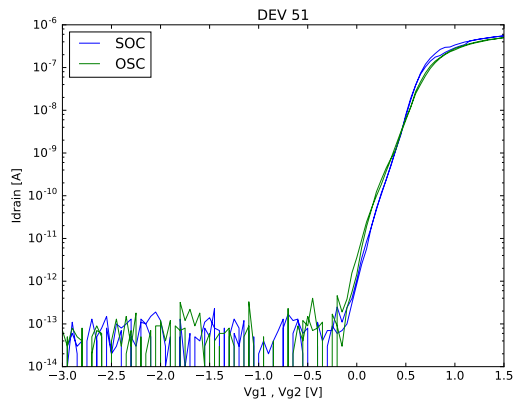
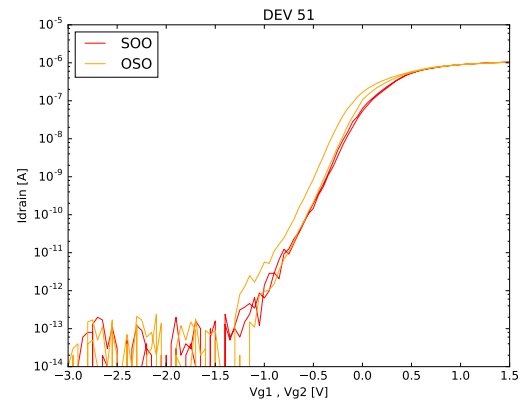


Figure 2.8 Room-temperature measurements of device (8,0)

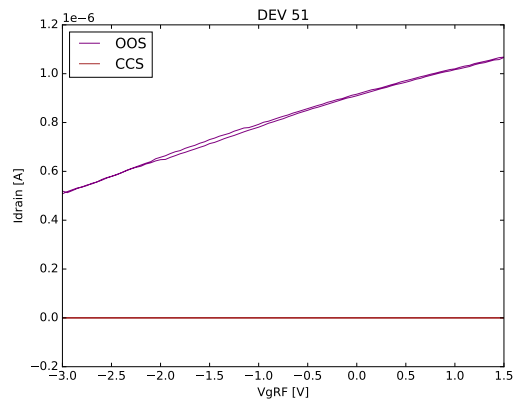




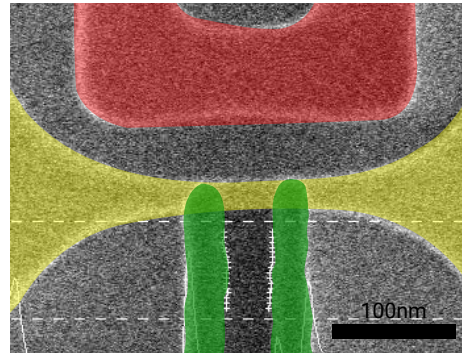
(a) Set A



(b) Set B



(c) Set C



(d) SEM Image

Figure 2.9 Room-temperature measurements of device (5,5)

- I<sub>ON</sub>** The current when a sweep reach the “open” value. Other gates could be either open or closed. It indicate if the device is conductive enough.
- I<sub>OFF</sub>** The current when a sweep reach the “close” value. Other gates could be either open or closed. It indicate if a gate has enough electrostatic control or not. If it's elevate, it could mean that there are too much dopants into the channel to prevent depletion.
- I<sub>ON</sub>/I<sub>OFF</sub>** The ratio of I<sub>ON</sub> over I<sub>OFF</sub>. Especially useful for Set C to evaluate the coupling of a gate
- V<sub>TH</sub>** The threshold voltage. Formally defined as the voltage where strong inversion occurs [60] we calculated it with the Linear Extrapolation (LE) method [61, 62]. It give an indication where first-electron tunnel events will take place at low temperature. In order to have similar shaped and similarly lead coupling of dots, we look for similar value within the same Set (A and/or B)
- SS** The sub-threshold slope is inversely proportional to capacitive coupling of gate with the electron gas. In this specific device their values are much higher than the minimum theoretical value at room temperature (60 mV/dec) due to shape of gates. Values higher than the mean indicates either a bad coupling or an higher concentration of dopants below the gate. Similarly to the threshold voltage we look for similar values in the same Set.
- I<sub>g</sub>** Gate leakage current. A current that flows from one gate to channel through the oxide. Must be the minimum possible.
- IntD** Integral difference. Is the difference of the logarithm of the area under two I(V<sub>g</sub>) curves in a Set:  $\text{IntD} = \int \log(I^{(1)}(V_G)/I_0) - \log(I^{(2)}(V_G)/I_0) dV_G$ . Is another way to define the “symmetry” of two gates.

From these parameters and the comparison with samples that have been imaged, we can infer an approximation of the shape of the sample without SEM images.

In table 2.10 there are all these parameters for all the devices. In green is highlighted the best one according to our requirements that has been measured.

## 2.2 Setup and device connection

The sample has been pre-characterized at room temperature in the automatic probe-station as explained in sections 2.1.2 and B.1. Then, the selected sample has been put in a dilution refrigerator, with a base temperature of 15mK. Gates and leads are connected up to

		GATE		
		1	2	RF
SET	A	O	S	C
		S	O	C
	B	O	S	O
		S	O	O
	C	O	O	S
		C	C	S

O	Open	1.5V
C	Closed	-3.0V
S	Sweep	-3 $\Rightarrow$ 1.5 V

Figure 2.10 Set of measurements performed at the probe station

Die	Distances			IntD[V]				I <sub>ON</sub> [μA]		I <sub>ON</sub> /I <sub>OFF</sub>	I <sub>OFF</sub> [fA]			
	G1/G2	G1/RF	G2/RF	SOC/OSC	SOO/OSO	SOC/SOO	OSO/OSC	OOC	OOO		COC	OCC	COO	OCO
(0,7)	37.48	44.96	40.01	0.84	0.65	6.15	4.66	0.295	1.206	4.08	0	580	-20	840
(-5,5)	32.35	40.30	*	0.05	0.02	0.05	0.02	<0.001	<0.001	-0.75	20	20	20	-10
(5,5)	33.93	43.69	40.99	0.19	0.14	5.64	5.59	0.551	1.044	1.90	-20	0	0	10
(0,4)	37.29	38.11	35.04	0.76	6.26	12.44	5.42	0.218	0.990	4.53	-60	50	-40	30
(-7,3)				0.34	6.70	13.05	6.01	0.399	1.254	3.14	0	0	100	0
(8,3)				0.07	0.35	7.75	7.33	0.215	1.047	4.87	-110	-30	-120	0
(-4,2)				1.18	1.04	4.27	4.13	0.597	1.165	1.95	10	30	0	-150
(0,2)				3.85	14.89	10.98	0.06	0.002	0.618	>100	0	100	-20	-70
(4,2)				1.69	4.21	5.11	2.59	<0.001	0.001	9.49	-10	-170	70	8110
(-8,0)	26.53	40.72	*	0.07	1.88	6.84	5.03	0.516	1.172	2.27	-80	-110	60	-60
(0,0)	40.82	42.29	37.03	0.68	4.22	9.00	5.46	0.321	1.128	3.52	-170	-20	150	-90
(8,0)	32.85	45.98	36.35	0.19	4.17	9.73	5.37	0.257	1.065	4.15	-10	-90	0	-120
(-4,-2)				0.46	0.21	5.65	4.98	0.457	1.013	2.21	-100	-30	-10	0
(4,-2)				0.06	1.66	5.75	4.03	0.382	0.860	2.25	-20	-140	-90	20
(-7,-3)				0.45	1.12	10.74	10.08	0.447	1.210	2.71	-70	-130	21840	9820
(0,-3)				0.04	2.51	6.82	4.35	0.464	1.099	2.37	-190	-70	20	-140
(8,-3)				0.38	2.53	5.43	3.27	0.527	1.182	2.24	0	-60	-40	-90
(-5,-5)	31.18	31.98	54.57	0.80	6.93	15.43	7.70	0.052	0.741	14.29	-190	-50	3760	-120
(0,-5)	31.48	40.85	36.01	2.13	4.41	15.22	12.94	<0.001	1.012	>100	170	-230	120	-10
(5,-5)	31.32	41.22	32.50	0.90	0.24	8.60	9.74	0.358	1.121	3.13	30	10	-150	-50

Die	V Threshold [V]				Sub-threshold slope [mV/dec.]				I <sub>leak</sub> [fA]			
	SOC	OSC	SOO	OSO	SOC	OSC	SOO	OSO	G2 OOC	G2 OOO	G4 OOC	G4 OOO
(0,7)	0.86	0.96	0.13	0.11	329	329	249	189	0	50	40	30
(-5,5)	1.04	-3.01	-0.70	-1.57	18	>999	5	297	>999	>999	>999	>999
(5,5)	0.59	0.61	0.10	-0.05	128	156	298	236	120	-550	-10	50
(0,4)	1.12	0.97	-0.38	0.05	274	289	417	179	410	-80	170	-40
(-7,3)	0.86	0.83	-0.48	0.05	210	190	317	269	100	-10	90	-120
(8,3)	1.10	1.21	0.04	0.09	330	336	251	254	60	30	10	50
(-4,2)	0.70	0.49	0.13	-0.01	154	126	154	166	-50	-10	120	120
(0,2)	1.23	0.84	-0.11	0.57	487	564	276	>999	100	100	0	150
(4,2)	1.09	-0.62	0.73	-0.45	320	286	>999	>999	-10	-120	-290	-70
(-8,0)	0.69	0.73	0.08	0.01	163	245	289	178	-20	-30	110	30
(0,0)	0.91	1.04	-0.22	0.14	272	244	334	154	-130	240	200	0
(8,0)	1.07	1.04	-0.09	0.16	243	233	385	151	770	-120	-40	-30
(-4,-2)	0.79	0.79	0.07	0.11	289	328	235	236	20	-120	30	-120
(4,-2)	0.72	0.64	-0.09	0.14	170	128	169	142	840	170	90	20
(-7,-3)	0.80	0.74	-0.43	-0.21	357	404	356	349	70	-150	150	40
(0,-3)	0.73	0.69	-0.04	0.14	182	161	234	170	90	10	70	150
(8,-3)	0.57	0.66	0.15	0.24	132	142	274	127	20	-380	30	-40
(-5,-5)	1.31	1.22	-0.60	0.04	273	305	310	195	120	-10	400	0
(0,-5)	1.28	1.31	-0.31	0.11	524	1142	312	254	220	100	-20	70
(5,-5)	0.80	1.01	-0.05	-0.12	137	200	343	332	-90	90	70	0

Figure 2.11 Results of room-temperature measurements for all candidates. When available, geometrical distances are reported. Non-working samples are grayed out

room-temperature by twisted pairs DC lines. The lines are filtered, both a room temperature (500Hz low pass filters) and at the base temperature (80MHz low pass filters, made by an home-made RC filters and Mini-Circuits VLFX-80). In addition to the DC signal, two high frequency lines with a bandwidth up to 20GHz are connected to the gate 2 and the RF stripline. These lines are used apply rapid pulses and/or microwave signals on the gates (see section 2.5.2 2.7). To reduce the thermal load, the line have thermalization points in terms of thermally anchored attenuators at the 1K, still and mixing plates.

In order to both apply a high frequency signal and DC bias on gate, these different signal get mixed at the base temperature by a bias-tee. The DC-Block is low rise-time commercial one (Tektronik PSPL5501A), while the RF filter is home-made on the chip carrier by a 10k $\Omega$  SMD resistance plus a wire that acts as inductor (see figure 2.12).

The chip carrier is PCB, with miniaturized connectors for 2 RF port and 24 DC lines. The substrate is ceramic-based, with copper metallic lines gold-plated, in order to have the best performances at high frequency.

The cryostat is equipped with a 2D vector magnet, which has been used to apply a static magnetic field in the plane of the sample. The angles in the text are expressed relative to the nanowire (ie. zero degrees means field parallel to the wire). The magnet is composed by two superconducting coils, which can reach a maximum of 9T/3T depending on the direction.

DC signal are generated by low-noise opto-isolated DACs. Readout is performed by a transimpedance amplifier with a gain of 10<sup>9</sup>V/A; a commercial multimeter is used to digitize the amplified signal.

Microwave signal are generated by an analogue microwave generator (Anritsu MG3693C), while fast pulses are generated by an Arbitrary Waveform Generator (Tektronik AWG520). These signals can be applied to the gate Rf or gate 2 (see section 2.7.1) for more details).

## 2.3 Stability diagram and bias spectroscopy

The selected sample has been cooled down to 15mK and the source-drain transport has been measured as function of all gates and drain bias voltage. The first goal was to drive the system in a mode where two dots in series are accumulated below the gates. We expect tunnel barriers to be formed in the access region below the outer spacers, as described in [35] The filling of these dots should be as low as possible and must exhibit spin-blockade (more on that 2.4). The signature of a double dot system is represented by a couple of conduction triangles in the plane of the gates voltages [63]. After the cooldown, we can compare the conductance measurements with the ones realized at room temperature (see figure 2.13). One gate has been kept on a high voltage (1V) to open its section of the channel, and the other one has been

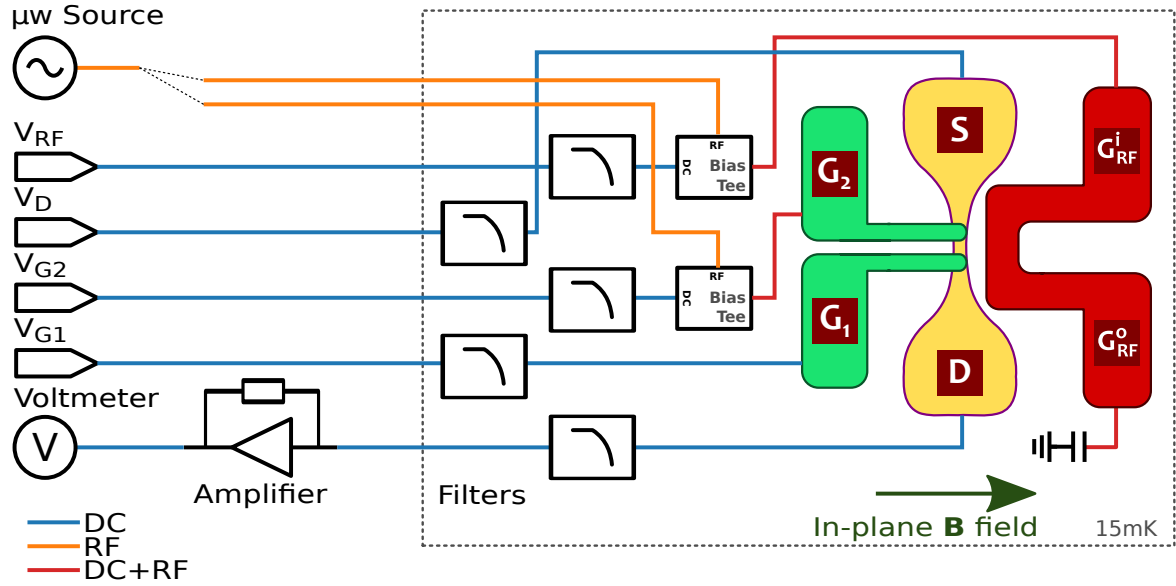


Figure 2.12 Schematics of the electrical connections

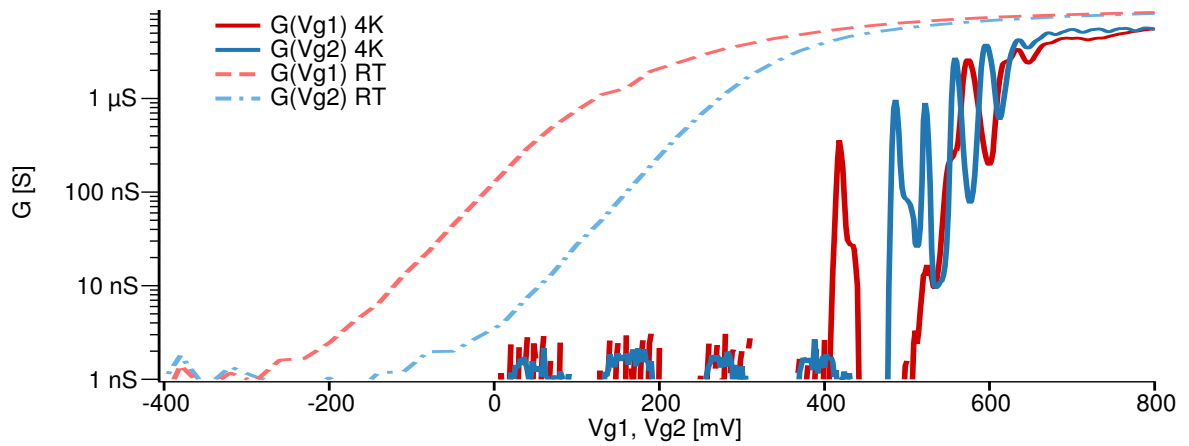


Figure 2.13 Room temperature vs 4K

swept. The drain bias is 5mV. We can see regular oscillations of the conductance, so under each gate we can accumulate a single dot and have coulomb blockade. As expected, the first visible peak appears not so after the room-temperature threshold. Oscillations for gate two are quite regular, with a period of 36mV and a first peak at 486mV. On the contrary, gate one shows an isolated peak at 420mV. The lower voltage of first peak is in accordance with the room temperature threshold voltages, which are shifted in the same way. We attribute this lone resonance to a transport enhanced by a single dopant in the access barriers.

In figure 2.14a the stability diagram, so the plot of current as function of both gates. It has been acquired at  $T=15\text{mK}$ , a side gate bias of -250mV and 10mV of bias. We can clearly see conduction spots triangle shaped. In the region for  $V_{g1} > 500\text{mV}$  these triangles are regularly spaced, with a large amount of co-tunnelling between them. As stated before, we attribute these to coulomb peaks of two dots in series, with a large ( $>10$ ) number of electron inside. The co-tunnelling is compatible with the gate geometry that doesn't cover fully the nanowire, thus reducing the barriers height at high dots filling. At  $V_{g1} \approx 430\text{mV}$  we can see a "band" of triangles; as stated before, we attribute the same double dot system, but their transport signature is visible due to a dopant assisting the tunnelling. These triangles are attributed the very firsts electrons tunnelling in the system. Measurement at large drain bias (not shown) suggest that is case, since no current is spotted below this region. A definitive answer is however impossible, given the lack of a charge detector/ In figure 2.14b we measured the first visible triangle (highlighted in blue in figure 2.14a) with a small bias of 2.5mV and the side gate voltage tuned to -280mV for optimal results. From now, all the measurements reported are done under these bias conditions, unless differently stated. The lever arm matrix, defined as the matrix that link the variation of the applied potential to the variation of dot's chemical potential

$$\begin{pmatrix} \Delta\epsilon_1 \\ \Delta\epsilon_2 \end{pmatrix} = M \cdot \begin{pmatrix} \Delta V_{g1} \\ \Delta V_{g2} \end{pmatrix}$$

can be calculated from the vectors on the side of a triangle, as in figure 2.14b

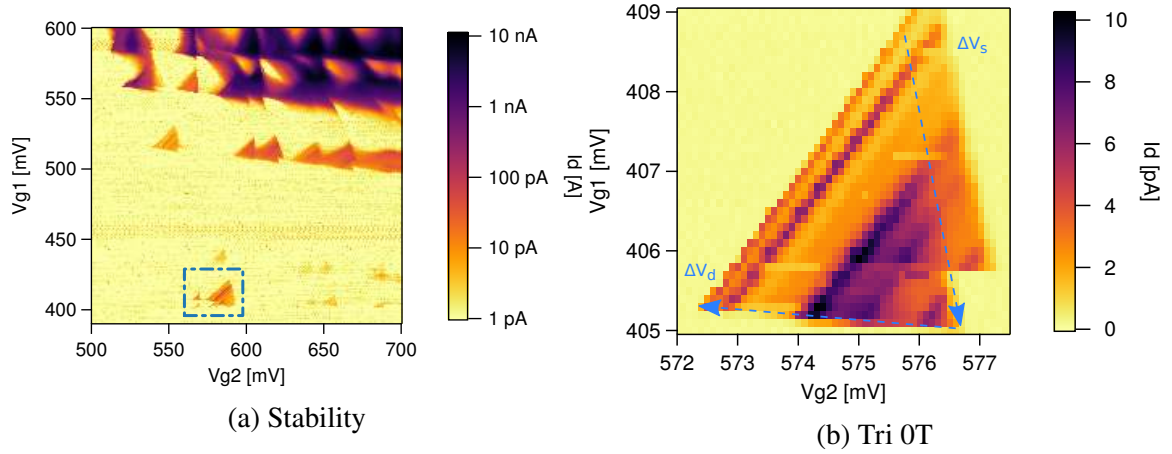
$$M^{-1} = \frac{1}{e|Vd|} \begin{pmatrix} \Delta V_{d^x} & \Delta V_{s^x} \\ \Delta V_{d^y} & \Delta V_{s^y} \end{pmatrix} \quad M = \begin{pmatrix} 0.67 & 0.03 \\ 0.18 & 0.52 \end{pmatrix}$$

From these values we can see that the dots are relatively well coupled with their gate, while a little of cross coupling is still present. This in accordance with electrostatic simulation, which predicts that the dots are mainly formed in the corners of the nanowire, on the opposite side of the RF gate.

We can notice that parallel to the base of the triangle, we have several conduction lines, associated to different energetic levels in the system [63]. The first one after the base is roughly 0.35meV above the ground state. We attribute this line to an excited state in the dot

2; this moderate value of the splitting is consistent with a valley orbit split ground orbital level in the dot. We can remark that these two lines are not perfectly parallel. In fact, if we calculate the splitting along the base we find that it varies from a minimum of 0.35 meV (lower left corner of triangle) up to 0.5 meV (upper right corner of the triangle). This slope also changed slightly between different measurements on a very long timescale (several weeks). This effect has been reported previously in literature, and it's commonly interpreted as a stark effect on the lowest-lying valleys [64]. The large electric field at the oxide interface, can change the energy splitting of the  $\pm k_z$  valleys [65]; by fixing the detuning value and moving along the base, we change the electric field, thus modifying the valley splitting.

The other lines in the triangle have been investigated with the help of an external magnetic field in section 2.4.



## 2.4 Magneto-transport and spin blockade

### 2.4.1 Spin blockade theory

Pauli spin blockade is a phenomenon that change affect the charge transport, due to the spin states of the electrons in a two (or more) dot system. Under specific conditions, the current flow is blocked by spin filling rules. In such case the spin in the system is well determined, at least until the spin relax with a time  $T_1$ . Thus Pauli spin blockade can be used for spin initialization and readout [13].

We consider a double dot system in the (0,1) charge configuration [14]; the charge states that contribute to the transport are the (1,1) and the (0,2). When two electrons are the dots (states

((1,1) and (0,2)) the spins can form a singlet or a triplet states:

$$\begin{aligned}
 S^{02} &= \frac{|\uparrow_2\downarrow_2\rangle - |\downarrow_2\uparrow_2\rangle}{\sqrt{2}} \\
 T_-^{02} &= |\downarrow_2\downarrow_2\rangle \\
 T_0^{02} &= \frac{|\uparrow_2\downarrow_2\rangle + |\downarrow_2\uparrow_2\rangle}{\sqrt{2}} \\
 T_+^{02} &= |\uparrow_2\uparrow_2\rangle
 \end{aligned} \tag{2.1}$$

$$\begin{aligned}
 S^{11} &= \frac{|\uparrow_1\downarrow_2\rangle - |\downarrow_1\uparrow_2\rangle}{\sqrt{2}} \\
 T_-^{11} &= |\downarrow_1\downarrow_2\rangle \\
 T_0^{11} &= \frac{|\uparrow_1\downarrow_2\rangle + |\downarrow_1\uparrow_2\rangle}{\sqrt{2}} \\
 T_+^{11} &= |\uparrow_1\uparrow_2\rangle
 \end{aligned} \tag{2.2}$$

where in original eigenstates the number indicate in which dot the electron is, and the arrow its spin orientation. The singlets have a zero total spin, while the triplets have a total spin of one. The triplets have three possible spin  $z$  components, which are indicated by  $-$ ,  $0$  and  $+$ . At zero magnetic field, they are all degenerate, and at finite magnetic field they split by the Zeeman energy.

In the (1,1) configuration, the electrons can occupy the lowest lying orbitals in both singlet and triplet states. Thus their energy difference will be small, and inversely proportional to the detuning  $\epsilon$ . When the levels are aligned at zero detuning, the exchange energy is equal to  $J = 4t_c^2/E_C$  in the Hubbard approximation [14];  $t_c$  is the tunnel coupling and  $E_C$  is dot charging energy. From now, we consider the energy difference between the  $S^{11}$  and  $T^{11}$  to be small compared to the others energies. On the contrary, for the (0,2) charge configuration, both of the electrons are in the same dot; due to the Pauli exclusion principle, to form a triplet state the electrons should occupy different orbital, thus increasing the energy difference of singlet and triplet. For silicon quantum dots singlet-triplet splitting  $\Delta E_{ST}$  is in the order of few hundred  $\mu\text{eV}$  up to  $\text{meV}$  [66–68]. The tunnel coupling hybridize the (1,1) and (0,2) states with same quantum numbers; however if the spin is conserved during tunnelling, tunnelling is allowed only between states with the same spin. The energy diagram is reported in figure 2.16.



For a finite drain bias, the transport sequence is  $(0,1) \rightarrow (1,1) \rightarrow (0,2) \rightarrow (0,1)$  for a positive bias (on the left lead); for a negative bias is  $(0,1) \rightarrow (0,2) \rightarrow (1,1) \rightarrow (0,1)$  (figure 2.17). If we consider the second case, for a given gate bias configuration, the electron coming has only the  $S^{02}$  state accessible, so an electron with the right spin can enter and form a singlet. Then it can tunnel to the second dot through the  $S^{11}$  and then to the other lead. So in this case there is no additional blocking other than coulomb blockade. Otherwise, for a positive bias, an electron can enter in both the  $S^{11}$  and  $T^{11}$  states. If it forms a singlet, it can tunnel out through the  $S^{02}$  state; but as soon as an incoming electron forms a  $T^{11}$ , it can not hybridize to  $S^{02}$  because of the spin conservation, neither to the  $T^{02}$  because it's energetically inaccessible for a detuning smaller than the  $\Delta E_{ST}$ . In this case we are in a *Pauli spin blockade* regime. The current is blocked and the double dot system is a well defined spin state. The spin has to relax to the singlet ground state to unblock the current. This happens on a timescale of  $T_1$  spin relaxation time, but since this time can be very long (up to seconds or even minutes [20]) this current is negligible. If the detuning is raised above  $\Delta E_{ST}$ , the blockade is raised because the electron can escape through the  $T^{02}$  excited state.

The first experimental signature of spin blockade is a rectification of the current; if we record bias triangles for both of the bias polarities, the base of the triangle for the positive bias would be missing. In the case of an ideal spin blockade (no relaxation effects), for  $\varepsilon < \Delta E_{ST}$  the current should be suppressed. However, in usual quantum dots, there are several mechanisms that partially lifts the spin blockade. In section 2.4.2 these mechanisms are explained in details. Usually (but not in all cases) spin blockade is recovered with a finite magnetic field.

This derivation is not limited to singlet and triplet states created by two electrons, but applies also (with some limitations) to states with more than two electron, when we can create states with different parities that can be spin blocked. If the incoming electron can create a singlet state with the highest-energy electron in the dot and the triplet is energetically high,

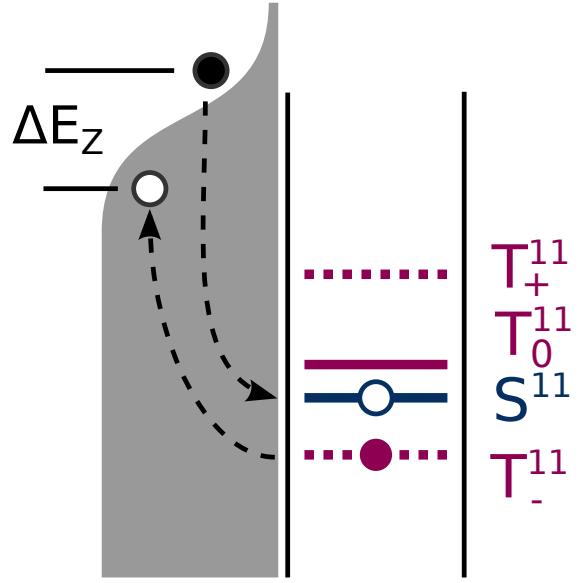


Figure 2.15 Schematics of spin-flip co-tunnelling

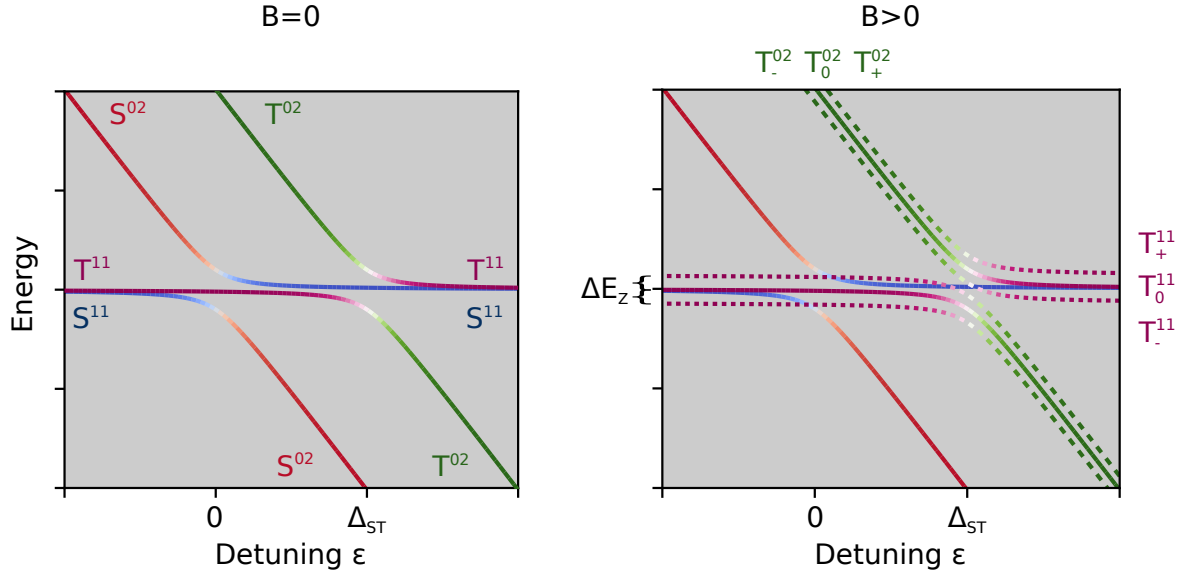


Figure 2.16 Evolution of two spin states in a tunnel coupled double quantum dot system as function of detuning. Colours represents the corresponding eigenstate. On the left the magnetic field is zero, while on right it lifts the degeneracy of triplet states by Zeeman effect

we may have spin blockade. This situation is like an atom, where only the external orbital forms bonds, and the others are inert. Thus we may have spin blockade for dots filling  $(N, M+1)$ , and not on  $(N, M)$  [69, 70]. In silicon we also have the valley degree of freedom, which can contribute to the blockade. In this case we call it *valley-spin blockade*.

## 2.4.2 Lifting of spin blockade

Pauli spin blockade can be suppressed by a series of phenomena. The interaction of the spins with the environment can affect the lifetime of the spin states, thus lifting partially or totally the spin blockade. Any mechanism that mix the singlet and triplet states or induce transition between them, can alter the spin blockade. In our case, there are three main phenomena that we have to consider:

**Hyperfine interaction** The electron spin are confined in quantum dots made by materials which may posses a nuclear magnetic moment. These moment act as random inhomogeneous effective magnetic field, the *Overhauser field*[71], which can induce mixing between the singlet and triplet states. In such case the Pauli blockade can be lifted, because the system can not stay anymore in a pure triplet  $(1,1)$  state, thus coupling to the  $(0,2)$  regardless of the spin state. This is true if the if the energy of this gradient of magnetic field (given by  $E_N = \mu_b g \delta B$ ) is lower than the Zeeman energy of the external magnetic field. Otherwise, if  $E_z > E_N$ , the mixing is suppressed and the

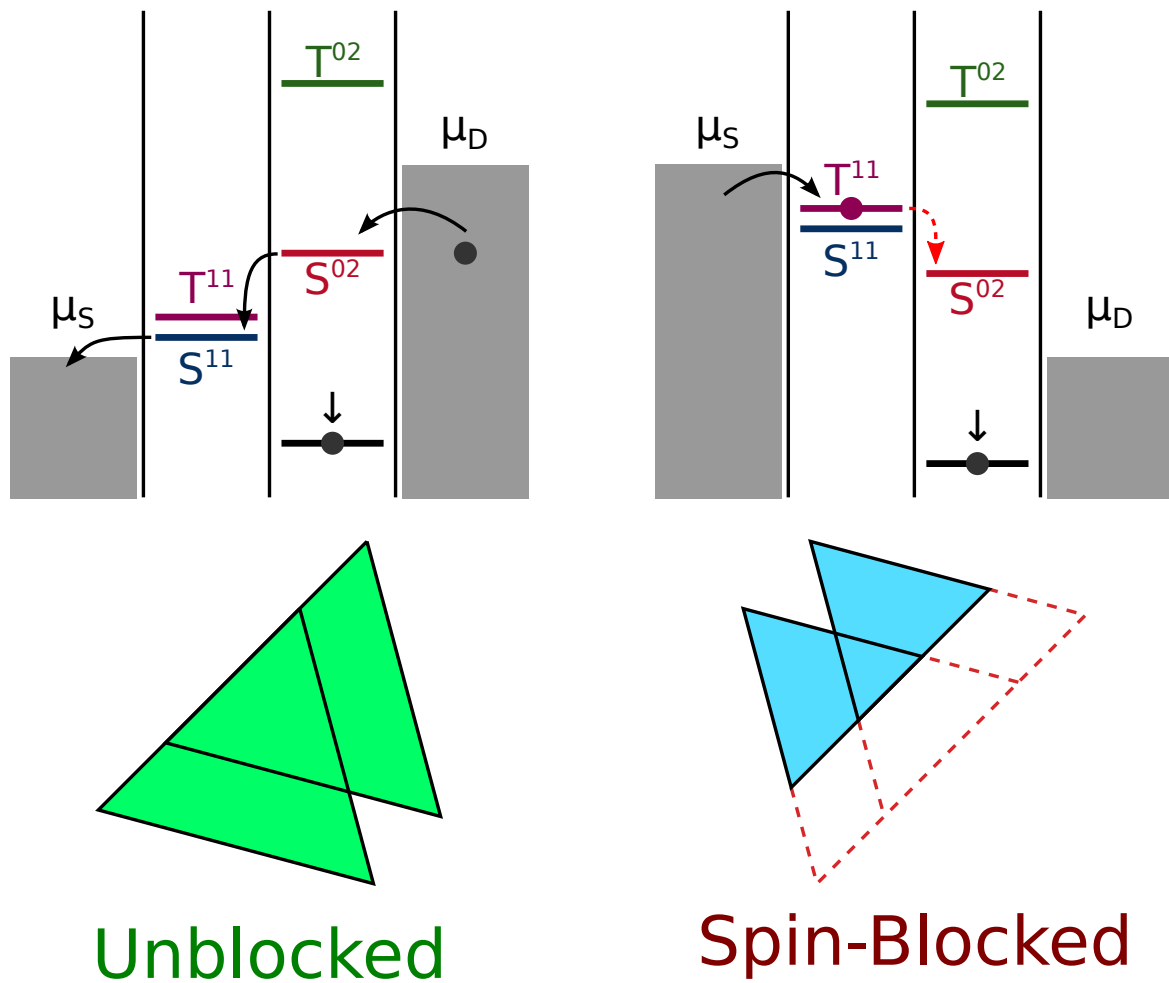


Figure 2.17 Scheme of energetic levels and bias triangles for a tunnel coupled double quantum dot system. On the left the system is not spin-blocked, while on the right is spin-blocked.

spin blockade is restored [72, 14]. The magnitude of this random magnetic field is approximately  $\delta B \approx \delta B_{fp}/\sqrt{N}$  where  $\delta B_{fp}$  is the maximum magnetic field when the nuclear spin are fully polarized and  $N$  is the number of nuclei. For GaAs quantum dot this is not negligible, since  $\delta B \approx 2 - 6 mT$  [66]. In silicon, the amount of nuclear spin is reduced, since only  $^{29}\text{Si}$  posses a nuclear spin; doping with  $^{75}\text{As}$  can increase the amount of nuclear spins, but it should be a relatively minor contribution. Theoretical estimations of the Overhauser field for natural silicon, give a value of  $0.37 \mu T$ , which in the context of spin blockade could be considered negligible [73] (not the same for coherence times).

**Spin-flip co-tunnelling** Spin-flip co-tunnelling is a co-tunnelling mechanism where the blocked spin is exchanged with another electron from the lead. Suppose that we are in a spin blocked triplet (1,1), co-tunnelling would happen if the blocked spin is exchanged by virtual tunnelling with the nearby lead for another one with the opposite spin orientation. The process is composed by two simultaneous virtual tunnelling event. In the first, the blocked spin tunnel to an empty state below the Fermi level, creating a virtual intermediate state. Then an electron, with opposite spin above the Fermi level, tunnel in the dot, creating a singlet (1,1) which is unblocked (see figure 2.15). This process is then thermal dependent, since it relies on the availability of electron above the Fermi sea and holes below. Also it's strongly suppressed by an external magnetic field. With a large enough magnetic field,  $T_-^{11}$  becomes the ground state, and the energy difference with the  $S^{11}$  increase linearly with the field. The co-tunnelling rates are exponentially suppressed with respect to the magnetic field. In the case of a weak interdot tunnelling ( $\sqrt{2}t < k_B T$ ) and weak co-tunnelling ( $\Gamma_{cot} \ll \Gamma_{SD}$ ), the leakage current [74, 66] is given by

$$I(B, \epsilon = 0) = 4/3 e \Gamma_{cot} \frac{g \mu_b B}{\sinh\left(\frac{g \mu_b B}{k_B T}\right)}$$

We can see that the current is strongly suppressed with a finite magnetic field, with a magnitude given by the co-tunnelling rate and the temperature.

**Spin-orbit interaction** Any charged particle that moves in an electric fields, feels an effective magnetic field proportional to  $\mathbf{E} \times \mathbf{p}$ , as a consequence of Lorentz transformation. In analogous way to an electron orbiting a nucleus, this effect is called *spin-orbit interaction*. Electrons moving in the lattice of a crystal, feels its specific periodic electric field. In solid systems, we usually consider two contributions: bulk inversion asymmetry (BIA, or Dresselhaus [75]) and structural inversion asymmetry (SIA, or Rashba

[76]). The first, as the name imply, arise in materials that lacks the inversion symmetry (like the zincblende structure of GaAs); is usually not considered in silicon. The second one arise when there is a strong discontinuity in the bulk crystal, such as interface, which is effectively an electric field. For a 2D structure, with the xy plane, these two spin-orbit Hamiltonians can be written as:

$$H_D = \beta [-p_x \sigma_x + p_y \sigma_y]$$

$$H_R = \alpha [-p_y \sigma_x + p_x \sigma_y]$$

where  $\alpha$  and  $\beta$  are respectively the Rashba and Dresselhaus spin-orbit coupling terms,  $P_i$  is the momentum operator and  $\sigma_i$  are the Pauli matrices.

In the context of spin blockade, the main effect of a spin-orbit interaction, is to introduce nonspin-conserving tunnelling terms that have the effect of coupling the polarized triplet states with the singlets. So, spin-orbit interaction can lifts the spin-blockade as well. However this effect depends strongly on the external magnetic field, or in other words on how much  $T_{-,+}^{11}$  are split apart. For small fields, the states are close enough in energy to re-arrange into new states. One of these states it's coupled to the  $S^{02}$ , so it contribute to the leakage current, while the others no. Therefore the current at zero field is  $I_0 = 4/3e\Gamma_{rel}$ , where  $\Gamma_{rel}$  is the spin relaxation rate [77]. When the field is increased, the coupling of two of three blocked states to the leaking state increases, and at high field it reaches its maximum of current  $I_{max} = 4/3e\Gamma_{rel}$ , where only one state is blocking and the others three are leaking. Thus we have a zero-field dip in the current, with a width which is proportional to the strength of the spin-orbit interaction. At very high field and low-temperatures, the ground state  $T_-^{11}$  is so far apart from the others, that the system is pushed in coulomb-blockade regime in this state, thus suppressing greatly the leakage current [70]. The final picture would be double peak structure, with a zero-field dip.

**Spin resonance** Spin resonance is a phenomenon used to actively drive transition from the blocked triplet states, to the unblocked singlet states. In fact we use it in the other way around: we use spin blockade as way to initialize and readout a spin to perform spin resonance. More on that topic is section 2.5.

**Photon assisted tunnelling** If we apply to the sample a microwave field (usually thought one gate), we can induce transition between levels, lifting spin and/or coulomb blockade. This effect is called *Photon Assisted tunnelling* (PAT). It is an inelastic tunnelling, since energy is provided by the incoming photon  $h\nu$  [63]. Spin-blockade can be lifted

by either assisted tunnelling to a lead or to a triplet in the (0,2) state [78]. In our case PAT is regarded as a parasitic phenomenon when performing Spin Resonance experiment.

These mechanisms are not-mutually exclusives, so they can take place together.

### 2.4.3 Magnetotransport measurements

To verify that we have spin blockade on our triple point, we measured the current as function of detuning and magnetic field for two opposite polarities ( $\pm 2.5$  mV), as reported in figure 2.18. We can see that for a negative bias of -2.5mV there are no major modifications in going from zero to 0.7T. The triangle appears mostly uniform, without a clear indication of excited states and it seems dominated by inelastic process. On the contrary for a positive bias, the current is strongly suppressed for  $B \gtrsim 200$ mT for  $\varepsilon < 1.9$ meV. Therefore under these condition the system is in spin-blockade and  $\Delta E_{ST} = 1.9$ meV. The leakage current can be attributed to spin-flip co-tunnelling, given the field where it gets suppressed, which is larger than the one expected for hyperfine interaction.

We can look more in detail at the spin-blockade and leakage current. In figure 2.19a is reported a measurement of leakage current for a finite detuning of  $\varepsilon = 0.72$ meV as function of magnetic field. The measurement has been carried at very low magnetic field rate of 5mT/min, downwards and then upwards (figure 2.19a). We can clearly see the spin flip-co-tunnelling leakage current decaying as function of magnetic field. Surprisingly the two traces are not perfectly equal, and they show an evident hysteresis. This hysteresis has no clear explanation; it can be due to non-idealities of the magnets or ferromagnetic materials nearby the sample. The sample itself can have some permanent magnetism due to its composition (see section 2.8.1). Another option is Dynamic Nuclear Polarization of arsenic and silicon-29 in the samples, but their concentration is very low. Other samples in this and other batches have not shown this behaviour.

On top of the leakage current, at around zero field (slightly shifted by the hysteresis) we can see a small dip, also zoomed in figure 2.19b. This small dip can be attributed to a large spin-orbit interaction. The presence of co-tunnelling leakage and hysteresis make difficult an evaluation of the strength of spin-orbit interaction.

Finally, we can remark a sharp peak at about 330mT. This peak is the result of spin-blockade lifting as well, as we can see in figure 2.19c, where it manifests as a vertical line in the detuning against field plot. The origin of this peak will be discussed in section 2.6.

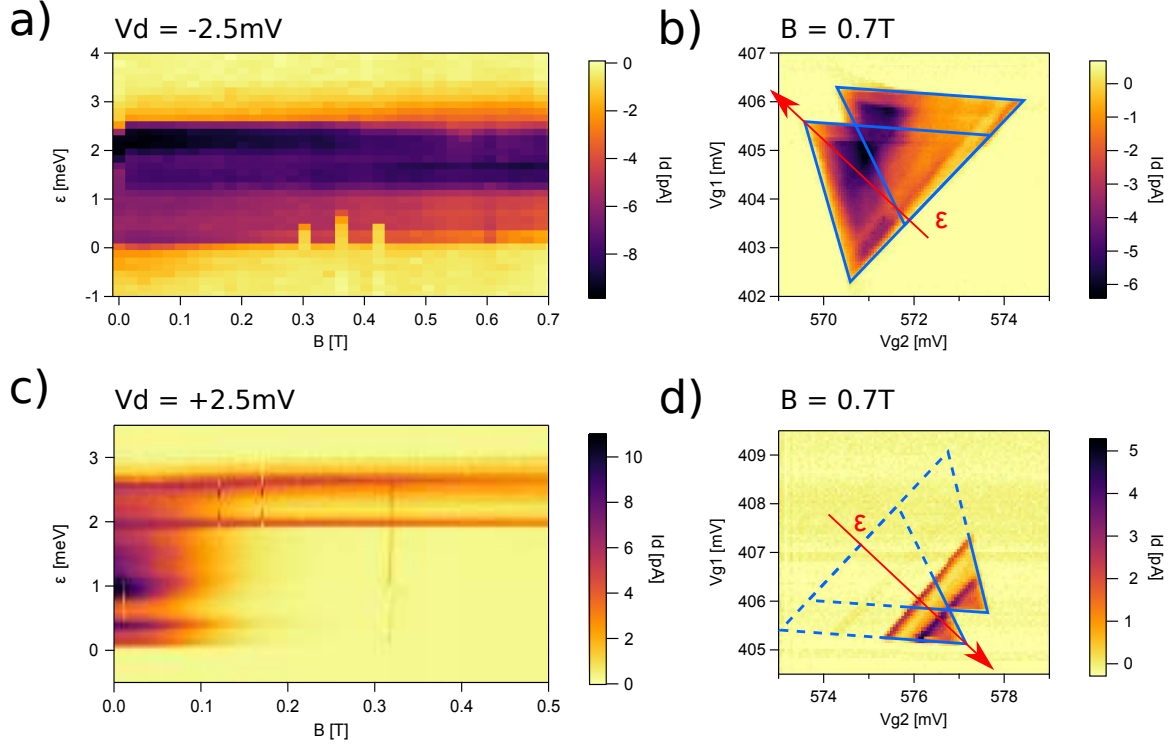


Figure 2.18 Search for spin blockade. **a** Colour-plot of the measured Source-drain current  $I_{sd}$  as function of external applied magnetic field for a drain bias of -2.5mV and  $T=15$ mK. **b** Double dot bias triangles: Source-drain current  $I_{sd}$  as a function of gate voltages  $V_{g1}$  and  $V_{g2}$  for a drain bias of -2.5mV, a magnetic field of 0.7T and  $T=15$ mK. Edges of triangles are highlighted with light-blue lines. Red arrow indicate the detuning axis used in figure a; zero detuning is at the base of the triangle. **c** Same as (a), but with drain bias of +2.5mV. **d** Same as (b), but with drain bias of +2.5mV. The missing part of the triangles is highlighted by dashed lines.

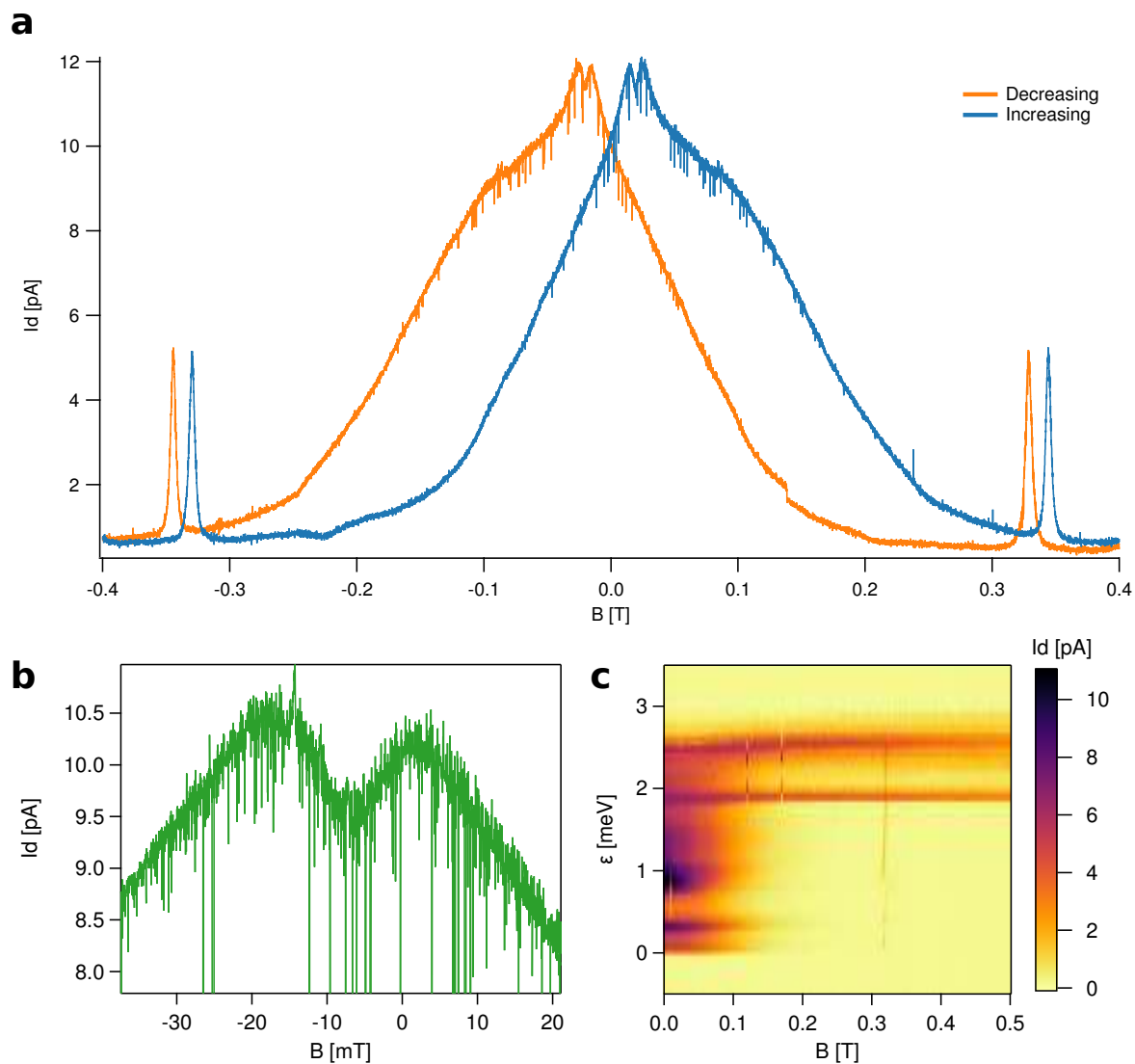


Figure 2.19 Details of spin-blockade. **a** Magneto-transport measurement performed downwards and upwards. **b** Detail of the peak around zero magnetic field. We can remark a small dip. **c** High-resolution measurement of the leakage current as function of magnetic field.



## 2.5 Electron Dipole-induced Spin Resonance

Magnetic resonance is the phenomenon of inducing transition among the non-degenerate levels of a spin system split by an external magnetic field. Electron Spin Resonance (ESR, also known as Electron Paramagnetic Resonance, EPR) is the magnetic resonance carried on an ensemble of electronic spins. In this thesis the discussion will be limited to the magnetic resonance carried on a single electronic spin confined in a silicon quantum dot.

The Hamiltonian for a spin in a static magnetic field is given by

$$\hat{H}_I = -\hat{\boldsymbol{\mu}}_J \cdot \mathbf{B}_0$$

where  $\hat{\boldsymbol{\mu}}_J$  is the magnetic moment operator associated to a generic angular momentum operator  $\hat{\mathbf{J}}$ . They are linked by a linear relation

$$\hat{\boldsymbol{\mu}}_J = -\frac{\mu_B}{\hbar} g \hat{\mathbf{J}}$$

where  $g$ , the proportionality term, is the  $g$ -factor. By taking  $\mathbf{B} = B_0^z \mathbf{k}$ ,  $\hat{H}_I$  is simplified to

$$\hat{H}_I = -\mu_z B_0^z = \frac{\mu_B g \hat{J}_z B_0^z}{\hbar}$$

If we develop the Hamiltonian using perturbation theory, using the eigenstates of the angular momentum

$$\mathbf{J}^2 |j, m_j\rangle = \hbar^2 j(j+1) |j, m_j\rangle$$

$$\hat{J}_z |j, m_j\rangle = \hbar m_j |j, m_j\rangle$$

we get the Zeeman energy

$$E^{(1)} = \langle j, m_j | \frac{\mu_B g \hat{J}_z B_0^z}{\hbar} | j, m_j \rangle = \mu_B B_0^z m_j$$

with  $m_j$  that can assume all the  $n = 2j + 1$  values from  $-j$  to  $+j$ . If we take the angular momentum of an electron,  $S=1/2$ , the eigenstates  $|\downarrow\rangle$  and  $|\uparrow\rangle$  will have energies

$$E_{\downarrow} = -\frac{1}{2} \mu_B g B_0^z$$

$$E_{\uparrow} = \frac{1}{2} \mu_B g B_0^z$$

The transition from the lower state to the upper one can be driven by one photon with the right energy

$$\Delta E = h\nu = \mu_B g B_0^z \quad (2.3)$$

This is the ESR equation, and for a magnetic resonance transition it predicts a linear relation between magnetic field and frequency. If we analyze the equation of motion semiclassically, the rate of change in angular momentum is given by [79]

$$\frac{d\mathbf{J}}{dt} = \boldsymbol{\mu} \times \mathbf{B}_0$$

or

$$\frac{d\boldsymbol{\mu}}{dt} = \boldsymbol{\mu} \times \left( \frac{g\mu_b \mathbf{B}_0}{\hbar} \right) \quad (2.4)$$

This equation tell us that in a static magnetic field, the magnetic moment precess around the axis of the magnetic field at the *Larmor frequency*

$$\omega_L = \frac{g\mu_b \mathbf{B}_0}{\hbar}$$

It's useful to define a new reference frame, called *rotating frame*, which rotates around the static magnetic field at the Larmor frequency. In the rotating frame, the effective magnetic field is given by

$$\mathbf{B}_{eff} = \mathbf{B} - \frac{\boldsymbol{\omega}}{g\mu_B}$$

Under the effect of only a static field, the orientation of the magnetic moment is fixed in the rotating frame, since the effective magnetic field will be zero.

Now, if we add an oscillating magnetic field in the xy (using the rotating wave approximation), thus perpendicular to the static magnetic field

$$\mathbf{B}_1(t) = B_1(\mathbf{i} \cos \omega t + \mathbf{j} \sin \omega t)$$

the effective magnetic field in the rotating frame (figure 2.20) will be

$$\mathbf{B}_{eff} = \mathbf{k}(B_0^z - \frac{\omega}{g\mu_B}) + B_1\mathbf{i}$$

The magnetic moment would not be static anymore, and it will precess, in the rotating frame around  $\mathbf{B}_{eff}$ . If  $\omega = \omega_L$ , the effective magnetic field is equal to  $B_1$ ; the magnetic moment will precess from -z to z at the Rabi frequency  $\omega_R = \mu_B g B_1$ . The resonance condition is fulfilled and is same as the ESR equation 2.3.

To summarize, to have the resonance condition, the  $\mathbf{B}_1$  must be perpendicular to the static magnetic field  $\mathbf{B}_0$ , otherwise no torque would be applied to the magnetic moment and no spin rotation can be induced. Also, it must be stressed that in principle only an oscillating magnetic field can induce spin rotations; an electric field can not generate the torque moment to acts on the spin orientation. In order to drive the spin orientation with an electric field, a different coupling between the electric field and the spin is needed. In this case, we talk about *Electric Dipole-Induce Spin Resonance* (EDSR).

Since our momentum is the result of a two-state spin system, it's convenient to introduce the representation of the *Bloch Sphere* (see figure 2.21). It's a geometric representation of eigenstates for a two-states system. The poles represents the two basis vectors, usually identified as  $|0\rangle$  and  $|1\rangle$ . Any state that is a superposition of these two, is written as

$$|\varphi\rangle = \alpha|0\rangle + \beta|1\rangle = \cos(\theta/2)|0\rangle + e^{i\phi}\sin(\theta/2)|1\rangle$$

The surface of the sphere represents all the possible states.  $\theta$  (latitude) represents the proportion of the pure states, while  $\phi$  (longitude) the phase.

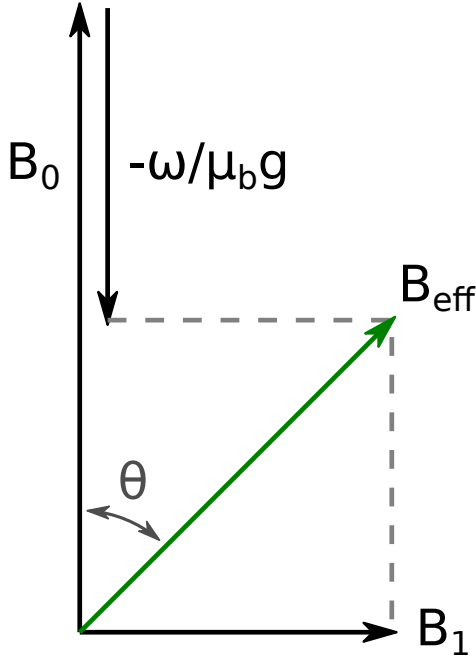


Figure 2.20 Effective magnetic field in the rotating frame

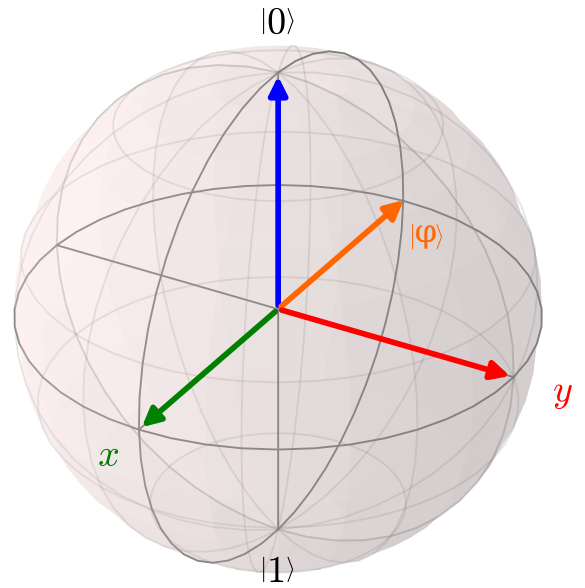


Figure 2.21 Bloch sphere

### 2.5.1 Relaxation phenomena and Bloch equations

So far the spin has been considered as isolated, without any interaction with the environment. In reality, since the spin is hosted in a lattice, it will interact with the environment. The semiclassical equation of motion 2.4 can be modified to take into account the relaxation phenomena:

$$\begin{aligned}\frac{d\mu_x}{dt} &= \mu_b g (\mathbf{B}_0 \times \boldsymbol{\mu})_x - \frac{\mu_x}{\tau_2} \\ \frac{d\mu_y}{dt} &= \mu_b g (\mathbf{B}_0 \times \boldsymbol{\mu})_y - \frac{\mu_y}{\tau_2} \\ \frac{d\mu_z}{dt} &= \mu_b g (\mathbf{B}_0 \times \boldsymbol{\mu})_z - \frac{\mu_z^0 - \mu_z}{\tau_1}\end{aligned}\tag{2.5}$$

We define two phenomenological relaxation times  $\tau_1$ , the transverse relaxation time (also called lattice-spin) and  $\tau_2$ , the longitudinal relaxation time (also called spin-spin). The first one takes into account the relaxation phenomena with an exchange of energy with the environment. Under the effect of a static magnetic field only, their effect manifests as a reduction of the precession amplitude around  $\mathbf{B}_0$ , until  $\boldsymbol{\mu}$  is fully aligned with  $\mathbf{B}_0$ . On the contrary,  $\tau_2$  takes into account all phenomena that doesn't involve an energy transfer with the environment, thus all decoherence phenomena that affect the quantum phase. It affects the transverse component of the magnetization. These times are not equal, and  $2\tau_1 \geq \tau_2$  [14]. Random fluctuations of the magnetic environment (such as the Overhauser field) doesn't contribute directly to the dephasing, but affects the coherence time as well, since the spin feels different magnetic field over the resonance experiment. The effect of these variations is taken into account in the time  $\tau_2^*$ , which is the effective  $\tau_2$  measured when the experiment is averaged over a large number of samples of measurements or in continuous wave mode. It's possible to suppress these effects by refocusing the spin using the spin echo technique [80].  $\tau_2^*$  is always bigger than  $\tau_2$ .

### 2.5.2 Continuous-Wave Spin Resonance

The simplest form of spin-resonance scheme is the continuous-wave (CW) one. The excitation to drive the spin comes from a time-uniform microwave signal applied to one of the gates. An external magnetic field is applied to Zeeman split the spin levels. Readout is performed by spin-blockade. If the system is spin-blocked, at finite magnetic field, it will be in the  $T_-^{11}$  state (which is the ground state). If we excite the transition to the unblocked state  $S^{11}$ , spin-blockade will be lifted and a peak appears under resonant condition. Frequency of mi-

crowave and magnetic field are swept in order to look for the ESR condition of equation 2.3.

In a 2D measurement of current as function of magnetic field and microwave frequency,

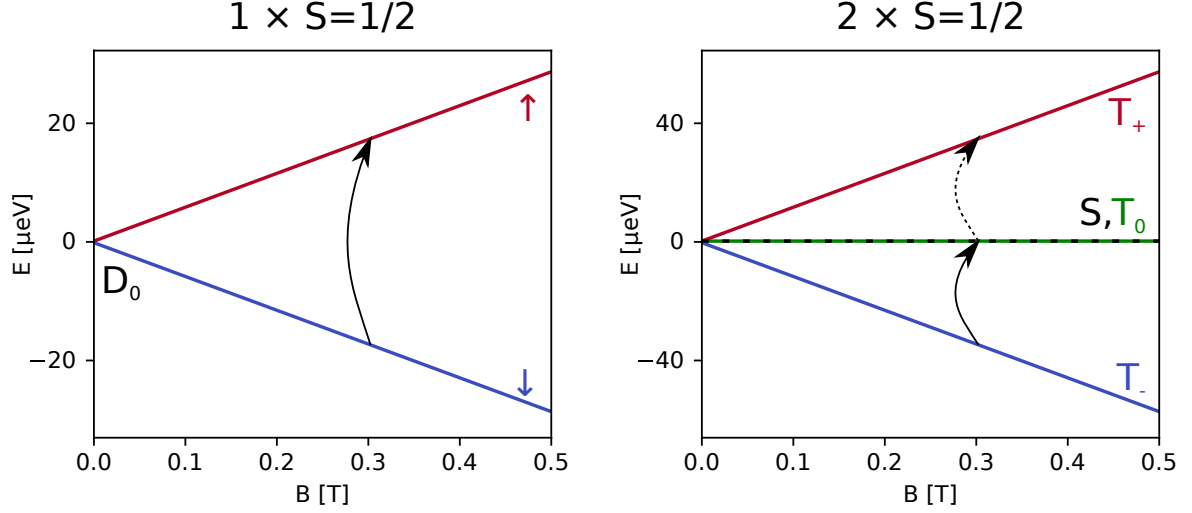


Figure 2.22 Schematics of energy levels for one(left) and two(right) spin  $1/2$  as function of magnetic field. Arrows indicate possible ESR transitions

the signature of spin resonance will be a straight line with slope  $\mu_b/hg$ . In figure 2.23a is reported this measurement for a microwave signal applied on the RF antenna. We can clearly see a straight line that we can attribute to a spin resonance with a  $g$  factor of 2.02. This value is compatible with the  $g$  factor for free electrons in bulk silicon  $g = 1.99875 \pm 0.0001$  [81, 82]. Surprisingly, if we apply the same signal to the gate 2 instead of the RF gate (figure 2.23b), we can see a very similar spin resonance appears. The magnetic field generated by an electrostatic gate is supposed to be negligible, since contrary to the special designed RF line, there is no path for a current to flow. Also, as rough estimate, the unblocked current should be between one and three times of the Rabi frequency. In the ideal case, in one  $\pi$  period, the spin-blockade should be lifted and one electron should pass. After the unblocking event, the system can let pass few electrons before being unblocked (electron can enter either in the blocking singlet state or in one of the three blocking triplet states, see [83]). In section 2.1.1 we estimated a Rabi frequency of 14kHz, so the unblocked current for  $\Gamma_{SD}, t \gg I_{ESR}$  should be between 2 and 6 fA, but we measure several hundreds of fA. The similarity of the results for both gates geometries and the facts that the signal seems too strong for a purely magnetic spin manipulation, suggest that we are in the presence of a Electron Dipole-induced Spin Resonance. We discuss the possible mechanism in section 2.8.

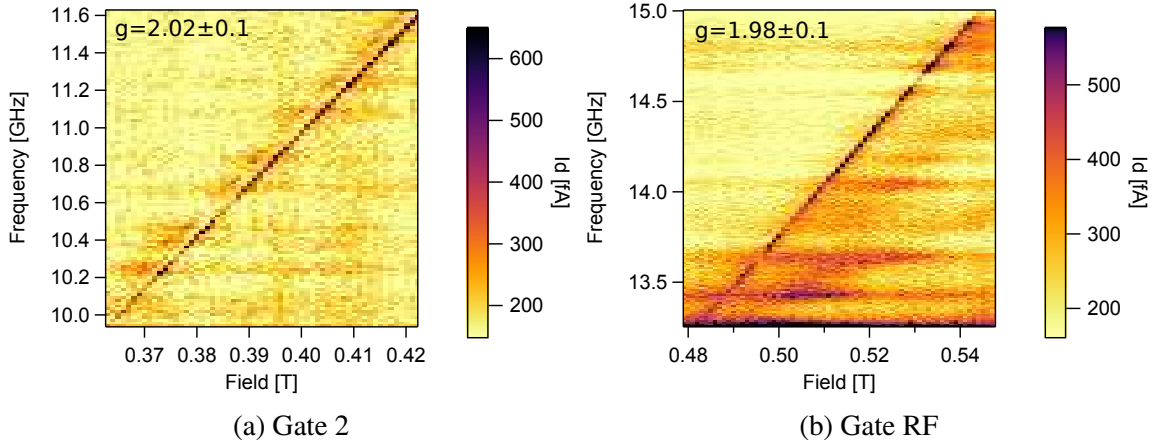


Figure 2.23 EDSR spectra recorded as function of magnetic field and microwave frequency. The straight line is the resonance signal. Microwave excitation in the two plots has been applied on different gates

### Relaxation times

In order to study the coherence times, we measured the resonance line at different microwave powers [14, 84, 67]. If the Bloch equations 2.5 are still valid and homogeneous line broadening, the lineshape is a lorentzian[85]

$$Y(B) = \frac{y_m^0}{1 + [(B - B_0)/\sigma_B/2]^2} \quad (2.6)$$

where  $y_m^0$  is the amplitude of the line,  $B_0$  the resonant field and  $\sigma_B$  is the full-width at half-maximum (FWHM). If we rewrite this formula in terms of relaxations time  $\tau_1$  and  $\tau_2$  we get

$$Y(B) = \frac{s B_1 y_m^0}{1 + s(B - B_0)^2 (g\mu_B/\hbar)^2 \tau_2} \quad (2.7)$$

with the *saturation factor*  $s$  defined as

$$s = \frac{1}{1 + B_1^2 (g\mu_B/\hbar)^2 \tau_1 \tau_2} \quad (2.8)$$

Saturation happens when the system is excited on a rate bigger than  $1/\tau_1$  relaxation rate. If the power is increased over the saturation, the intensity of the line is supposed to reach a maximum and then decrease. At very low power, the system relax faster than the excitation rate; in this case  $s \approx 1$  and the linewidth is inversely proportional to transverse relaxation

time  $\tau_2$

$$\tau_2 = \frac{2\hbar}{g\mu_b\sigma_B} \quad (2.9)$$

and for a line recorded as function of microwave frequency

$$\tau_2 = \frac{2\sqrt{\ln 2}}{\pi\sigma_f} \quad (2.10)$$

In figure 2.25 is reported the ideal behaviour for an line as function of power in the case of homogeneous line broadening. As expected, at low power the linewidth is almost constant and the line intensity is linear with the power. When  $s$  drops to 0.5, the width starts to increase linearly with the power, and the intensity drops. In figure 2.24a is reported such measurement for an excitation on the Gate 2, while in 2.24b the same but with the excitation on the RF gate. We remark that in both of the cases the amplitude reach a maximum value and then drops, like in the ideal case. For the linewidth, the behaviour is different, since for the measurement on gate 2 it increase linearly, as expected, while in the other case it stay almost constant for low power and slightly increase. We believe that in the latter case we are well below of saturation and the hypothesis of homogeneous broadening doesn't hold anymore. Photon assisted tunnelling starts to play a role in broadening; in fact, the baseline current (not shown) increases as well. The difference of the two measurements can be explained by the different working point to have a spin resonance with different excitation and by the different coupling that the two gates have. The first one is useful to spot the saturation point at high power, while the second one is useful to look for the minimal linewidth. We performed a very low speed measurement to properly reconstruct the shape of resonance line and fit to extract the  $\tau_2$ . Since it's a CW measurement, it's more correct to talk about  $\tau_2^*$ . By sweeping the magnetic field (at  $f=9.4$  GHz) and then the frequency (at  $B=343.5$  mT) we got two similar coherence times (figure 2.26)

$$\begin{aligned} \tau_2^*(B) &= \frac{2\hbar}{g\mu_b\sigma_B} = 36\text{ns} & \sigma_B &= 0.324\text{mT} \\ \tau_2^*(f) &= \frac{2\sqrt{\ln 2}}{\pi\sigma_f} = 46\text{ns} & \sigma_f &= 11.31\text{MHz} \end{aligned}$$

### Anisotropy

To further investigate the nature of our EDSR signal, we rotated the magnetic field angle and studied the evolution of the resonance peak. In a solid, the magnetic field felt by the spin

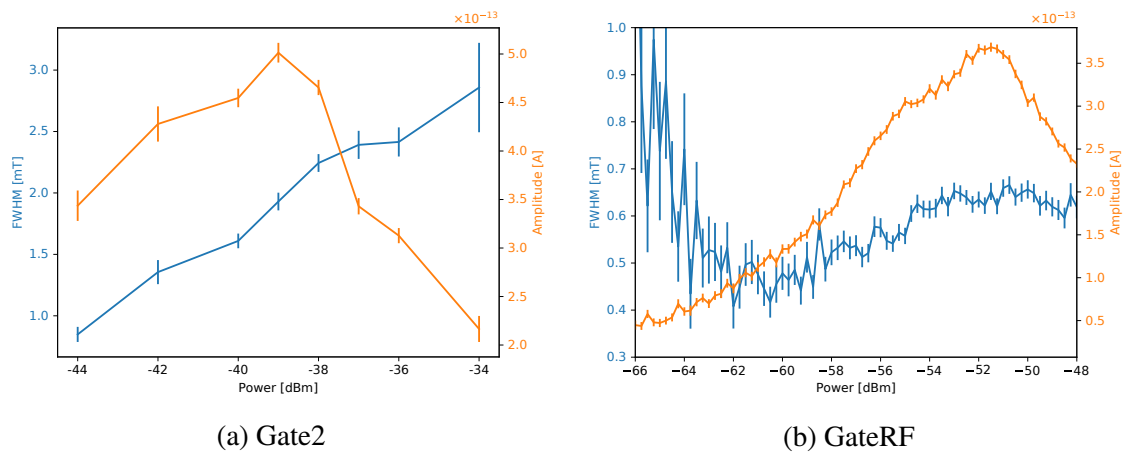


Figure 2.24 Resonance amplitude and width as function of applied power. Microwave excitation in the two plots has been applied on different gates

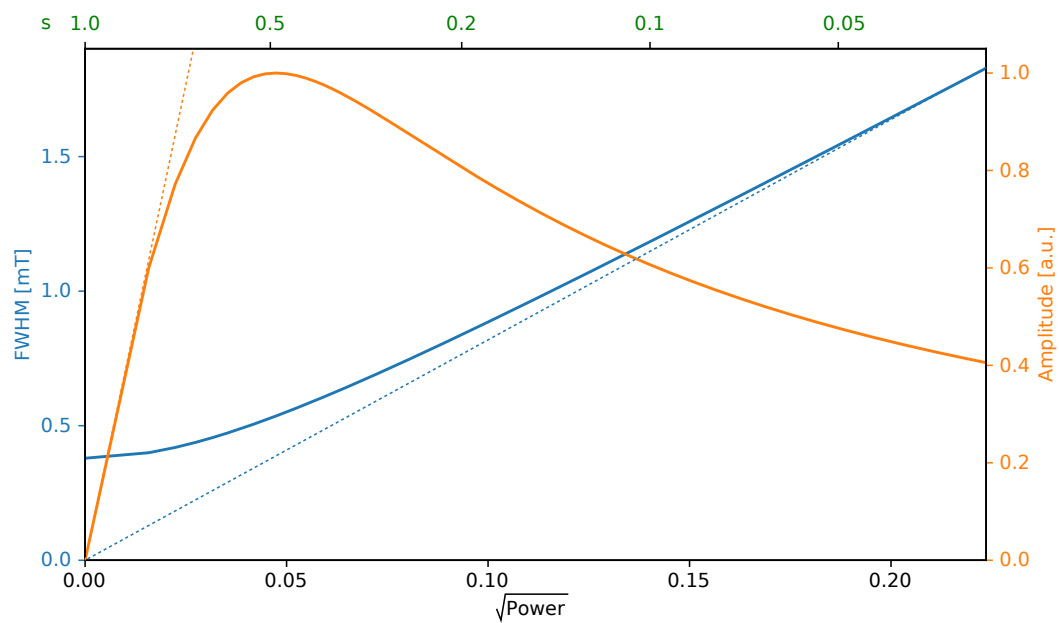


Figure 2.25 Simulation of resonance amplitude and width as function of power around the saturation point



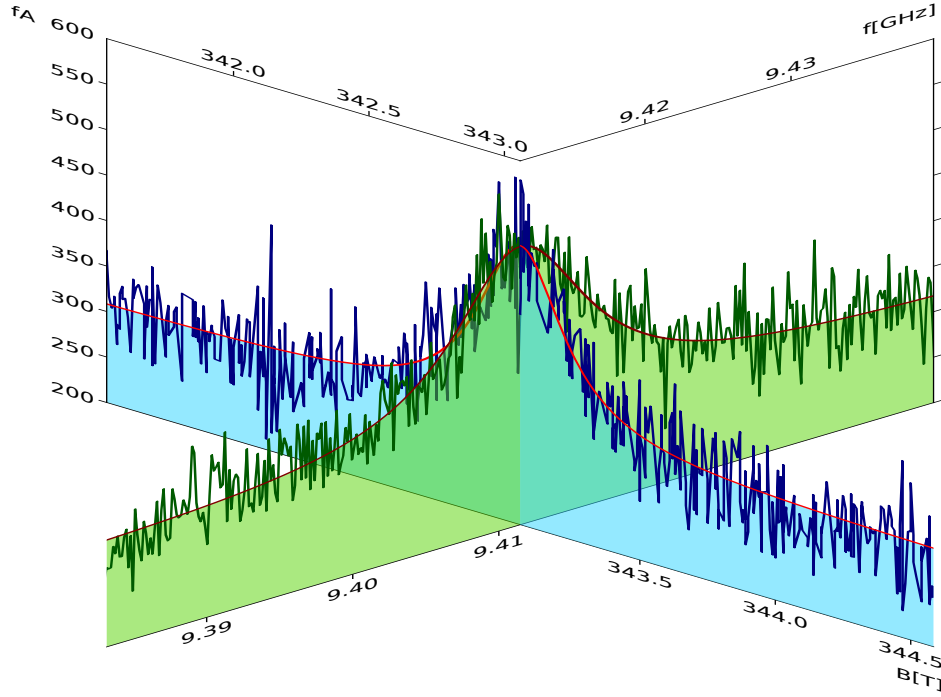


Figure 2.26 Linewidth at minimal power. Resonance has been measured as function of magnetic field (blue line) and microwave frequency (green line)

is different from the external one, because of the local magnetic field that arise in a lattice. It's convenient to group all these effect the the  $g$  factor, which will be the different from the electron  $g$ -factor  $g_e \simeq -2.0023$ . The  $g$  factor will not be a scalar anymore, but it will be a 2nd rank symmetric tensor, so it means that the  $g$  factor will depend on the direction of the magnetic field. In the case of a spin confined in a quantum dot it may be linked to the dot shape. For a given direction  $(x', y', z')$  we get

$$\mathbf{g} = \begin{bmatrix} g'_{x',x'} & g'_{x',y'} & g'_{x',z'} \\ g'_{y',x'} & g'_{y',y'} & g'_{y',z'} \\ g'_{z',x'} & g'_{z',y'} & g'_{z',z'} \end{bmatrix} \quad (2.11)$$

with the Zeeman Hamiltonian written as

$$H_z = \frac{\mu_B}{\hbar} \mathbf{B} \cdot \mathbf{g} \cdot \mathbf{S} \quad (2.12)$$

It's always possible to find the principal axis  $(x, y, z)$  and then diagonalize  $\mathbf{b}$ , with diagonal elements  $g_x, g_y, g_z$ . By exploring the evolution of the EDSR position at different orientations of the static magnetic field, we can reconstruct the  $g$ -tensor. In the case of an uniaxial

symmetry we will have

$$g_{\parallel} = g_z$$

$$g_{\perp} = g_x = g_y$$

and by explicating the angle between the principal axis and the magnetic field we get

$$g^2 = g_{\perp}^2 \sin^2 \theta + g_{\parallel}^2 \cos^2 \theta \quad (2.13)$$

The magnetic field was always in the same plane as the nanowire; the angle is relative to the nanowire axis, counter-clockwise. The nanowire was etched with the [110] orientation A.1. So zero degrees means a field parallel to the nanowire in the [110] direction, while ninety degrees means a field perpendicular to the nanowire in the  $[\bar{1}10]$  direction. Due to imprecision in the placement of the sample, there is a misalignment of about  $5^\circ$ ; the magnetic field will have a small out-of-plane component.

In figure 2.27a is reported the measurement of an EDSR peak as function of the angle over a range of  $180^\circ$ . The resonance position oscillates from a minimum of 373mT to a maximum of 400mT, which correspond respectively to g factor of 1.99 and 1.84. These values are slightly off from the values calculated in section 2.5.2; this is because in that case the g factor is a measurement of slope, while here is proportional to the ratio of field and frequency. If the line doesn't pass exactly from the origin, the two values doesn't match perfectly. The variation of the g factor are pretty big, considering that in literature these variations are much smaller [82, 86, 87]. We believe that this oscillations are mostly due artefacts of the setup. The zero field of the magnets is not properly calibrated, and an offset on both coils can lead to an apparent oscillations of the resonance position as respect to the angle. Moreover, the hysteresis seen in section 2.4.3 can make the evaluation even more difficult. In fact we can see that the local minima have different position, which is in disagreement with equation 2.13 and could be a direct consequence of sample hysteresis. Apparently the peak position (line light blue figure 2.27b) doesn't follow the trivial functional form of equation 2.13. Therefore, since we can't properly evaluate the g-tensor, and given that the variation are supposed to be small from literature, in the following analysis we will use the isotropic g-factor calculated from the line slope, as section 2.5.2.

On the contrary, the intensity of the resonance (orange line) follows a clear sinusoidal form. By fitting it with [87]

$$I(\theta) = A_0 + A \sin(\theta + \theta_0)^2$$

we get a good agreement with fit parameters

$A_0$	$(0.49 \pm 0.01)\text{pA}$
$A$	$(1.07 \pm 0.01)\text{pA}$
$\theta_0$	$(-2.7 \pm 0.4)\text{deg}$

We can see that we get the minimum amplitude when the field is parallel to the nanowire (zero degrees) and it has its maximum when it gets perpendicular (ninety degrees). This behaviour is in accordance with the theoretical predictions in paragraph 2.8.2.

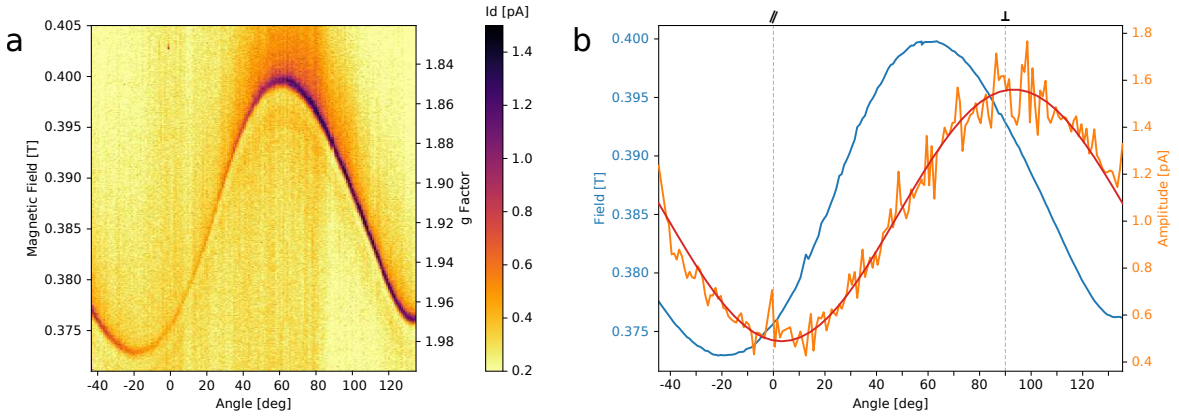


Figure 2.27 Spin resonance as function of the angle of in-plane magnetic respect to the nanowire axis. In the left panel the raw measurement, in the right one measured resonance position(blue) and amplitude(orange), with a fit for the amplitude(red)

### Double peak

When the visibility of the resonance peak is high enough, at some point in the frequency vs. field plot, a second peak appears. This peak is very close to the main one and much less intense. If we take two measurements at different frequencies, we can see that the spacing of this peak is always the same, so this resonance line run parallel to the first one, ie. they have the same g factor (see figure 2.28). A first hypothesis is the hyperfine interaction with a localized arsenic donor. The Hamiltonian for this interaction is

$$H_{HF} = \mathbf{I} \cdot \mathbf{A} \cdot \mathbf{S}$$

where  $\mathbf{I}$  and  $\mathbf{S}$  are the operators for the nuclear and electron spin, while  $\mathbf{A}$  is a second-rank tensor describing the hyperfine interaction. If we restrict ourselves to the isotropic Fermi contact interaction we get

$$H_{HF} = -\frac{2}{3} \mu_0 |\psi(0)|^2 \boldsymbol{\mu}_e \cdot \boldsymbol{\mu}_n = \frac{2}{3} \frac{\mu_0}{\hbar^2} |\psi(0)|^2 \mu_B g_e \mu_N g_N \mathbf{S} \cdot \mathbf{I}$$

where  $|\psi(0)|^2$  is the overlap of the electron wavefunction with the arsenic nucleus. The *hyperfine coupling constant*  $A_0$  is

$$A_0 = \frac{2}{3} \frac{\mu_0}{\hbar^2} |\psi(0)|^2 \mu_B g_e \mu_N g_N$$

The hyperfine interaction should manifest itself as  $n = 2I + 1$  equally spaced peaks, with the total peak spacing given by  $A_0$  (so spacing between each peak equal to  $A_0/n$ ). The nuclear spin of arsenic is  $3/2$ , so we expect  $n = 2I + 1 = 4$  peaks. As stated before, the hyperfine coupling constant depends on the overlap of the wavefunction with the nucleus, so it can be reduced from its expected bulk value in the case of something that alter the shape of the wavefunction. For arsenic dopants in bulk silicon  $A_0 = 198.35 \text{ MHz}$  [81]. In our case we see only two peaks over the expected four, and their distance (3mT, which is equivalent to 83MHz) is too big to be compatible with an hyperfine interaction.

Another possibility is the exchange interaction between the spin in the two different dots. As explained in the modelling in section 2.6, the effect of the exchange interaction is to remove the degeneracy between the  $S^{11}$  and  $T_0^{11}$  states. We attribute the main line as the  $T_-^{11} \rightarrow S^{11}$  transition, which lifts the spin-blockade directly. The smaller peak is attributed to the  $T_-^{11} \rightarrow T_0^{11}$  transition. This transition doesn't lift the spin-blockade directly, but since the singlet and the unpolarized triplet are close in energy, thanks to the spin-orbit interaction these states are coupled and we can have an indirect lifting. The peak is smaller due to this second-order process [88]. The measured exchange interaction in this case is

$$E_J = \mu_b g \Delta B = 0.34 \mu eV$$

Another possibility is that the two dots feels a different magnetic field (see section 2.8.1 for possibles origins of magnetic field gradient). While having the same  $g$  factor (same slope) the resonant field for the two electron would be then different. Thus different lines can be attributed to the rotation of the spin in different dots. The transition can be  $T_-^{11} \rightarrow \downarrow \uparrow^{11}$  or  $T_-^{11} \rightarrow \uparrow \downarrow^{11}$ . In both of the case, the arriving state has a singlet component, thus a way to escape the (0,2) state [89]. The problem with this hypothesis is to explain the origin of such difference in field between the two dots.

## 2.6 Spin-Valley Resonance

In figures 2.23a and 2.23b we presented a zoom on the EDSR line; the particularity of this line is that if we prologue it to reach it the axis of frequency, it will pass almost through the origin of the frequency/field plane. In others words, there is no zero field splitting. The global

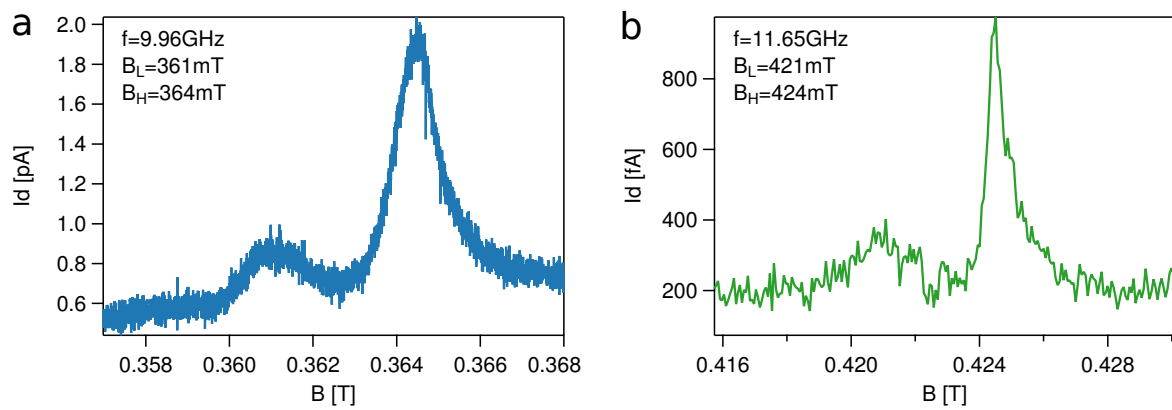


Figure 2.28 Double peak of resonance, for two different frequencies

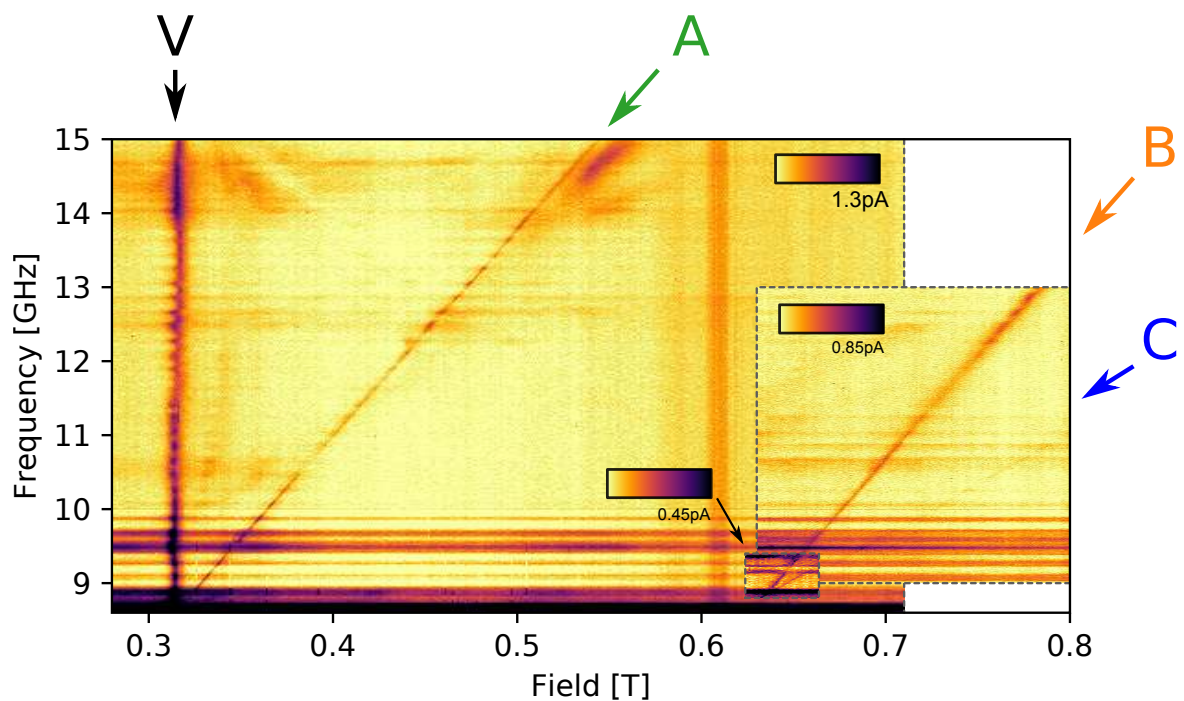


Figure 2.29 Extended measurements of spin resonance. Three different measurements are put together for clarity.

picture in fact is composed by several lines, with different slopes and/or offset on the axes. In figure 2.29 is reported a global view with all the lines resolved. It's a collage of different measurements to highlight the different lines. Except for the regularly spaced horizontal lines, which are due to standing waves in the cables and/or PAT, we can recognize four lines, which are labelled A,B,C,V. In addition to the slope, we calculated also the offset of the line on the frequency axis, called *zero-field splitting*. Thus the EDSR equation is slightly modified to

$$h\nu = \mu_B g B_0^z + D \quad (2.14)$$

and the results are

Line	g	D [ $\mu\text{eV}$ ]
A	$1.980 \pm 0.005$	$-0.36 \pm 0.1$
B	$2.00 \pm 0.01$	$-36.8 \pm 0.5$
C	$0.96 \pm 0.01$	$-0.8 \pm 0.5$

The vertical line V is not function of the microwave frequency, and it's visible also without a microwave signal (see paragraph 2.4.3). It appears as a peak at  $B_V = 0.314 \pm 0.001$  mT (see paragraph 2.6.1). The other vertical line at around 0.6T is an artefact of the measurement. The line A is the one already studied, with  $g = 1.97$  and zero-field splitting. Line B has a  $g$  factor very close to the one of line A, but a zero field splitting of  $-36.9\mu\text{eV}$ . We attribute this line to an intervalley transition, with a valley-splitting equal to the zero field splitting. In figure 2.30a the energy level for a system of one electron with spin 1/2, with two possible valley states (valley  $\pm z$ , indicated with 1 and 2). A small Rashba spin-orbit interaction  $H_{SO}$  smaller than the Zeeman energy is included. The modelization of this interaction is useful to couple the states in a similar way to a real spin-orbit hamiltonian. The Hamiltonian is

$$\begin{aligned}
 H &= H_Z \otimes \mathbb{1} + \mathbb{1} \otimes H_V + H_{SO} \\
 H_Z &= \frac{1}{2} \mu_B g \sigma_z \\
 H_V &= \frac{1}{2} \Delta E_V \sigma_z
 \end{aligned} \quad (2.15)$$

where  $\sigma$  are the Pauli matrices. In figure 2.30a are represented the eigenenergies as function of magnetic field. The colour is proportional to the expectation value of the  $\hat{S}_Z$  and  $\hat{V}_Z$  operators (defined respectively as  $\sigma_z \otimes \mathbb{1}$ ), in order to give a visual representation of spin and valley flavour of the eigenstates. In the left panel blue (red) is for spin down(up), while in the right panel violet(green) is for valley one(two). The states anticross due the spin-orbit coupling at  $B_V = \Delta E_V / \mu_B g$ . In figure 2.30b are represented the possible EDSR transitions. The green line correspond to an intra-valley transition, where the spin change its orientation,

but the valley (either 1 or 2) is conserved. This line has no zero-field splitting. Violet and red lines represents inter-valley transitions, where the valley is not conserved. The red line is for the “inner” transition  $|\uparrow, v_1\rangle \rightarrow |\downarrow, v_2\rangle$  before the anticrossing (the descending line) and  $|\downarrow, v_2\rangle \rightarrow |\uparrow, v_1\rangle$  after (the ascending one). The violet one represent the “outer” transition  $|\downarrow, v_1\rangle \rightarrow |\uparrow, v_2\rangle$ . The zero-field splitting of these lines is equal to  $\pm\Delta E_V$ . Not all these lines must be visible; the initial state must be occupied to have a transition, and only the ground state is guaranteed to be occupied. The other ones should be populated by another EDSR or pure valley transition, or have some kind of valley or spin polarization of the incoming electrons in the system.

The line V can be attributed to the mixing of the states that happens at the anticrossing field

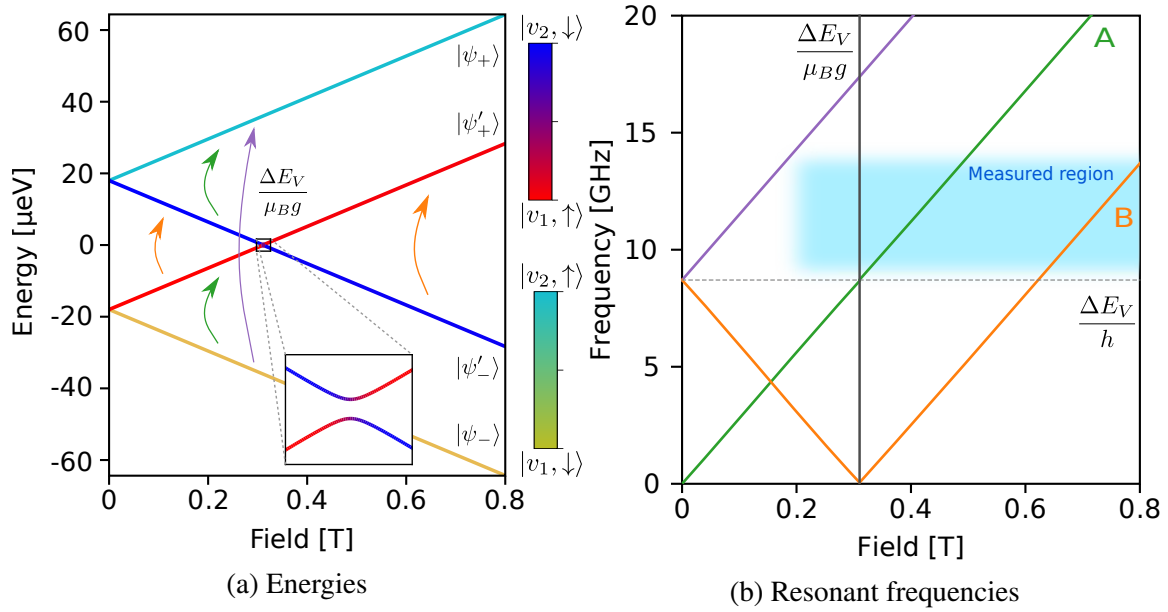


Figure 2.30 Simulations of energy and resonant frequencies as function of external magnetic field for one electron with two possible valleys

$B_V$ . At this point the states are superposition of spin up and down, so an incoming electron with a blocking spin can be effectively flipped. We conclude that lines B and V provide a measurement of the valley splitting and it's equal to 36 μeV.

This model is very simple and doesn't take into account that the system is comprised of two quantum dot, each occupied by one electron. The valley splitting depends a lot on the confinement potential, thus on the dot shape, surface roughness and proximity to interfaces. It's reasonable to assume that it will be different between the two dots. This is confirmed by the two very different measurements of the valley splitting; in section 2.3 we measured a valley splitting of 350-500 μeV with transport measurement, which is in strike contrast with

the value of 36  $\mu\text{eV}$  measured with EDSR. We attribute these two different values to valley splitting in different dots.

With these parameters, we can construct a new model with two electrons, similar to the one explained in [67]. We consider the (1,1) case

$$\begin{aligned}
 H &= H'_Z + H'_V + H_J \tag{2.16} \\
 H'_Z &= H_Z^{(1)} \otimes \mathbb{1} \otimes \mathbb{1} \otimes \mathbb{1} \\
 &\quad + \mathbb{1} \otimes H_Z^{(2)} \otimes \mathbb{1} \otimes \mathbb{1} \\
 H'_V &= \mathbb{1} \otimes \mathbb{1} \otimes H_V^{(1)} \otimes \mathbb{1} + \\
 &\quad + \mathbb{1} \otimes \mathbb{1} \otimes \mathbb{1} \otimes H_V^{(2)} \\
 H_Z^{(i)} &= \frac{1}{2} \mu_b g \sigma_z^{(i)} \\
 H_V^{(i)} &= \frac{1}{2} \Delta E_V^{(i)} \sigma_z^{(i)} \\
 H_J &= 2J[\sigma_x^{(1)} \otimes \sigma_x^{(2)} \otimes \mathbb{1} \otimes \mathbb{1} + \\
 &\quad \sigma_y^{(1)} \otimes \sigma_y^{(2)} \otimes \mathbb{1} \otimes \mathbb{1} + \\
 &\quad \sigma_z^{(1)} \otimes \sigma_z^{(2)} \otimes \mathbb{1} \otimes \mathbb{1}]
 \end{aligned}$$

For simplicity the spin-orbit interaction has been neglected for clarity; this interaction is mostly relevant at the interaction points of singlet and triplets, where it make them anti-cross. A more detailed analysis for the spin-orbit interaction (for one single dot) is in section 2.8.2. We introduced the exchange interaction between the two electrons with  $H_J$ ; this interaction is relevant only for small values of detuning and has the main effect of removing the degeneracy of singlet and unpolarized triplet.

The new sixteen states have two electron spin part, like the one defined in the equation 2.2 and a valley part (indices (1,1) are omitted)

$$\begin{array}{cccc}
 |S^{v1v1}\rangle & |T_-^{v1v1}\rangle & |T_0^{v1v1}\rangle & |T_+^{v1v1}\rangle \\
 |S^{v1v2}\rangle & |T_-^{v1v2}\rangle & |T_0^{v1v2}\rangle & |T_+^{v1v2}\rangle \\
 |S^{v2v1}\rangle & |T_-^{v2v1}\rangle & |T_0^{v2v1}\rangle & |T_+^{v2v1}\rangle \\
 |S^{v2v2}\rangle & |T_-^{v2v2}\rangle & |T_0^{v2v2}\rangle & |T_+^{v2v2}\rangle
 \end{array} \tag{2.17}$$

In figure 2.31 we show the results of a simulation with the value introduced so far (two valleys with different valley splitting). For better clarity, in the panels for  $S^2$ ,  $S_Z$  and the occupation of the valley for the first dot, only the states with the valley of the second dot (states v1v1 and



$v2v1$ ) in the ground state are shown. We can safely ignore the states  $v1v2$  and  $v2v2$ , since the Valley splitting in the second dot is very high compared to dot one. EDSR transitions among these levels are impossible to be excited since they are too energetic. Given that, for our purposes this model is very similar to the one with only one spin. One striking feature is the explication of the double line feature thanks to the exchange interaction (see 2.5.2).

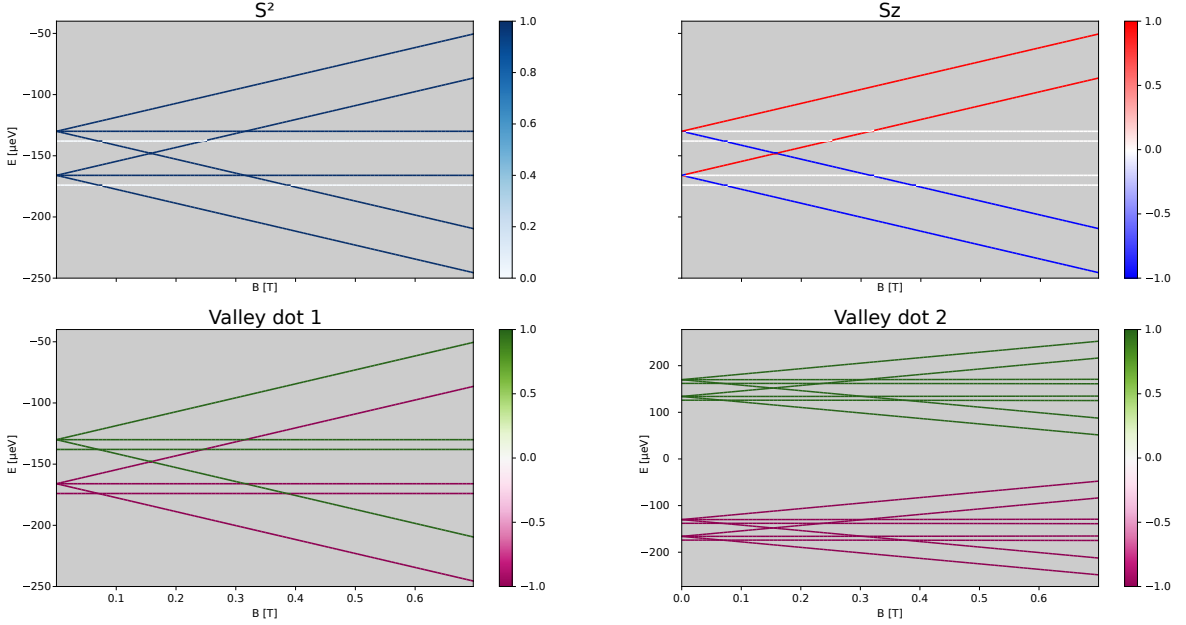


Figure 2.31 Simulation of eigenenergies as function of magnetic field for a system with two different valley splitting

The line C has a  $g$  factor which is half of the one in line A. It's also a very faint line difficult to resolve. We attribute this line to a second harmonic drive process [90, 88]. Higher harmonic processes need a non-linear system, such as a gradient of field or an anharmonic confinement potential. The shape of our dot is believed to be strongly asymmetric, due to the step that create a corner (see section 2.1, so it could be the origin of such signal.

### 2.6.1 Spin-valley blockade

In the light of the small values of valley splitting, we need to reconsider the mechanisms for the spin blockade. Since these energies are smaller than the extracted orbital singlet-triplet splitting ( $36\text{-}200\text{ }\mu\text{eV} < 1.9\text{ meV}$ ), it appears clear that the system is spin-valley-blocked. In this case, both spin and valley quantum numbers are conserved during interdot tunnelling. Otherwise, in the case of a pure spin-blockade without valley blockade, the blockade would be lifted for detuning larger than the valley-splitting of the right dot, since a triplet ( $T_{(0,2)}^{v1v2}$ ) is available for lower detuning than the orbital splitting, as explained in [67]. So the true orbital

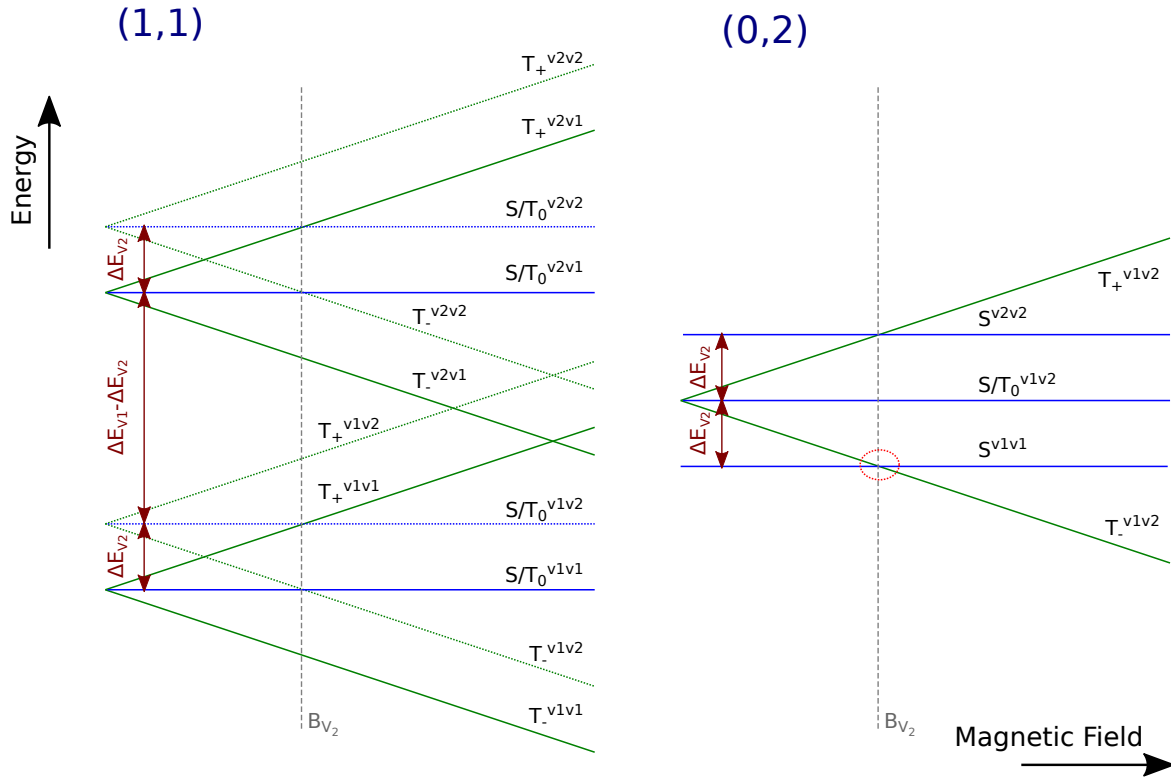


Figure 2.32 Scheme of the energy levels for a system with two dots, filled with two electrons in (1,1) and (0,2) charge states, as function of magnetic field. Different valley splitting for the two dots (respectively  $\Delta E_{V_1} > \Delta E_{V_2}$ ) are used. For clarity, spin-orbit interaction is neglected, so anticrossing features at  $B = B_{V_2}$  is missing. Triplets in the (0,2) state with both electrons in the same valley are not represented, since they are energetically far away

Singlet-Triplet splitting is thus

$$\Delta_{ST}^{orb} = \Delta_{ST} + \Delta E_{V2} = 2.1 \text{ meV} \quad (2.18)$$

This situation is better pictured in figure 2.32 it's represented a simplified scheme of levels for both the (1,1) and (0,2) charge configurations as function of magnetic field. No exchange coupling or spin-orbit interaction are included. We assign this valley splitting of about 36  $\mu\text{eV}$  as the separation of the valleys in the dot under the gate two ( $\Delta E_{V2}$ ). On the contrary, the valley-splitting of about 200  $\mu\text{eV}$  extracted in section 2.3 is the one of dot under gate number one ( $\Delta E_{V1}$ ). These values reflects the small stochastic variations of the two dots in a silicon nanowire and are confirmed to be reasonable by tight-binding simulation (see 2.8.2). Large splitting are only visible by transport measurements and small one only by spin resonance. For a large energy separation, the EDSR frequency is too high for the bandwidth of experimental setup (up to about 18GHz); transport measurement is limited by the resolution of voltage source and electron temperature, which is in the same order of magnitude as the splitting. As stated previously, Line V is only slightly affected by the application of microwaves and appears also when no microwaves are applied. It appears when the magnetic field is equal to  $B_V = 0.314 \pm 0.001$  mT. We attribute this line to a lifting of the spin-valley blockade. It appears to happen at the anticrossing point of eigenstates due to the spin-orbit interaction. Supposing the same g-factor as line A, we get that  $B_V = \frac{\Delta}{\mu_B g}$  and we can extract a valley-splitting  $\Delta E_V = 36.0 \pm 0.1$   $\mu\text{eV}$ , compatible with the value got from the fit of line B. Spin-valley blockade holds when there is **at least one** blocking state (ie. a (1,1) state that doesn't hybridize with any of the accessible (0,2) states). Triplets of (1,1) charge states with both electrons in valley one are blocking, and  $|T_-^{v1v1}\rangle$  is also the ground state. However, when  $B = B_V$ , the states  $|T_-^{v1v2}\rangle$  and  $|S^{v1v1}\rangle$  of (0,2) configuration anticross and so mix together. The resulting state can hybridize with the former blocking states, since it has a v1v1 character, as well as a triplet flavour. Similar schemes can be built for the others blocking states. No other blocking states are left, so blockade is lifted at this particular magnetic field.

## 2.7 Towards coherent control with EDSR

The experiment performed in Continuous Wave mode make the spin turn in an incoherent way. At the resonance, the spin change orientation continuously, and when it's turned by 180° it can tunnel out, with a rate governed by the tunnel rates. An incoming electron will goes into the same process, again with the randomness and the decoherence induced by the

tunnel process. So in this scheme we are not able to control the angle of the rotation. To overcome this limitation, we used a pulsed scheme where the manipulation take place in the coulomb blockade regime and the initialization and readout in spin blockade regime. This scheme was reported for the first time in [13] and it's often referred as the Koppens' scheme. The sequence is explained in the left part of figure 2.34. At the beginning, the system is in spin blockade, so it initialize to the  $T_-^{11}$  state. The time spent in this configuration should be larger than the inverse of the lowest tunnel rate, in order to assure that it will reach this configuration. Then, with a pulse on one gate (Gate 2 in our case) the system is moved to the coulomb blockade, without changing the (1,1) occupation numbers. During this phase, a burst of microwave is applied to rotate the spin. Since it's in coulomb blockade, there is no more decoherence induced by the tunnelling. Finally, the gate is pulsed back to spin blockade; if the spin turned and it formed a singlet state, the spin will unload and contribute to the detected current. Otherwise the electron stay blocked into the system without increasing the current. This sequence is repeated few millions of times to get enough electrons for a readable current. Also, repeating the measurement so many times probe the probability of being parallel or antiparallel, instead of the single event which is stochastic by nature. The burst length  $\tau$  can be varied to rotate the spin at different angles and study the evolution of the spin orientation as function of the bust time. The frequency of the oscillation of the spin alignment as function of the burst time are called Rabi Oscillation. The probability of having the spin turned is given by

$$P(\tau) = \left(\frac{\omega_1}{\Omega}\right)^2 \sin^2\left(\frac{\Omega t}{2}\right) \quad (2.19)$$

where

$$\begin{aligned} \omega_1 &= g\mu_B B_1/\hbar \\ \Omega &= \sqrt{(\omega - \omega_L)^2 + \omega_1^2} \end{aligned}$$

The resonance condition is fulfilled when  $\omega = \omega_L$ , and the oscillation will have the maximum amplitude. If we detune the applied frequency, the oscillations frequency increases, but the visibility decrease (see figure 2.33).

In our experiment the detected current would be

$$I(\tau) \simeq \frac{e}{t_{PER}} \sin^2\left(\frac{\omega_1 t}{2}\right) \quad (2.20)$$

where  $t_{PER}$  is the repetition rate of our sequence. In our case pulses are 1 $\mu$ s long, so we will have a maximum visibility of 160fA. If the initialization and readout step is not long enough to reach a steady-state spin blockade, the visibility can be reduced.

The oscillations will not last for all the possible  $\tau$ , and they will eventually dumped on a

timescale given by  $T_2^*$ . A  $\pi$  pulse is a pulse with length  $t_\pi = \pi/\omega_R$  which is able to fully reverse the spin orientation. In a similar way a  $t_{\pi/2} = \pi/2\omega_R$  is a pulse that rotate the spin in the xy equatorial plane, thus creating a state which is a superposition of spin up and down.

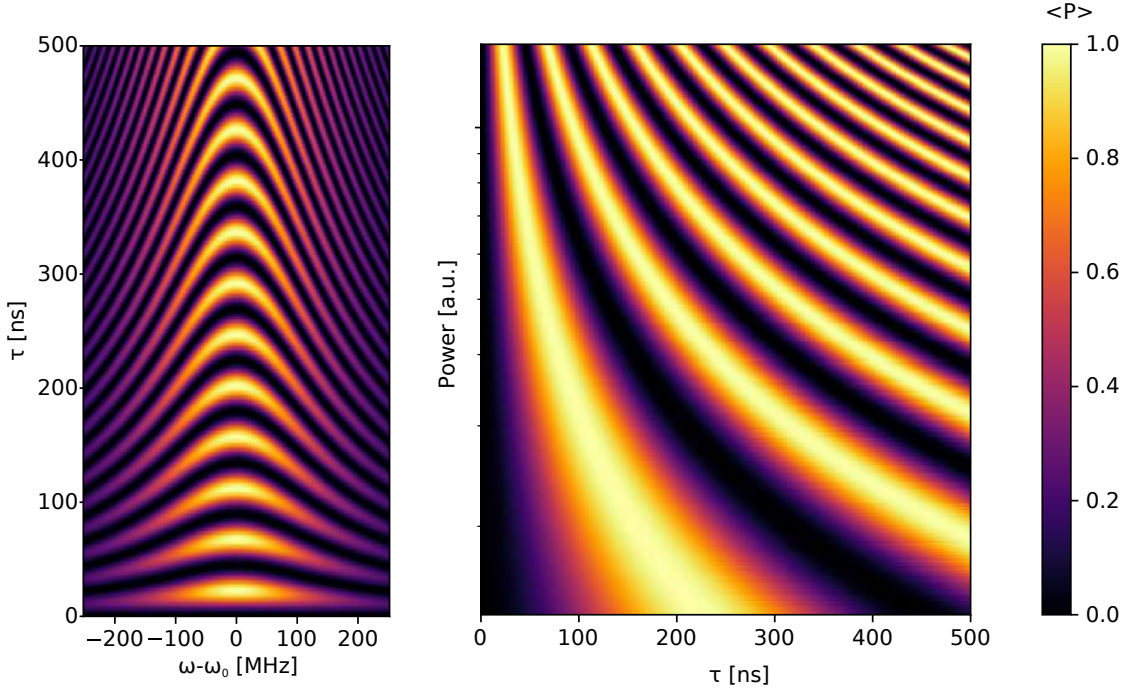


Figure 2.33 Simulation of Rabi oscillations as function of microwave detuning frequency (left) and power (right)

### 2.7.1 Setup and calibration

To implement this manipulation scheme, we need a way to pulse gate for the coulomb/spin blockade shifts and a way to generate microwave bursts.

Both pulses and burst are too fast to be delivered by the filtered DC lines, so they have been applied using the fast RF lines to the gate 2 and the gate RF (see 2.2). Pulses are generated by an Arbitrary Waveform Generator (AWG), which is able to generate fast pulses with a time resolution down to 1ns (Tektronik AWG520). The amplitude of the pulses at the sample (with the attenuation of the transmission line) is of few tens of millivolts. To calibrate the amplitude of the pulses, we recorded the bias triangles with the pulsing signal (figure 2.35 a). Since the DC measurement of the current is much slower than the pulse length (200ms against 500ns), the measurements shows two copies of the original triangle, shifted by the amplitude of the pulse. The triangle on the left(right) correspond to the positive(negative) part of the pulse; since the duty cycle of the pulse is not 50%, one of the triangle (the left one)

is more intense than the other. We will sit in the spin-blockaded region of the left triangle; in this way the system will be in spin-blockade for the initialization/readout (which last for 600ns) and in coulomb blockade for the microwave burst (which last for 400ns). We found that the attenuation of the line at 1MHz repetition rate is 7mV/V.

The bursts are generated by a mixer (Marki M8-0420MS) fed by the AWG and the microwave source (see right panel in figure 2.34). The RF port is connected to the microwave source which provide a CW source of microwave (red curve). The IF port is connected to the other port of the AWG; it generates a pulse which is “high” (2V) when the burst should be, an “low” otherwise (orange curve). In this way at the LO port, we will have the right microwave burst. Unfortunately, the mixer is not an ideal switch, since when the IF signal is low, it leaks a small, but not negligible amount of power. This parameter is called isolation and for this mixer can be as low as 25dB. If some power reaches the sample when it’s supposed to be off, the spin can rotate more than the expected. To improve it, we put two mixer in series, with the IF port connected to the AWG by a power splitter (Mini-Circuits ZFRSC-183-S+). Between the RF/LO port of the mixer we put small attenuators, in order to reduce as much as possible the reflections and standing waves. We calibrated the “low” value of the pulse with a power meter at the output, a continuous DC bias at the IF port and a microwave input power of 10dBm to saturate the mixer input; we found that the isolation can be as low as -78dB (figure 2.35 b). The two dips in the figure corresponds to the offset of each mixer. Another option to improve the isolation is to fully exploit the properties of the mixer and perform heterodyning. Instead of applying a square pulse on the IF, we can generate a low frequency burst (up to 100MHz) with the AWG; the mixer will modulate the microwave signal and at the LO port we will find two signals with respectively the sum and the difference of the two frequencies. By lowering (or increasing) the microwave frequency by the frequency of the AWG burst, the upper (lower) sideband will match the resonant frequency. In this way the leakage (with the other sideband) will not be attenuated, but it will be on a frequency away from the resonant one; at the resonant frequency there would be no power leak out of the burst. This scheme has the disadvantage that more power reach the sample, thus inducing more heating and PAT than the necessary.

The “high” value has been chosen to the maximum output of the AWG, which is 2V, in order to saturate this port and have a linear relationship between the applied power by the microwave source and the output power. In figure (figure 2.35 c) is reported the power calibration, which shows a linear relationship up to roughly +12dBm, with a loss  $\sim -16/-20$  dBm depending on the frequency.

Like in CW, we can put the microwaves either on the gate RF or on the gate 2. While the first case is trivial to implement (see figure 2.34 upper right) because the role of the pulsing gate

an the antenna are separated, the latter one requires one more step. The burst and the gate pulsing are supposed to be carried on the same line, so they need to be mixed. We used a triplexer, a power combiner with a band-pass filter for each of the three inputs (see figure 2.34 lower right). The two signals have very different bandwidths (the pulse is roughly 1MHz, plus the higher harmonics of the square step, the burst is around 10GHz) so the passband filters avoids cross-talking of the different channels.

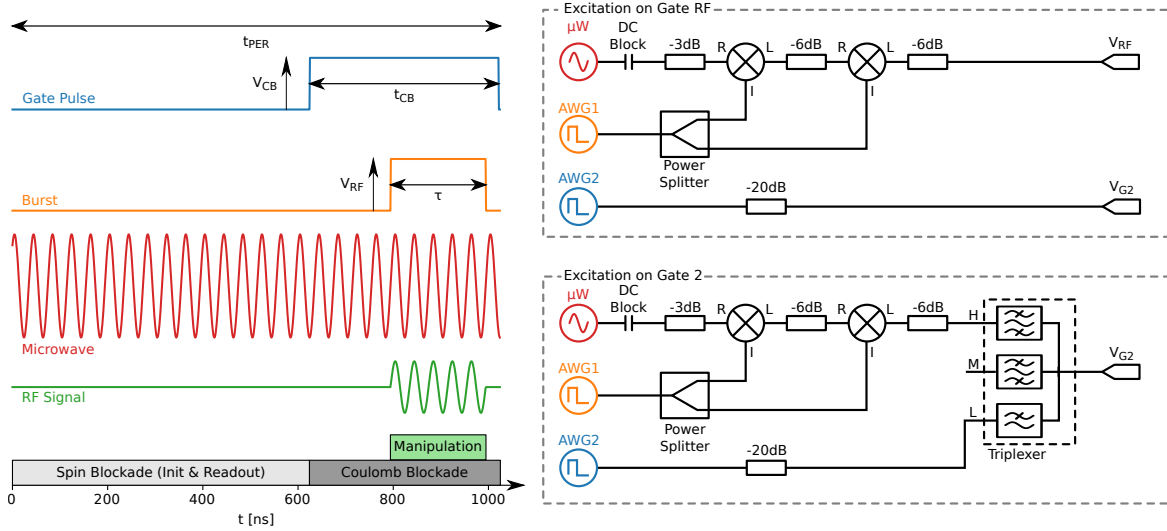


Figure 2.34 On the left a schematic of pulse sequences to drive Rabi oscillations. On the right the microwave circuits to create these pulses, for microwave bursts on the gate RF (top) and on gate 2 (bottom)

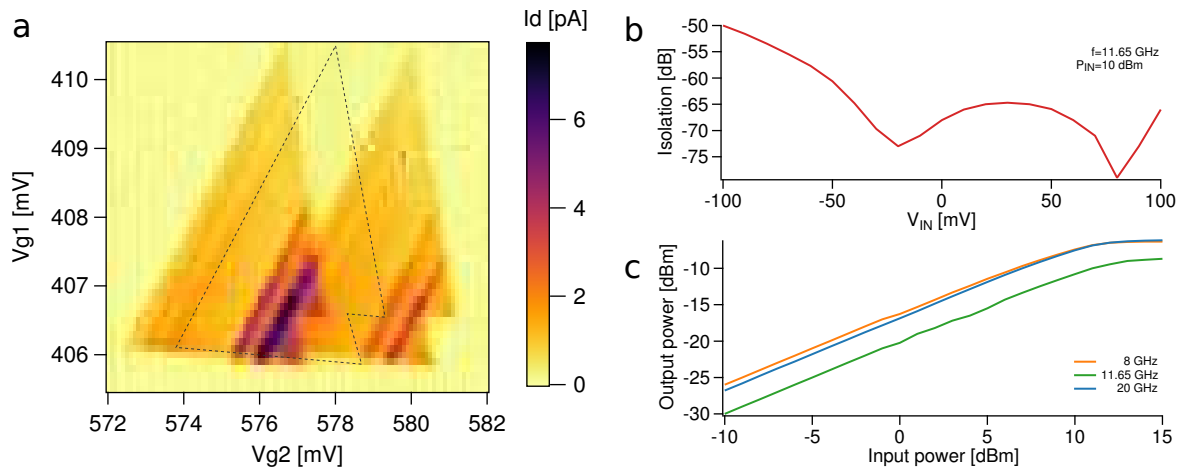


Figure 2.35 Calibrations of the microwave circuits. **a** Calibration of the pulses intensity. **b** Calibration of the mixers offset and isolation. **c** Calibration of mixers loss as function of applied power

## 2.7.2 Results

In left panel of figure 2.36 a Rabi measurement for different powers is recorded. The power is the one expected at the sample (38dB of line attenuation). The burst is applied on the RF gate, microwave frequency is 9.89GHz, magnetic field is 362mT. We can see that there is a first oscillation peak at around 100ns; its position move down in time as the power increase, as expected. If we take a cut at -35.5dBm (figure 2.36 right panel) a second oscillation is visible. If we fit this curve with the formula 2.20 we get a Rabi frequency of  $5.9 \pm 0.1$  MHz. In fact to make the fit works, we added an exponential dumping term ( $e^{-t/\gamma}$ ), which dumps the oscillations with a time constant of  $80 \pm 3$  ns, which is surprisingly short. One possible explanation is that we are not exactly at the resonant frequency, thus the oscillations have shorter period, but lower visibility and are quickly dumped.

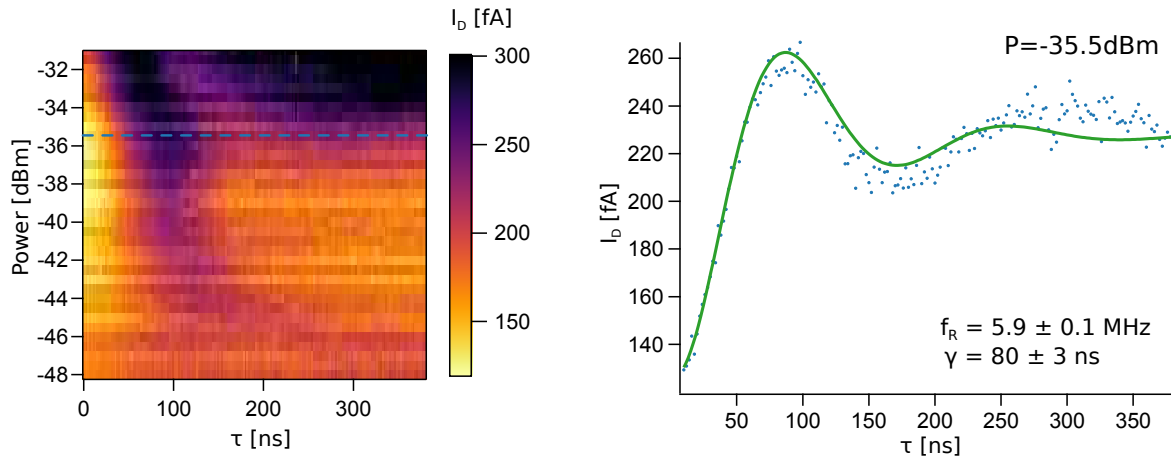


Figure 2.36 Measurement of Rabi oscillations. On the left the measurement as function of burst time and power, on the right a cut at  $P = -35.5$  dBm

## 2.8 Origin of EDSR

### 2.8.1 Permanent magnetism

A possible explanation of the EDSR signal, is the presence of materials with a permanent magnetism. In the proximity of magnetic elements, the static magnetic field would not be constant anymore, and electron in different positions in the dot would feel a field which varies as a function of the position. By displacing back and forward the electron with an electric field, in its reference frame it will feel an oscillating magnetic field, thus enabling spin manipulation [89]. In our device we found three possible parts that can create such gradient of field. The first hypothesis is a ferromagnetism of the silicide in the leads. This metal



is NiPtSi (see section A.1), and nickel is an elemental ferromagnet. However, in literature there are no report of magnetic order of its silicide [91, 92]. NiPtSi is a close relative of NiSi, since platinum is added in small quantities, so it's reasonable to assume that it will not affect the magnetic properties significantly [93].

Another candidate is the hafnium oxide in the gate stack. There are several report of ferromagnetic behaviour, principally induced by vacancies, defects and/or doping [94–96]. However, it's not an always reproducible effect (see [97]) and never reported in so thin and amorphous layer like us.

We showed in section 2.1.1 that our gates are superconducting at our working temperatures. A perfect Type-I superconductor would exhibit the Meissner effect, behaving like a perfect diamagnet and completely expelling the magnetic field. In the proximity of the superconductor the magnetic field would be “bended”, thus creating the required gradient of magnetic field. Coherent manipulation has been shown in a singlet-triplet qubit with gradient of field created by aluminium gates, see [98]. However, we have no evidences that the EDSR signal is driven by magnetism in the materials nearby the dot. It's possible to tune the properties of these material to have significant magnetic behaviour that can be exploited for electrical spin manipulation. As an example the  $\text{HfO}_2$  can be modified (polycrystalline with specific doping) to be ferromagnetic.

## 2.8.2 Spin-Orbit and Valley mixing modelling

In order to study the origin of the EDSR signal, we developed a model that take into account the spin-orbit interaction in silicon, the valley degree of freedom, the peculiar 3D geometry of the sample and the roughness of the system. It turn out that all of these factors can give rise to a significant EDSR signal. In particular, the contribution of the interaction of valley mixing and the confinement is significant. In order to simplify the spin-resonance picture, only one dot is considered. Modelling and simulation has been developed and performed by Léo Bourdet and Yann-Michel Niquet at INAC/MEM.

In the absence of valley-orbit and spin-orbit coupling, the ground state in a quantum dot is doubly degenerate in valley [20]. Valley-orbit coupling lifts this degeneracy; the resulting states are, in first approximation, bonding ( $|v_1\rangle$ ) and anti-bonding ( $|v_2\rangle$ ) linear combinations of the unperturbed degenerate ground state. They are separated in energy by  $\Delta E_V$ , the *valley splitting*.

At resonance, the Rabi frequency within valley 1 reads:

$$\hbar\nu = eV_{g,rf} |\langle v_1, \uparrow | D | v_1, \downarrow \rangle|, \quad (2.21)$$

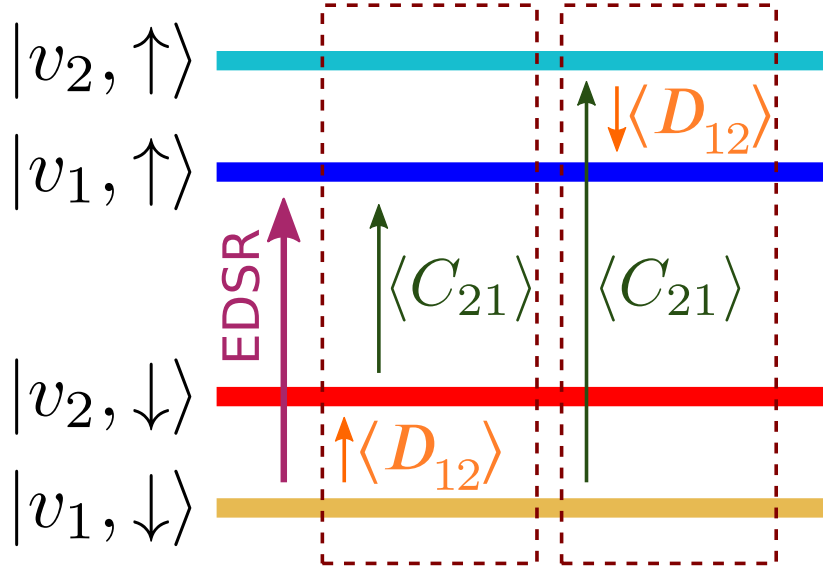


Figure 2.37 Scheme of valley levels and relevant virtual transitions

where  $V_{g,\text{rf}}$  is the amplitude of the radio-frequency (RF) modulation on the gate and  $D(\mathbf{r}) = \partial V_t(\mathbf{r})/\partial V_g$  is the derivative of the total potential  $V_t(\mathbf{r})$  in the device with respect to the gate voltage  $V_g$ . We discard the effects of the displacement currents (co-occurring ESR), which are negligible. In the absence of spin-orbit coupling,  $h\nu$  is zero as the RF field does not couple opposite spins.

The introduction of spin-orbit coupling mixes spins and valleys and yields a finite  $h\nu$ . In a perturbative picture, EDSR is assisted by virtual transitions from  $|v_1, \downarrow\rangle$  to  $|v_2, \downarrow\rangle$  (mediated by the RF field, hence by  $D(\mathbf{r})$ ), then from  $|v_2, \downarrow\rangle$  to  $|v_1, \uparrow\rangle$  (mediated by the spin-orbit coupling Hamiltonian  $H_{\text{SO}}$ ), and by virtual transitions from  $|v_1, \downarrow\rangle$  to  $|v_2, \uparrow\rangle$  (mediated by  $H_{\text{SO}}$ ), then from  $|v_2, \uparrow\rangle$  to  $|v_1, \uparrow\rangle$  (mediated by the RF field); see figure 2.37. The Rabi frequency is therefore expected to be proportional to the inter-valley matrix elements:

$$C_{21} = \langle v_2, \uparrow | H_{\text{SO}} | v_1, \downarrow \rangle = -\langle v_1, \uparrow | H_{\text{SO}} | v_2, \downarrow \rangle \quad (2.22a)$$

$$D_{12} = \langle v_1, \sigma | D | v_2, \sigma \rangle = \langle v_2, \sigma | D | v_1, \sigma \rangle \quad (2.22b)$$

The above equalities follow from time-reversal symmetry considerations for real wavefunctions.  $D_{12}$  is real and  $C_{21}$  is complex.

$C_{21}$  and  $D_{12}$  are known to be small in the conduction band of silicon. Actually,  $D_{12}$  is zero in any approximation that completely decouples the two valleys (such as the simplest effective mass approximation). It is, however, finite in tight-binding or advanced  $\mathbf{k} \cdot \mathbf{p}$  models for the conduction band of silicon. The Rabi frequency can then become significant if  $E_{1,\uparrow}$  is

close enough to  $E_{2,\downarrow}$ , because the first of the above virtual transitions is strongly enhanced. This happens when  $\Delta E_V$  is small and/or when  $g\mu_b B \approx \Delta$ .

In the simplest, non-degenerate perturbative theory, the eigenstates  $|\tilde{v}_1, \sigma\rangle$  read to first order in  $H_{SO}$ :

$$|\tilde{v}_1, \downarrow\rangle = |v_1, \downarrow\rangle + \frac{C_{21}}{E_1 - E_2 - g\mu_b B} |v_2, \uparrow\rangle + \frac{iR_{21}}{E_1 - E_2} |v_2, \downarrow\rangle \quad (2.23a)$$

$$|\tilde{v}_1, \uparrow\rangle = |v_1, \uparrow\rangle - \frac{C_{21}^*}{E_1 - E_2 + g\mu_b B} |v_2, \downarrow\rangle - \frac{iR_{21}}{E_1 - E_2} |v_2, \uparrow\rangle, \quad (2.23b)$$

with  $R_{21} = -i\langle v_2, \downarrow | H_{SO} | v_1, \downarrow \rangle$  real. We have neglected here all virtual transitions beyond the four  $|v_{1,2}, \sigma\rangle$ , because the higher orbital states are at least a few meV above the ground states. Inserting Eqs. (2.23) into Eq. (2.21), then expanding the energy denominators in powers of  $B$  yields to first order in  $B$  and  $H_{SO}$ :

$$h\nu = eV_{g,\text{rf}} |\langle \tilde{v}_1, \uparrow | D | \tilde{v}_1, \downarrow \rangle| = 2eg\mu_b B V_{g,\text{rf}} \frac{|D_{12}| |C_{21}|}{\Delta E_V^2}. \quad (2.24)$$

As expected, the Rabi frequency is proportional to  $V_{g,\text{rf}} D_{12}$ ,  $C_{21}$ , and to  $B$  (as the contributions from the  $\propto C_{21}$  terms in Eqs. (2.23) cancel out if time-reversal symmetry is not broken by the  $\propto g\mu_b B$  terms of the denominators). It is also inversely proportional to  $\Delta E_V^2$ ; namely the smallest the valley-orbit splitting, the faster the rotation of the spin (see above discussion).  $R_{21}$  does not contribute to lowest order because it couples states with the same spin.

The above equation is, nonetheless, valid only for very small magnetic fields  $B$ , as non-degenerate perturbation theory breaks down near the anti-crossing between  $E_{1,\uparrow}$  and  $E_{2,\downarrow}$  when  $g\mu_b B \approx \Delta$  (see figure 2.30a). We may, of course, deal with this anti-crossing using degenerate perturbation theory in the  $\{|v_1, \uparrow\rangle, |v_2, \downarrow\rangle\}$  subspace, while still using Eq. (2.23a) for  $|\tilde{v}_1, \downarrow\rangle$ . However, such a strategy spoils the cancellations between the contributions from  $|\tilde{v}_1, \downarrow\rangle$  and  $|\tilde{v}_1, \uparrow\rangle$  needed to achieve the proper behaviour  $h\nu \rightarrow 0$  when  $B \rightarrow 0$ . We must, therefore, deal with the SO Hamiltonian in the full  $\{|v_1, \downarrow\rangle, |v_1, \uparrow\rangle, |v_2, \downarrow\rangle, |v_2, \uparrow\rangle\}$  space.

The total Hamiltonian then reads:

$$H = \begin{pmatrix} E_1 - \frac{1}{2}g\mu_b B & 0 & -iR_{21} & C_{21}^* \\ 0 & E_1 + \frac{1}{2}g\mu_b B & -C_{21} & iR_{21} \\ iR_{21} & -C_{21}^* & E_2 - \frac{1}{2}g\mu_b B & 0 \\ C_{21} & -iR_{21} & 0 & E_2 + \frac{1}{2}g\mu_b B \end{pmatrix}. \quad (2.25)$$

As discussed before,  $R_{21}$  is not expected to make significant contributions to the Rabi frequency as it mixes states with the same spin. We may therefore set  $R_{21} = 0$  for practical purposes;  $H$  then splits into two  $2 \times 2$  blocks in the  $\{|v_1, \uparrow\rangle, |v_2, \downarrow\rangle\}$  and  $\{|v_1, \downarrow\rangle, |v_2, \uparrow\rangle\}$  subspaces. The diagonalization of the  $\{|v_1, \downarrow\rangle, |v_2, \uparrow\rangle\}$  block yields energies (see again figure 2.30a):

$$E_{\pm} = \frac{1}{2}(E_1 + E_2) \pm \frac{1}{2}\sqrt{(\Delta + g\mu_b B)^2 + 4|C_{21}|^2} \quad (2.26)$$

and eigenstates:

$$|\psi_+\rangle = \alpha|v_1, \downarrow\rangle + \beta|v_2, \uparrow\rangle \quad (2.27a)$$

$$|\psi_-\rangle = \beta|v_1, \downarrow\rangle - \alpha^*|v_2, \uparrow\rangle \quad (2.27b)$$

with:

$$\alpha = \frac{-2C_{21}}{(4|C_{21}|^2 + F^2)^{1/2}} \quad (2.28a)$$

$$\beta = \frac{F}{(4|C_{21}|^2 + F^2)^{1/2}} \quad (2.28b)$$

and:

$$F = \Delta + g\mu_b B + \sqrt{(\Delta + g\mu_b B)^2 + 4|C_{21}|^2}. \quad (2.29)$$

Likewise, the diagonalization of the  $\{|v_1, \uparrow\rangle, |v_2, \downarrow\rangle\}$  block yields energies:

$$E'_{\pm} = \frac{1}{2}(E_1 + E_2) \pm \frac{1}{2}\sqrt{(\Delta - g\mu_b B)^2 + 4|C_{21}|^2} \quad (2.30)$$

and eigenstates:

$$|\psi'_+\rangle = \alpha'|v_1, \uparrow\rangle + \beta'|v_2, \downarrow\rangle \quad (2.31a)$$

$$|\psi'_-\rangle = \beta'|v_1, \uparrow\rangle - \alpha'^*|v_2, \downarrow\rangle \quad (2.31b)$$

with:

$$\alpha' = \frac{2C_{21}^*}{(4|C_{21}|^2 + F'^2)^{1/2}} \quad (2.32a)$$

$$\beta' = \frac{F'}{(4|C_{21}|^2 + F'^2)^{1/2}} \quad (2.32b)$$

and:

$$F' = \Delta - g\mu_b B + \sqrt{(\Delta - g\mu_b B)^2 + 4|C_{21}|^2}. \quad (2.33)$$

We can finally compute the Rabi frequencies for the resonant transitions from the ground-state  $|\psi_- \rangle$  to the mixed spin and valley states  $|\psi'_\pm \rangle$  in the  $\{|v_1, \uparrow \rangle, |v_2, \downarrow \rangle\}$  subspace:

$$h\nu_- = eV_{g,\text{rf}} |\langle \psi'_- | D | \psi_- \rangle| = eV_{g,\text{rf}} |\alpha' \beta + \alpha^* \beta'| |D_{12}| \quad (2.34a)$$

$$h\nu_+ = eV_{g,\text{rf}} |\langle \psi'_+ | D | \psi_- \rangle| = eV_{g,\text{rf}} |\alpha \alpha' - \beta \beta'| |D_{12}|. \quad (2.34b)$$

We can also compute the Rabi frequency between the states  $|\psi'_\pm \rangle$  in the  $\{|v_1, +1 \rangle, |v_2, -1 \rangle\}$  subspace:

$$h\nu' = eV_{g,\text{rf}} |\langle \psi'_+ | D | \psi'_- \rangle| = eV_{g,\text{rf}} |\alpha' \beta'| |D_{11} - D_{22}|, \quad (2.35)$$

and between the states  $|\psi_\pm \rangle$  in the  $\{|v_1, -1 \rangle, |v_2, +1 \rangle\}$  subspace:

$$h\nu = eV_{g,\text{rf}} |\langle \psi'_+ | D | \psi'_- \rangle| = eV_{g,\text{rf}} |\alpha \beta| |D_{11} - D_{22}|, \quad (2.36)$$

where  $D_{11} = \langle v_1, \sigma | D | v_1, \sigma \rangle$  and  $D_{22} = \langle v_2, \sigma | D | v_2, \sigma \rangle$ . The Rabi frequency of this inner transition is, therefore, proportional to the mismatch between the matrix elements of the gate potential in valleys 1 and 2. The expansion of Eq. (2.34a) in powers of  $B$  and  $C_{21}$  yields back Eq. (2.24) at low magnetic fields. Yet Eqs. (2.34) are valid up to much larger field (typically  $g\mu_b B \lesssim E_3 - E_1$ , where  $E_3$  is the energy of the next-lying state).

### 2.8.3 Tight-binding results

We can validate the above model against tight-binding calculations. Tight-binding is well suited to the description of such devices as it takes into account valley- and spin-orbit coupling at the atomistic level, so without Rashba or Dresselhaus terms.

We consider a prototypical device with  $W = 30 \times H = 10$  nm, [110]-oriented silicon nanowire half-covered by a 30 nm long gate, similar to the one used in the experiment, but with only one gate for simplicity. As in real device, the gate is only partially covering the nanowire from one side.

We compute the first four eigenstates  $|\tilde{1} \rangle \dots |\tilde{4} \rangle$  of this device using a  $sp^3d^5s^*$  TB model. We include the effects of SO coupling and magnetic field. The former is described by an intra-atomic term  $H_{\text{SO}} = \lambda \mathbf{L}_i \cdot \mathbf{S}$  on each atom  $i$ , where  $\mathbf{L}_i$  is the angular momentum on atom  $i$ ,  $\mathbf{S}$  is the spin and  $\lambda$  is the SO coupling constant in silicon. The action of the magnetic field on the spin is described by the bare Zeeman Hamiltonian  $H_Z = g_0 \mu_b \mathbf{B} \cdot \mathbf{S}$ , and the action of the magnetic field on the orbital motion of the electrons is described by Peierl's substitution.

We can then monitor the different Rabi frequencies

$$\hbar\tilde{\nu}_{ij} = eV_{g,\text{rf}} |\langle \tilde{i} | D | \tilde{j} \rangle|. \quad (2.37)$$

Note that this TB description goes beyond the analytic model in including the action of the magnetic field on the orbital motion, and in dealing with all effects non-perturbatively.

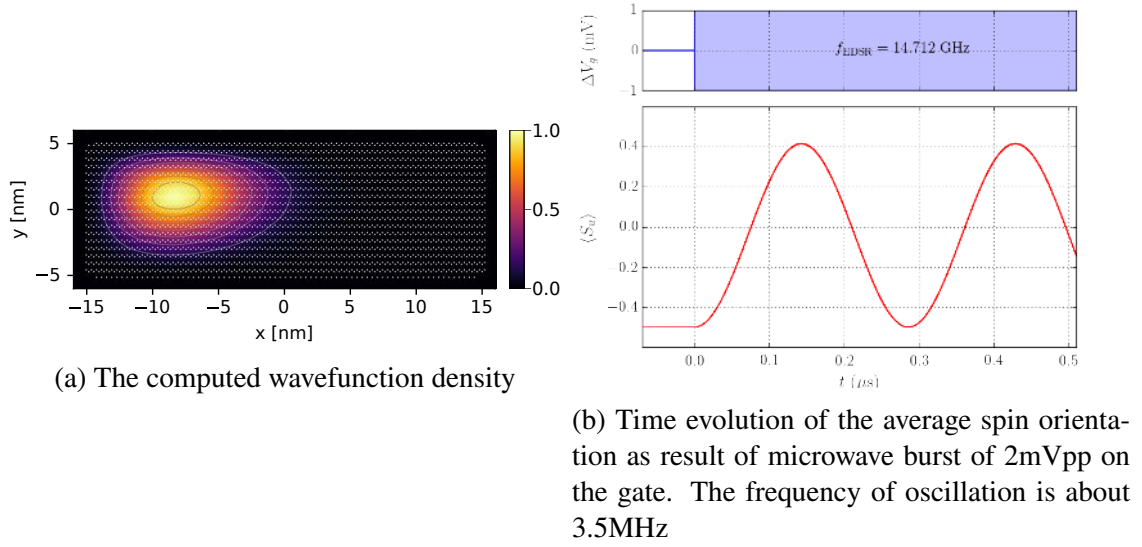


Figure 2.38 Results of tight-binding simulations

In figure 2.38 are reported the result of the the tight-biding simulation. In particular, in figure 2.38a is reported the cross-section of the calculated wavefunction density for this device. The dot sits in the upper corner of the nanowire. A simulated burst of microwave have been applied on the top gate with a frequency of about 14GHz with an peak-peak amplitude of 2mV (-50dBm). In figure 2.38b is reported this simulation and the time evolution of the average spin orientation. The frequency of oscillation is about 3.5MHz, in rough accordance with the experimental values of 5.9MHz for -35.5dBm (see section) 2.7.2).

$C_{21}$  may depend on the orientation of the external magnetic field. The Rabi frequency, and thus the leakage current can depends as well on the in-plane magnetic field orientation. Tight-binding simulation shows that the Rabi frequency has its maximum when the field is perpendicular to the nanowire, while it goes down to zero when the field gets parallel. This suggest that only terms proportional to  $\sigma_z$  in the spin-orbit Hamiltonian are relevant, like in a Rashba-like contribution. This is in good agreement with the experiment, as seen in figure 2.27.

## 2.9 Conclusions

We have shown the manipulation of spin for an electron confined in a quantum dot. We found a resonance signal with a g-factor around 2, compatible with the one for free electrons in bulk silicon. Intra and inter-valley has been measured, with a valley splitting of few tens of micro electron-volt. Transverse coherence time ( $T_2^*$ ) has been evaluated from low-power continuous-wave measurement to be around 40ns. Signatures of coherent manipulation, in form of Rabi oscillations have been measured, with a Rabi frequency of 6MHz. This manipulation, contrary to the initial aims of a magnetic drive field, is performed completely by electric field. We propose a theory to explain the origin of this coupling, with realistic tight-binding simulations.





## Chapter 3

# Reflectometry - Dual-channel gate dispersive readout

Integration of charge sensors for the readout of quantum bits (qubits) is one of the necessary ingredients for the realization of scalable semiconductor quantum computers [18]. In most qubits developed so far in silicon, like electron or nuclear spins in quantum dots and single atoms [2, 84, 99], charge [100] or hybrid spin-charge states [101], qubit readout has been performed with the aid of quantum point contacts (QPCs) or single-electron transistors (SETs). These charge-sensitive devices, however, involve a significant overhead in terms of gates and contact leads, posing an issue for scalability towards many-qubit architectures.

Gate-coupled radio-frequency (RF) reflectometry [102–104] has been recently proposed as an alternative approach to qubit readout. In this technique, the charge sensing required to sense the qubit state is accomplished by measuring the dispersive response of an electromagnetic RF resonator connected to one of the qubit gates and excited at its resonance frequency. The absence of local charge sensors simplifies the qubit physical layer [18] and allows for a tighter qubit pitch. Further, the RF resonator can be a microscopic circuit shared by many qubits through frequency multiplexing.

Before its first implementation in a gate-coupled geometry [102], RF reflectometry has been (and still is) applied to increase the readout bandwidth and sensitivity of electrometers such as QPCs, SETs or Cooper-pair transistors [105–108]. Also, it has been used to discern remote charge traps in the polysilicon gate stack [49] or in the channel [109] of silicon nanowire field-effect transistors (FETs).

Gate-coupled reflectometry has been shown [104] to achieve bandwidths and sensitivities comparable to those of on-chip charge detectors. Combined with spin-to-charge conversion processes [110], it has allowed detecting spin-related effects in double quantum dots (DQDs) [111–114]. In a recent experiment, gate reflectometry has also been used to reveal coherent

charge oscillations in a silicon DQD [115] and measure coherence times of the order of 100 ps, consistent with those found in an earlier study based on DC transport [116].

Here we apply gate reflectometry to investigate the electronic properties of a silicon DQD. Besides probing the full charge stability diagram at equilibrium (i.e. zero drain-source bias voltage  $V_{ds}$ ), we shall present reflectometry measurements at finite  $V_{ds}$ , where we will show that i) gate reflectometry allows probing excited quantum dot levels (even when the DC current is too small to be measured), and ii) the dispersive response of a resonator is strongly influenced by the conductive regime of the DQD and the associated charge relaxation rate. This chapter is an extract of our article “Level spectrum and charge relaxation in a silicon double quantum dot probed by dual-gate reflectometry”[117]

### 3.1 Device and measurement setup

Measurements are carried out on double-gate silicon nanowire FETs, similar to the one presented in section 2.1. Fig. 3.1a) shows a false colour scanning electron micrograph of a typical device. Transistors present a silicon channel thickness  $t_{\text{Si}} = 11$  nm and width  $W_{\text{Si}} = 15$  nm, whereas gates, denoted as  $G_1$  and  $G_2$ , are patterned with a length  $L_g = 35$  nm and a spacing  $S_{gg} = 35$  nm. At low temperature, the two gates are employed in accumulation mode to define two electron quantum dots in series.

DC charge transport measurements are performed by grounding the source electrode, S, and connecting the drain contact, D, to a transimpedance amplifier with adjustable reference potential. Two lumped-element resonators,  $R_1$  and  $R_2$ , are connected to  $G_1$  and  $G_2$ , respectively. Each resonator is composed of a surface-mount inductor (nominal inductances:  $L_1 = 270$  nH and  $L_2 = 390$  nH for  $R_1$  and  $R_2$ , respectively) and the parasitic capacitance  $C_p$  at the corresponding gate [102–104, 118] [see Fig. 3.1c)]. The resulting resonance frequencies are  $f_0^{(1)} = 421$  MHz and  $f_0^{(2)} = 335$  MHz, respectively. Unlike drain-based reflectometry, where the LC circuit provides impedance-matching conditions for the source-drain resistance of the charge sensor (SET or QPC), here the purpose of the inductor along with its parasitic capacitance is to provide a resonant network sensitive to small changes in the load capacitance (in this case the total capacitance seen by the gate). The dispersive responses of  $R_1$  and  $R_2$  are simultaneously recorded using homodyne detection on the reflected RF signals.

A circuit representation of the DQD system is shown in Fig. 3.1b). We label the quantum dot accumulated below  $G_1$  ( $G_2$ ) as “dot 1” (“dot 2”). The electrostatic influence of gate  $j$  on dot  $i$  ( $i, j = 1, 2$ ) is mediated by a capacitance  $C_{ij}$ . The DQD is electrically connected to the S and D reservoirs via tunnel barriers with characteristic tunnel rates  $\Gamma_L$  and  $\Gamma_R$ , respectively.

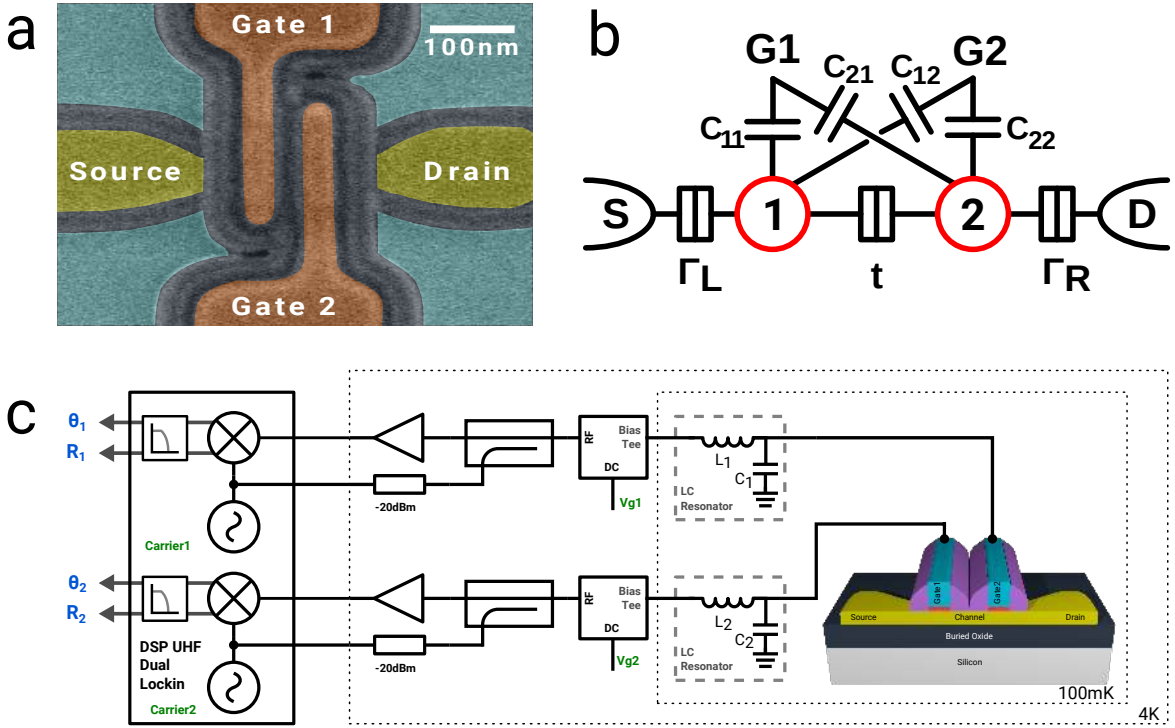


Figure 3.1 a) False color scanning electron micrograph of a typical double gate device nominally identical to the measured samples. Orange denotes the gate electrodes, whereas spacers are dark grey. Heavily-doped regions of reservoirs are highlighted in yellow. b) Schematic of the dual-port measurement setup. Each gate is connected to a resonator for dispersive readout. Demodulation is performed at room temperature by a Ultra High Frequency dual lock-in. c) Equivalent circuitry of the sensed quantum system. The two quantum dots are red circles. Labels and elements are explained in the main text.

We operate the device in a regime where  $k_B T_e \lesssim 2t < \Delta$ , with  $k_B$  is the Boltzmann constant,  $T_e$  the electron temperature ( $\sim 300$  mK),  $t$  the interdot tunnel coupling and  $\Delta$  the mean level spacing in each dot, typically in the range from  $\sim 0.1$  to few meV [119, 68].

Let's now define the formalism for an isolated DQD. No charges are given to or removed from the reservoirs but a single electron can be switched between the two dots, corresponding to an excess electron in either dot 1 or dot 2. Interdot dynamics between the localized states  $|1\rangle$  and  $|2\rangle$ , respectively of dot 1 and dot 2, is described by the Hamiltonian  $H = (\epsilon/2)\sigma_z + t\sigma_x$ :  $\epsilon$  is the detuning parameter, i.e. the misalignment between chemical potentials of the two dots in the limit of vanishing interdot coupling  $t$ , and  $\sigma_{z,x}$  are Pauli matrices. The eigenstates of such two-level system are

$$\begin{aligned} |\psi_-\rangle &= \sin(\theta/2)|1\rangle - \cos(\theta/2)|2\rangle \\ |\psi_+\rangle &= \cos(\theta/2)|1\rangle + \sin(\theta/2)|2\rangle, \end{aligned} \quad (3.1)$$

where  $\tan\theta = 2t/\epsilon$  and  $|\psi_-\rangle$ ,  $|\psi_+\rangle$  correspond to the bonding and antibonding molecular states expressed in terms of the localized states  $|1\rangle$  and  $|2\rangle$ . The two eigenvalues, basically the states of a charge qubit, are

$$E_{\pm} = \pm \sqrt{\epsilon^2 + (2t)^2}/2 \quad (3.2)$$

## 3.2 Dispersive readout signal

Resonator  $R_1$  ( $R_2$ ) is sensitive through  $G_1$  ( $G_2$ ) to changes in the quantum admittance of the DQD system [120]. More precisely, an electron tunneling between two dots or between a dot and a reservoir gives rise to a small capacitance  $C_{\text{diff}}^j$  seen by the resonator  $R_j$  in addition to the geometric capacitances of Fig. 3.1b). The differential capacitance of a dot coupled to gate  $j$  is

$$C_{\text{diff}}^j = -e\alpha_j \frac{\partial \langle \nu \rangle}{\partial V_{Gj}}. \quad (3.3)$$

$e$  is the electron charge,  $\alpha_j$  is the lever-arm to convert the gate voltage  $V_{Gj}$  into energy and  $\langle \nu \rangle$  is the average excess charge flowing through the dot.

If the charge dynamics is faster than the probing frequency  $f_0^{(j)}$  of resonator  $R_j$ , the reflected signal experiences a phase variation  $\delta\Theta_j \propto -C_{\text{diff}}^j$  [108], hence non zero in correspondence of the charge transitions.

For small excitations applied by gate  $j$  to dot  $i$ , i.e.  $\delta V_{Gj} \ll 2t/e\alpha_{ij}$ , the differential capaci-

tance for resonator  $R_j$  reads [115]

$$C_{\text{diff}}^j = \frac{\beta_j^2}{2} \left( \frac{dZ}{d\epsilon} \frac{\epsilon}{\sqrt{\epsilon^2 + (2t)^2}} + Z \frac{(2t)^2}{[\epsilon^2 + (2t)^2]^{3/2}} \right), \quad (3.4)$$

with  $Z = P_- - P_+$  the difference between the occupation probabilities of  $|\psi_- \rangle$  and  $|\psi_+ \rangle$ ;  $\beta_j \equiv -e(\alpha_{1j} - \alpha_{2j})$  is the detuning lever-arm factor for gate  $j$ . The first term of Eq. 3.4, called tunnel capacitance, counts for transitions whose occupation probabilities  $P_-$  and  $P_+$  depend on the detuning, whereas the second one, named quantum capacitance, is related to band curvature  $\partial^2 E_{\pm} / \partial \epsilon^2$  [108].

### 3.3 Results

Figure 3.2 contains a representative set of stability diagrams measured by gate reflectometry. Panels a) and b) display color maps of the phase responses  $\delta\Theta_1$  and  $\delta\Theta_2$  obtained from  $R_1$  and  $R_2$ , respectively. These two data sets have been simultaneously recorded for the same range of gate voltages  $V_{G1}$  and  $V_{G2}$  at  $V_{ds} = 0$ . Denoted the electron number in dot 1 and dot 2 as  $M$  and  $N$  respectively, dot-lead charge transitions  $(M, N) \leftrightarrow (M+1, N)$  ( $(M, N+1) \leftrightarrow (M, N)$ ) are detected primarily by resonator  $R1$  ( $R2$ ). Interdot transitions  $(M+1, N) \leftrightarrow (M, N+1)$  in principle could be equally sensed by both  $R1$  and  $R2$ ; in the case of Fig. 3.2, however, they happen to be clearly visible only in the  $\delta\Theta_2$  phase plot. Interdot lines can also be found in  $\delta\Theta_1$  signal in other regions of the stability diagram (not shown). Such behavior is probably related to the fact that the two quantum dots are not precisely positioned under the respective gates, and that their precise location changes with the electron filling of the channel region. Panel c) is simply the superposition of a) and b). It clearly shows that the two RF resonators together allow detecting all charge boundaries in the stability diagram.

Let us now focus on interdot charge transitions. Since  $\hbar f_0^{(j)} < 2t$  ( $\hbar$  is Planck's constant), interdot tunneling is adiabatic and  $C_{\text{diff}}$  is dominated by the quantum capacitance associated to  $|\psi_- \rangle$ , leading to a negative phase shift, i.e. a dip in the dispersive signal [114]. This result is expected at equilibrium, where the DQD lies in its ground state  $|\psi_- \rangle$ . Out of equilibrium, a non negligible probability of occupying the excited state  $|\psi_+ \rangle$ , which gives a positive phase shift, can qualitatively change the dispersive response. For instance, Ref. 115 reports a strongly driven two-level system (i.e.  $\hbar f > 2t$ ) in which non-adiabatic transitions between  $|\psi_- \rangle$  and  $|\psi_+ \rangle$  result in a Landau-Zener-Stückelberg interference pattern with both

negative and positive phase shifts in the reflected signal. Indeed Eq. 3.4 holds also for DQDs out of equilibrium as long as the resonators sense the stationary occupation probabilities of the DQD states. In the following, we investigate the out-of-equilibrium regime resulting from a finite  $V_{ds}$ . At positive detuning the excited state  $|\psi_+\rangle$  is populated in the process of charge tunneling from the source reservoir. Fig. 3.2d) shows the phase response on  $R_2$  in a conducting regime of the DQD at  $V_{ds}=5.75$  mV. The first thing we learn from this measurement is that, similarly to current transport, gate dispersive readout can detect excited-state transitions. These transitions, denoted by green arrows, form a set of lines running parallel to the base of the triangular regions, which corresponds to ground-state tunnel events [63]. Given the sign of the applied bias voltage, electrons flow from dot 1 to dot 2. As a result, the observed lines correspond to excited states of dot 2. On the other hand, the line denoted by a blue arrow, running parallel to the almost horizontal edge of the upper triangle is associated with an excitation in dot 1 occurring during tunneling from the source contact to dot 1. We remark that the demonstrated use of gate reflectometry as a tool for energy-level spectroscopy could be extrapolated to DQDs with extremely weak coupling to the source and drain reservoirs, where the more standard transport-based spectroscopy is hindered by unmeasurably small current levels.

Fig. 3.2d) bares a second important message. All inter-dot transitions display a clear peak-dip structure. This is revealed by a measurement of the phase response as a function of the detuning  $\epsilon$ , see the  $\delta\Theta_2(\epsilon)$  trace in the inset to Fig. 3.2d) corresponding to a line cut along the black solid line.

### 3.4 Modeling of out-of-equilibrium response

In order to understand the physical origin of the observed peak-dip structure, we initially derive a set of master equations for the occupation probabilities of the DQD states. At positive  $V_{ds}$ , electron transport involves cyclic transitions in the charge states of the DQD, notably  $(M+1, N) \rightarrow (M, N+1) \rightarrow (M, N) \rightarrow (M+1, N)$  for the lower triangular region of Fig. 3.3a), and  $((M+1, N) \rightarrow (M, N+1) \rightarrow (M+1, N+1) \rightarrow (M+1, N))$  for the upper one. For the sake of simplicity, let us consider only the first of these two options. These corresponding charge states can be mapped onto the “molecular” basis states  $\{|0\rangle, |\psi_-\rangle, |\psi_+\rangle\}$ , where  $|0\rangle$  refers to the  $(M, N)$  charge configuration. The rate equations for the correspond-

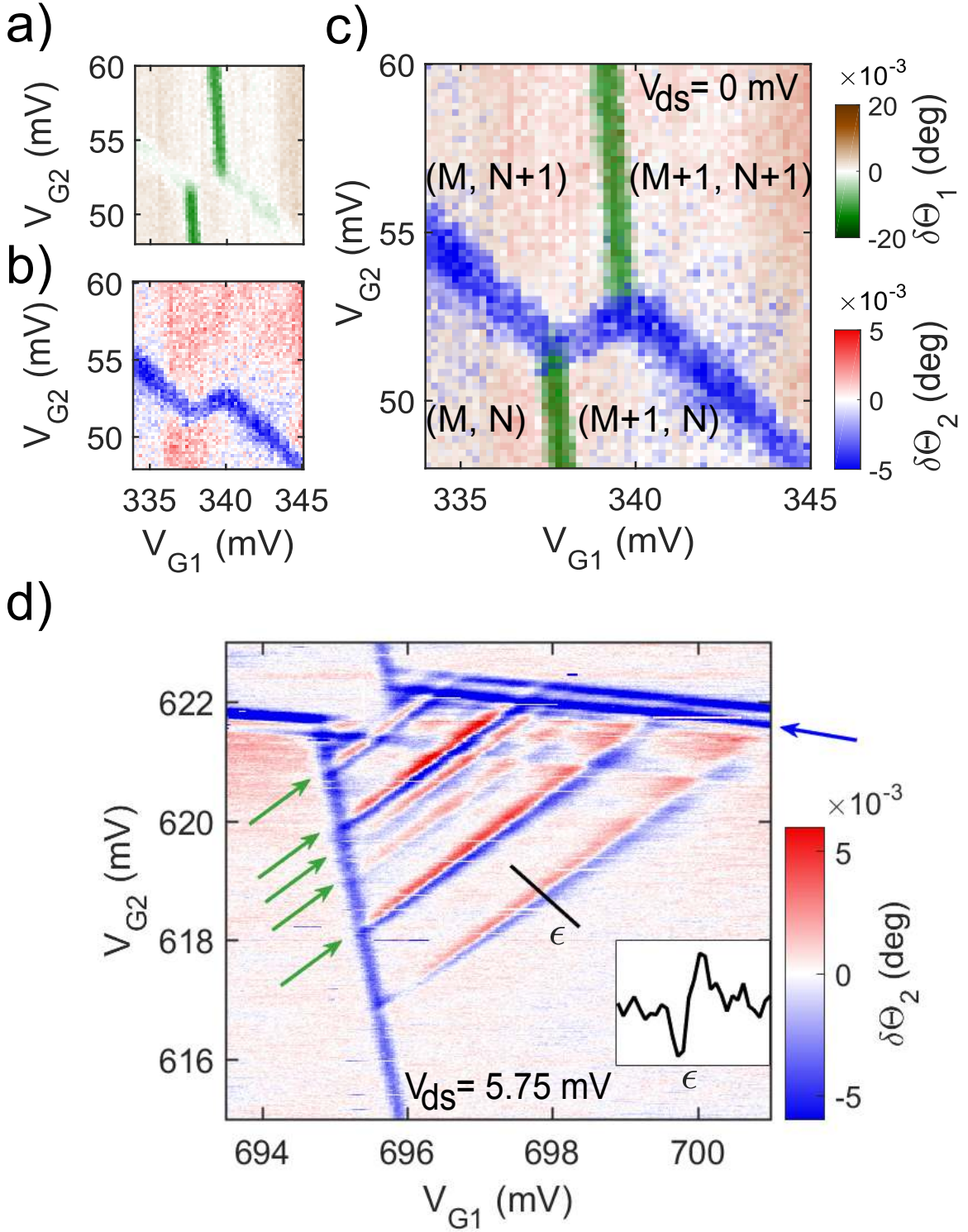


Figure 3.2 a), b), c) The triple point of a DQD stability diagram at nominal 0 bias results from the overlap of the plots a) and b) from detector  $R_1$  and  $R_2$  respectively. d) A different triple point measured at  $V_{ds} = 5.75$  mV. It exhibits the orbital spectrum of the DQD through lines parallel to the base of the triangles and lines parallel to the edges.

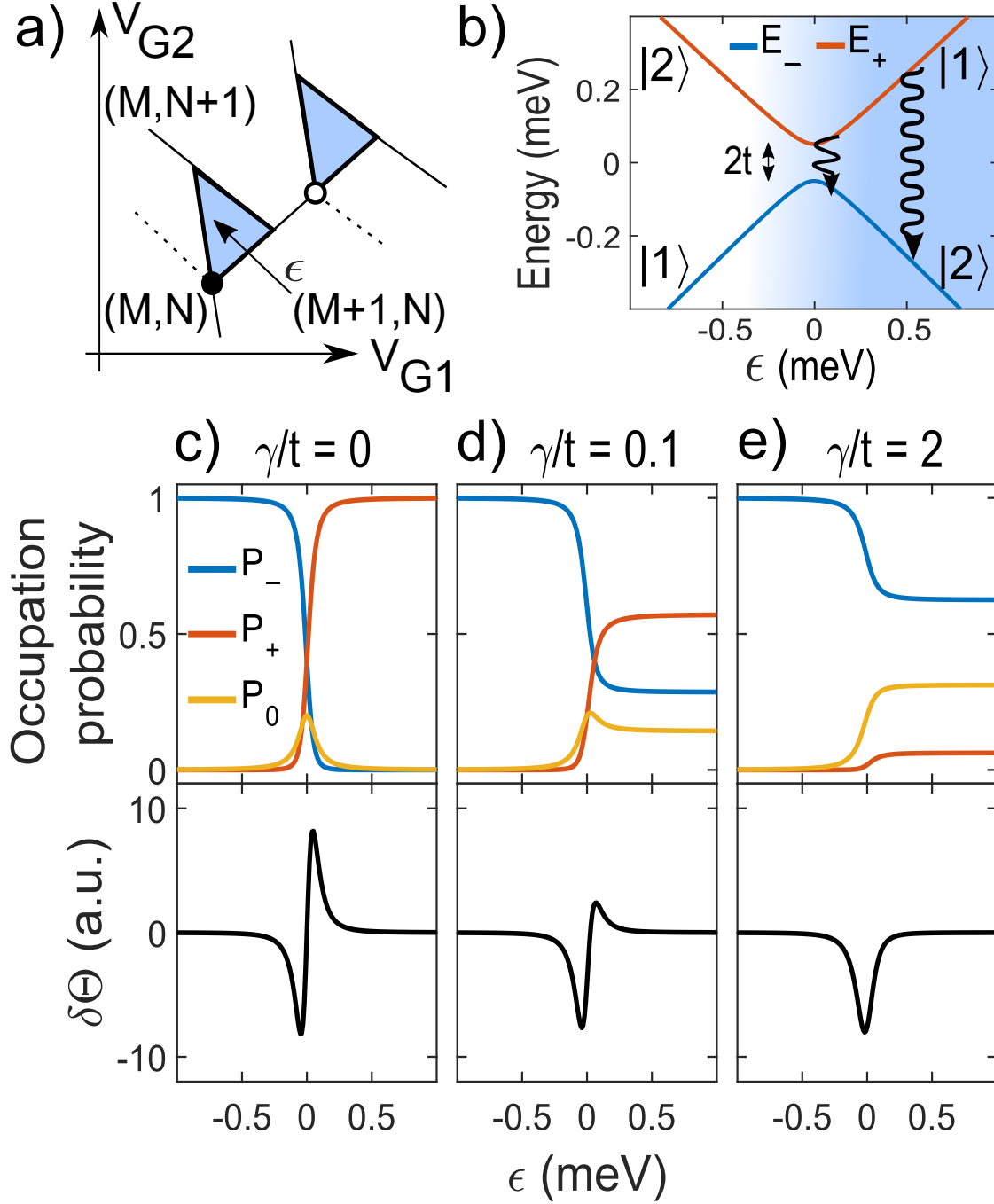


Figure 3.3 a) Schematic stability diagram at finite bias voltage. Numbers in the brackets denote the fixed-charge domains of the DQD; the light-blue triangular areas highlight the conductance regions. b) Ground and excited states of the DQD in presence of an extra charge. The light-blue background indicates the conductive condition. In the hybridization region  $|\epsilon| < 2t$  the  $E_{\pm}$  band curvature is maximized: resonators are sensitive to elastic and inelastic charge transfers. In the far detuned limit  $\epsilon > 2t$ ,  $|\psi_- \rangle$  and  $|\psi_+ \rangle$  are more localized, hence well approximated by single dot states  $|1\rangle$  and  $|2\rangle$ : inelastic transitions are weakly sensed due to the lack of band curvature. c), d), e) Occupation probabilities of the ground ( $P_-$ ), excited ( $P_+$ ) and empty ( $P_0$ ) configuration of the DQD from Eq. 3.5. The correspondent phase shift  $\delta\Theta$  is computed from Eq. 3.4. When there are no inelastic interdot transitions [ $\gamma/t = 0$ , panel c)], the dispersive response is a symmetrical dip-peak line shape. Such resonance gradually becomes asymmetric by setting some charge relaxations [ $\gamma/t = 0.1$ , panel d)], till it is just a dip for fast relaxations [ $\gamma/t = 2$ , panel e)]. In these plots  $\Gamma_R = 10 \mu\text{eV}$ ,  $\Gamma_L = 20 \mu\text{eV}$  and  $t = 50 \mu\text{eV}$ .



ing occupation probabilities are [121]:

$$\begin{aligned}\dot{P}_0 &= -\Gamma_L P_0 + \zeta \Gamma_R P_- + \Gamma_R (1 - \zeta) P_+ \\ \dot{P}_- &= \Gamma_L (1 - \zeta) P_0 - \zeta \Gamma_R P_- + \gamma P_+ \\ \dot{P}_+ &= \zeta \Gamma_L P_0 + [\Gamma_R (\zeta - 1) - \gamma] P_+\end{aligned}\tag{3.5}$$

with  $P_0 + P_- + P_+ = 1$ ,  $\zeta \equiv \cos^2(\theta/2)$  and,  $\gamma$  representing the inelastic interdot tunnel rate (in other words, the energy relaxation rate,  $T_1^{-1}$ , of the charge qubit with energy levels  $E_{\pm}$  [see Fig. 3.3b]). The stationary occupation probabilities  $P_0, P_-, P_+$  depend on the dot-lead rates  $\Gamma_L, \Gamma_R$  and the elastic and inelastic interdot rates, respectively  $t$  and  $\gamma$ . Once estimated  $P_+$  and  $P_-$  from Eq. 3.5, the resulting phase response  $\delta\Theta$  is computed by Eq. 3.4.

To perform the simulations of Figs. 3.3c), d) and e) we assume from the device symmetry the access barriers  $\Gamma_L, \Gamma_R$  differ from one other by one order of magnitude at maximum; in particular, we notice that  $\Gamma_L$  does not significantly influence the  $\delta\Theta$  lineshape, whereas  $\Gamma_R$  rules the height of the whole phase resonance. The excited state  $|\psi_+\rangle$  originates the peak side of the dip-peak structure when  $\Gamma_R > \gamma$ . Finally, the full width at half maximum (FWHM) of the dip is found to be  $\sim 2t$  when dip and peak are both present and  $\sim 2.5t$  for a dip-only resonance. Under these constraints, the asymmetry between the dip and peak amplitudes is set mostly by  $\gamma/t$ , as displayed in Figs. 3.3c), d) and e). In absence of energy relaxation ( $\gamma = 0$ , panel c)), charge transport makes  $|\psi_-\rangle$  mainly occupied for  $\epsilon < 0$  and  $|\psi_+\rangle$  mainly occupied for  $\epsilon > 0$ . Equal occupation probabilities are found for  $\epsilon = 0$ . Since  $E_-(\epsilon)$  and  $E_+(\epsilon)$  have exactly opposite curvatures, the dispersive response  $\delta\Theta(\epsilon)$  is characterized by a dip-peak structure with equally strong peak and dip components, as shown in the bottom panel of Fig. 3.3c). In presence of energy relaxation ( $\gamma > 0$ ), the average probability to be at energy  $E_+$  for positive detuning decreases, resulting in a reduced amplitude of the positive  $\delta\Theta$  component (see bottom panel of Fig. 3.3d)). Finally, for a strong energy relaxation rate ( $\gamma \gg t$ ), the DQD is predominantly in the  $|\psi_-\rangle$  state for any detuning, and the dispersive response exhibits only a dip in  $\delta\Theta$ , as shown in Fig. 3.3e).

In Fig. 3.4 we provide an experimental demonstration of the three regimes of Figs. 3.3c), d) and e). Panel a) shows a transport measurement with a pair of bias triangles in which the inelastic current is barely visible, indicating a slow relaxation rate. In the corresponding reflectometry signal, presented in panel b), the overlapping bases of the triangles appear with a pronounced dip-peak structure. A line cut along the dashed line, displayed in panel c), reveals that peak and dip have almost identical amplitudes, as expected for  $\gamma/t \ll 1$ . From the FWHM of the dip,  $t = 40 \mu\text{eV}$ . Given the assumptions above, the phase trace is fitted to Eq. 3.4 with fairly good agreement, yielding  $\gamma = 2 \pm 1 \mu\text{eV}$ , thus  $\gamma/t \approx 1/20$ .

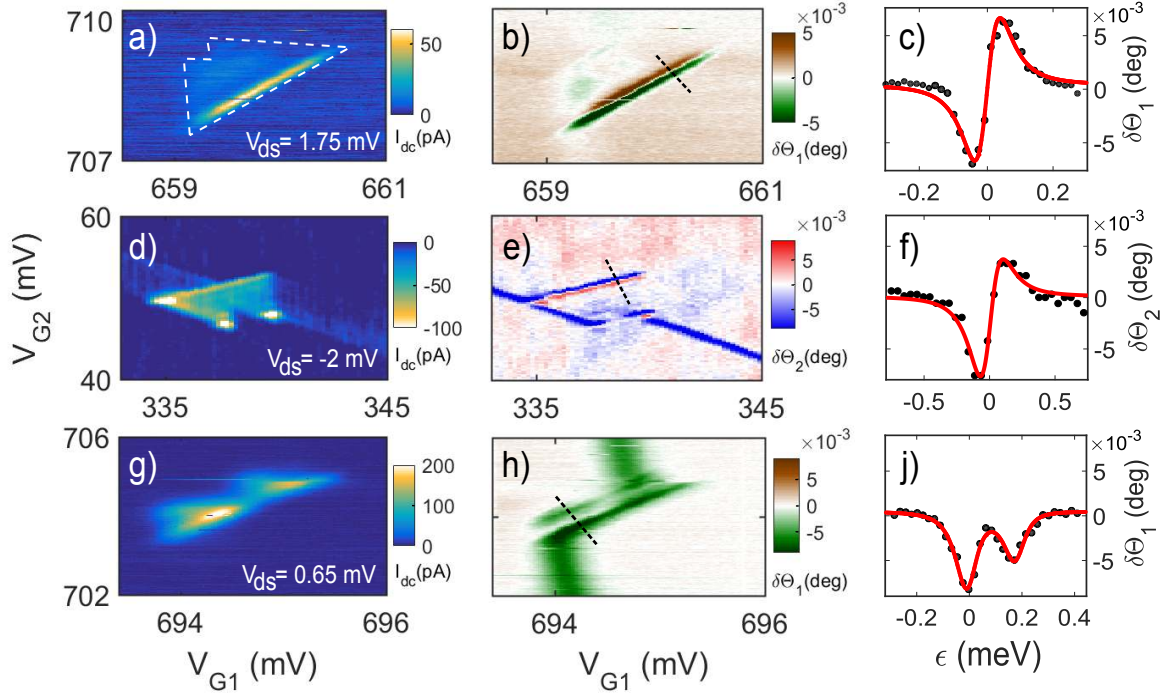


Figure 3.4 Stability diagrams of bias triangles recorded by source-drain current [panels a), d), f)] and dispersive signal [panels b), e), h)] relative to three different triple points characterized respectively by weak, medium and fast relaxation rate  $\gamma$ . Reflectometry data are plotted for the gate detector with better interdot signal. Black dashed lines indicate the detuning axis setting the energy scale on the plots for fitting on the right [(c), (f) and (j)]. Triple point edges in a) are marked by white dashed lines as a guide for the eyes.

The intermediate regime, where energy relaxation starts to be important, is observed on a different pair of bias triangles, where the inelastic current is small but clearly visible, as shown in panel d). A dip-peak structure is still visible in the corresponding reflectometry signal [see panel e) and line cut in panel d)], but the peak component is now weaker, as expected from a non negligible energy relaxation. For  $t = 90 \mu\text{eV}$ , the fit to Eq. 3.4 results again in a good agreement, yielding  $\gamma/t = 0.08 \pm 0.02$ .

The strong relaxation regime is observed on a third pair of bias triangles. The transport data in panel g) show a pronounced inelastic current. The (positive) peak component has completely disappeared from the phase response leaving only a dip structure. In fact, two dip structures are seen in panels h) and j). They correspond to different orbital levels of dot 2. Given  $t = 35 \mu\text{eV}$ , the fit gives  $\gamma/t = 3.0 \pm 0.3$ , consistent with the observation of strong energy relaxation.

## 3.5 Conclusions

In summary, we have studied silicon double quantum dots by means of a dual RF gate reflectometry setup. Two resonators operate in-parallel as independent charge transfer detectors. Such dispersive readout technique enables the mapping of DQD charge stability diagrams both at zero and finite bias voltage. For a net source-drain current across the DQD, the dispersive response is sensitive to charge relaxation between double-dot molecular states; by taking into account transport rate equations, we fit the reflected phase signal to extract the interdot tunnel coupling and the charge relaxation rate. Dispersive sensing of interdot dynamics can be implemented in time-dependently operated multi-gate devices with applications in metrology [122] and tunnel-coupled qubits, like chains of quantum dots or dopants.



# Conclusions

In conclusion, we investigated several key building blocks needed to realize a silicon Qubit on a Trigate SOI platform. We performed room-temperature measurement to evaluate the reliability and statistical properties of our MOSFET-like devices. We carried low-temperature experiments on selected samples to evaluate charge and spin confinement in quantum dots, spin manipulation and charge and spin readout. All these task have been successfully demonstrated, with different readiness level, thus proving the capabilities of our platform for electron spin Qubits.

In the manuscript we exposed measurements performed over samples with different sizes and geometries, exploring the different charge and spin confinement capabilities. In chapter 1 we explored the electron and hole confinement in ultrascaled MOSFET. The nanowires widths were as short as 3.4nm, with gates as short as 10nm. The confinement potential were very steep and localized, leading to enormous charging energy up to 230 meV. This enabled Single Electron Transistor operation up to room temperature. Confinement of both electron and holes (in different unipolar devices) was demonstrated. Single dot operation, with single-level electron transport mechanism has been shown. Compared to others works in this subject, we were able to follow the evolution of resonant tunneling peaks over the 4-300K range of temperature, demonstrating the presence of only one dot in the nanowire in all cases. Double dot operation with holes has been demonstrated as well, with the combined use of top and back gate [29].

Given the reduced dimension of the system, the confinement properties are dominated by surface roughness, leading to a large variability among nominally equivalent samples. However, the system can be tuned to the right SET thanks to the back gate.

By relaxing the geometrical dimensions, we where able to reach a better control and variability of our dots. It also enable us to explore new and more complicated geometries, thanks to use of more flexible e-beam lithography. Creation of double dots system has been proved reliable in the double-gate in series geometry (chapter 3) and in partially-overlapping double-gate geometry with side-gate (chapter 2). Moreover, in these structures we were able to confine and read the spin, thanks to the spin-blockade phenomenon. Barrier and dot tunability is

guaranteed by the back-gate and the eventual side-gate. The Trigate SOI has been proved to be a viable platform for silicon-based quantum devices. On-chip co-integration of classical FET-based and quantum devices is also possible and a great advantage of this technology [123, 124].

In chapter 2 we study how to manipulate to spin after the confinement in dots. Magnetic manipulation of spin with an RF antenna proved to be challenging; moreover it requires a large surface to place a proper coplanar waveguide. Instead we found a novel scheme for Electric Dipole Spin Resonance, which can be used with simpler gate structures. This new scheme exploits specific properties of silicon as material, such as valley degree of freedom. The specific trigate 3D geometry of the sample plays an important role in making this manipulation scheme possible. Fully-electrical spin manipulation is an important milestone, since it's usually performed with the help of dedicated external structures (like RF antenna or micromagnets) or with dedicated multiple-spin mechanism (like singlet/triplet, exchange only or hybrid qubit). We found a resonance signal with a  $g$ -factor around 2, compatible with the one for free electrons in bulk silicon. Intra and intervalley has been measured, with a valley splitting of few tens of micro electron-volt. Transverse coherence time ( $T_2^*$ ) has been evaluated from low-power continuous-wave measurement to be around 40ns. Signatures of coherent manipulation, in form of Rabi oscillations have been measured, with a Rabi frequency of 6MHz. More measurements are needed to confirm this result and to properly evaluate the performances of the obtained Qubit. It should be noted that the used geometry was not optimized for this kind of manipulation, hence the results can be improved by using new and more appropriate structures.

To read the spin state in chapter 2, we measured the current flow of the nanowire in the spin-blockade regime. This approach, albeit very simple, is extremely slow, since we are reading very small DC current (down to few hundreds of femto Amperes). Although this is good demonstrator for CW operations, it gets impracticable for real pulsed Qubit operation, since long pulse sequences and single-shot readout are impossible. Typically an external electrometer, such as an additional Single Electron Transistor or a Quantum Point Contact are used to readout the charge state. A spin-to-charge conversion mechanism is then used to probe the spin state. Instead of an additional charge sensor, we explored gate-coupled RF dispersive readout. Sensing is accomplished by reading the RF response of an LC resonator coupled to one gate. The signal is the variation of the gate capacitance, and in turn the quantum capacitance of the dot. In chapter 3 we employed this technique on both gates of a double-dot system. We probed all the charge transition around a triple point. When the drain is biased and there is transport, different lineshape appears. Thanks to a master equation model of the transport in the system, we were able to link this new features to the

---

charge dynamics and relaxation times in the double-dot. We also probed spin-blockade to seek for a possible charge-to-spin readout. Further development would seek for real-time readout for fast Qubit operations.





# Bibliography

- [1] N. Yoran and B. Reznik, “Deterministic Linear Optics Quantum Computation with Single Photon Qubits,” [Physical Review Letters](#) **91**, 037903 (2003).
- [2] J. J. Pla, K. Y. Tan, J. P. Dehollain, W. H. Lim, J. J. L. Morton, D. N. Jamieson, A. S. Dzurak, and A. Morello, “A single-atom electron spin qubit in silicon,” [Nature](#) **489**, 1 (2012).
- [3] B. E. Kane, “A silicon-based nuclear spin quantum computer,” [Nature](#) **393**, 133 (1998).
- [4] Y. Nakamura, Y. A. Pashkin, and J. S. Tsai, “Coherent control of macroscopic quantum states in a single-Cooper-pair box,” [Nature](#) **398**, 786 (1999).
- [5] J. R. Friedman, J. R. Friedman, V. Patel, V. Patel, W. Chen, W. Chen, S. Tolpygo, S. Tolpygo, J. E. Lukens, and J. E. Lukens, “Quantum superposition of distinct macroscopic states,” [Nature](#) **406**, 43 (2000).
- [6] J. I. Cirac and P. Zoller, “Quantum computations with cold trapped ions,” [Physical Review Letters](#) **74**, 4091 (1995).
- [7] L. M. Vandersypen, M. Steffen, G. Breyta, C. S. Yannoni, M. H. Sherwood, and I. L. Chuang, “Experimental realization of Shor’s quantum factoring algorithm using nuclear magnetic resonance,” [Nature](#) **414**, 883 (2001).
- [8] H. Mooij, “Superconducting quantum bits,” [Physics World](#) **17**, 29 (2004).
- [9] M. H. Devoret and R. J. Schoelkopf, “Superconducting circuits for quantum information: an outlook,” [Science \(New York, N.Y.\)](#) **339**, 1169 (2013).
- [10] L. DiCarlo, J. M. Chow, J. M. Gambetta, L. S. Bishop, B. R. Johnson, D. I. Schuster, J. Majer, A. Blais, L. Frunzio, S. M. Girvin, and R. J. Schoelkopf, “Demonstration of two-qubit algorithms with a superconducting quantum processor,” [Nature](#) **460**, 240 (2009).
- [11] R. Barends, J. Kelly, A. Megrant, A. Veitia, D. Sank, E. Jeffrey, T. C. White, J. Mutus, A. G. Fowler, B. Campbell, Y. Chen, Z. Chen, B. Chiaro, A. Dunsworth, C. Neill, P. O’Malley, P. Roushan, A. Vainsencher, J. Wenner, a. N. Korotkov, a. N. Cleland, and J. M. Martinis, “Superconducting quantum circuits at the surface code threshold for fault tolerance,” [Nature](#) **508**, 500 (2014).

- [12] J. R. Petta, A. C. Johnson, J. M. Taylor, E. A. Laird, A. Yacoby, M. D. Lukin, C. M. Marcus, M. P. Hanson, and A. C. Gossard, "Coherent manipulation of coupled electron spins in semiconductor quantum dots," [\*Science \(New York, N.Y.\)\* \*\*309\*\*, 2180 \(2005\)](#).
- [13] F. H. L. Koppens, C. Buizert, K. J. Tielrooij, I. T. Vink, K. C. Nowack, T. Meunier, L. P. Kouwenhoven, and L. M. K. Vandersypen, "Driven coherent oscillations of a single electron spin in a quantum dot," [\*Nature\* \*\*442\*\*, 766 \(2006\)](#).
- [14] R. Hanson, L. P. Kouwenhoven, J. R. Petta, S. Tarucha, and L. M. K. Vandersypen, "Spins in few-electron quantum dots," [\*Reviews of Modern Physics\* \*\*79\*\*, 1217 \(2007\)](#).
- [15] M. Ciorga, A. Sachrajda, P. Hawrylak, C. Gould, P. Zawadzki, S. Jullian, Y. Feng, and Z. Wasilewski, "Addition spectrum of a lateral dot from Coulomb and spin-blockade spectroscopy," [\*Physical Review B\* \*\*61\*\*, R16315 \(2000\)](#).
- [16] K. Saeedi, S. Simmons, J. Z. Salvail, P. Dluhy, H. Riemann, N. V. Abrosimov, P. Becker, H.-J. Pohl, J. J. L. Morton, and M. L. W. Thewalt, "Room-Temperature Quantum Bit Storage Exceeding 39 Minutes Using Ionized Donors in Silicon-28," [\*Science\* \*\*342\*\*, 830 \(2013\)](#).
- [17] R. Maurand, X. Jehl, D. Kotekar-Patil, A. Corna, H. Bohuslavskyi, R. Laviéville, L. Hutin, S. Barraud, M. Vinet, M. Sanquer, and S. De Franceschi, "A CMOS silicon spin qubit," [\*Nature Communications\* \*\*7\*\*, 13575 \(2016\)](#).
- [18] D. J. Reilly, "Engineering the quantum-classical interface of solid-state qubits," [\*npj Quantum Information\* \*\*1\*\*, 15011 \(2015\)](#).
- [19] S. Barraud, R. Coquand, M. Casse, M. Koyama, J. M. Hartmann, V. Maffini-Alvaro, C. Comboroure, C. Vizioz, F. Aussenac, O. Faynot, and T. Poiroux, "Performance of omega-shaped-gate silicon nanowire MOSFET with diameter down to 8 nm," [\*IEEE Electron Device Letters\* \*\*33\*\*, 1526 \(2012\)](#).
- [20] F. A. Zwanenburg, A. S. Dzurak, A. Morello, M. Y. Simmons, L. C. L. Hollenberg, G. Klimeck, S. Rogge, S. N. Coppersmith, and M. A. Eriksson, "Silicon quantum electronics," [\*Reviews of Modern Physics\* \*\*85\*\*, 961 \(2013\)](#).
- [21] B. Voisin, R. Maurand, S. Barraud, M. Vinet, X. Jehl, M. Sanquer, J. Renard, and S. De Franceschi, "Electrical Control of g -Factor in a Few-Hole Silicon Nanowire MOSFET," [\*Nano Letters\* \*\*16\*\*, 88 \(2016\)](#).
- [22] R. Li, F. E. Hudson, A. S. Dzurak, and A. R. Hamilton, "Pauli Spin Blockade of Heavy Holes in a Silicon Double Quantum Dot," [\*Nano Letters\* \*\*15\*\*, 7314 \(2015\)](#).
- [23] F. Q. Xie, L. Nittler, C. Obermair, and T. Schimmel, "Gate-controlled atomic quantum switch," [\*Physical Review Letters\* \*\*93\*\*, 128303 \(2004\)](#).
- [24] E. Scheer, N. Agraït, J. C. Cuevas, A. L. Yeyati, B. Ludoph, A. Martín-Rodero, G. R. Bollinger, J. M. van Ruitenbeek, and C. Urbina, "The signature of chemical valence in the electrical conduction through a single-atom contact," [\*Nature\* \*\*394\*\*, 154 \(1998\)](#).

- [25] J. Park, A. N. Pasupathy, J. I. Goldsmith, C. Chang, Y. Yaish, J. R. Petta, M. Rinkoski, J. P. Sethna, H. D. Abruña, P. L. McEuen, and D. C. Ralph, "Coulomb blockade and the Kondo effect in single-atom transistors," *Nature* **417**, 722 (2002).
- [26] L. E. Calvet, R. G. Wheeler, and M. A. Reed, "Observation of the linear stark effect in a single acceptor in Si," *Physical Review Letters* **98**, 096805 (2007).
- [27] M. Fuechsle, J. A. Miwa, S. Mahapatra, H. Ryu, S. Lee, O. Warschkow, L. C. L. Hollenberg, G. Klimeck, and M. Y. Simmons, "A single-atom transistor," *Nature nanotechnology* **7**, 242 (2012).
- [28] M. Pierre, R. Wacquez, X. Jehl, M. Sanquer, M. Vinet, and O. Cueto, "Single-donor ionization energies in a nanoscale CMOS channel," *Nature nanotechnology* **5**, 133 (2010).
- [29] R. Lavieville, F. Triozon, S. Barraud, A. Corna, X. Jehl, M. Sanquer, J. Li, A. Abisset, I. Duchemin, and Y. M. Niquet, "Quantum dot made in metal oxide silicon-nanowire field effect transistor working at room temperature," *Nano Letters* **15**, 2958 (2015).
- [30] S. J. Shin, C. S. Jung, B. J. Park, T. K. Yoon, J. J. Lee, S. J. Kim, J. B. Choi, Y. Takahashi, and D. G. Hasko, "Si-based ultrasmall multiswitching single-electron transistor operating at room-temperature," *Applied Physics Letters* **97** (2010), 10.1063/1.3483618.
- [31] Z. Zhong, Y. Fang, W. Lu, and C. M. Lieber, "Coherent single charge transport in molecular-scale silicon nanowires," *Nano Letters* **5**, 1143 (2005).
- [32] F. A. Zwanenburg, C. E. W. M. Van Rijmenam, Y. Fang, C. M. Lieber, and L. P. Kouwenhoven, "Spin states of the first four holes in a silicon nanowire quantum dot," *Nano Letters* **9**, 1071 (2009).
- [33] M. Mongillo, P. Spathis, G. Katsaros, P. Gentile, M. Sanquer, and S. De Franceschi, "Joule-assisted silicidation for short-channel silicon nanowire devices," *ACS Nano* **5**, 7117 (2011).
- [34] F. Boeuf, X. Jehl, M. Sanquer, and T. Skotnicki, "Controlled single-electron effects in nonoverlapped ultra-short silicon field effect transistors," *IEEE Transactions On Nanotechnology* **2**, 144 (2003).
- [35] M. Hofheinz, X. Jehl, M. Sanquer, G. Molas, M. Vinet, and S. Deleonibus, "Simple and controlled single electron transistor based on doping modulation in silicon nanowires," *Appl. Phys. Lett.* **89**, 143504 (2006).
- [36] V. A. Krupenin, A. B. Zorin, M. N. Savvateev, D. E. Presnov, and J. Niemeyer, "Single-electron transistor with metallic microstrips instead of tunnel junctions," *Journal of Applied Physics* **90**, 2411 (2001).
- [37] K. Matveev and L. Glazman, "Coulomb blockade of activated conduction," *Physical Review B* **54**, 10339 (1996).
- [38] Y. Nazarov, "Coulomb Blockade without Tunnel Junctions," *Physical Review Letters* **82**, 1245 (1999).

- [39] G. Vasseur, D. Weinmann, and R. A. Jalabert, "Coulomb blockade without potential barriers," [The European Physical Journal B](#) **51**, 267 (2006).
- [40] Y. Takahashi, H. Nagase, H. Namatsu, K. Kurihara, K. Iwdate, Y. Nakajima, S. Horiguchi, K. Murase, and M. Tabe, "Fabrication technique for Si single-electron transistor operating at room temperature," [Electronics Letters](#) **31**, 136 (1995).
- [41] M. Saitoh and T. Hiramoto, "Extension of Coulomb blockade region by quantum confinement in the ultrasmall silicon dot in a single-hole transistor at room temperature," [Applied Physics Letters](#) **84**, 3172 (2004).
- [42] L. Zhuang, L. Guo, and S. Y. Chou, "Silicon single-electron quantum-dot transistor switch operating at room temperature," [Applied Physics Letters](#) **72**, 1205 (1998).
- [43] H. Ishikuro and T. Hiramoto, "Quantum mechanical effects in the silicon quantum dot in a single-electron transistor," [Applied Physics Letters](#) **71**, 3691 (1997).
- [44] V. Deshpande, R. Wacquez, M. Vinet, X. Jehl, S. Barraud, R. Coquand, B. Roche, B. Voisin, C. Vizioz, B. Previtali, L. Tosti, P. Perreau, T. Poiroux, M. Sanquer, B. De Salvo, and O. Faynot, "300 K operating full-CMOS integrated Single Electron Transistor (SET)-FET circuits," in [Electron Devices Meeting \(IEDM\), 2012 IEEE International](#) (2012) pp. 8.7.1–8.7.4.
- [45] Y. Sun, Rusli, and N. Singh, "Room-temperature operation of silicon single-electron transistor fabricated using optical lithography," [IEEE Transactions on Nanotechnology](#) **10**, 96 (2011).
- [46] V. N. Golovach, X. Jehl, M. Houzet, M. Pierre, B. Roche, M. Sanquer, and L. I. Glazman, "Single-dopant resonance in a single-electron transistor," [Physical Review B](#) **83**, 075401 (2011).
- [47] E. Bonet, M. M. Deshmukh, and D. C. Ralph, "Solving rate equations for electron tunneling via discrete quantum states," [Physical Review B](#) **65**, 045317 (2002).
- [48] S. J. Shin, J. J. Lee, H. J. Kang, J. B. Choi, S. R. E. Yang, Y. Takahashi, and D. G. Hasko, "Room-temperature charge stability modulated by quantum effects in a nanoscale silicon island," [Nano Letters](#) **11**, 1591 (2011).
- [49] B. J. Villis, A. O. Orlov, X. Jehl, G. L. Snider, P. Fay, and M. Sanquer, "Defect detection in nano-scale transistors based on radio-frequency reflectometry," [Applied Physics Letters](#) **99**, 152106 (2011).
- [50] D. Culcer, Ł. Cywiński, Q. Li, X. Hu, and S. Das Sarma, "Quantum dot spin qubits in silicon: Multivalley physics," [Physical Review B](#) **82** (2010), 10.1103/PhysRevB.82.155312.
- [51] M. Pierre, R. Wacquez, B. Roche, X. Jehl, M. Sanquer, M. Vinet, E. Prati, M. Belli, and M. Fanciulli, "Compact silicon double and triple dots realized with only two gates," [Applied Physics Letters](#) **95**, 242107 (2009).

- [52] H. Bohuslavskyi, D. Kotekar-Patil, R. Maurand, A. Corna, S. Barraud, L. Bourdet, L. Hutin, Y.-M. Niquet, X. Jehl, S. De Franceschi, M. Vinet, and M. Sanquer, "Pauli Blockade in a Few-Hole PMOS Double Quantum Dot dominated by Spin-Orbit Interaction," *Applied Physics Letters* **109**, 193101 (2016).
- [53] J. P. Dehollain, J. J. Pla, E. Siew, K. Y. Tan, a. S. Dzurak, and A. Morello, "Nanoscale broadband transmission lines for spin qubit control," *Nanotechnology* **24**, 015202 (2013).
- [54] B. Sacépé, C. Chapelier, T. I. Baturina, V. M. Vinokur, M. R. Baklanov, and M. Sanquer, "Disorder-induced inhomogeneities of the superconducting state close to the superconductor-insulator transition," *Physical Review Letters* **101**, 1 (2008).
- [55] P. Diener, S. J. C. Yates, Y. J. Y. Lankwarden, J. J. A. Baselmans, and H. G. Leduc, "Design and testing of kinetic inductance detectors made of titanium nitride," *Journal of Low Temperature Physics* **167**, 305 (2012).
- [56] M. Tinkham, Introduction to superconductivity, 2nd ed. (Dover Publications, 1996) p. 454.
- [57] D. Hazra, N. Tsavdaris, S. Jebari, A. Grimm, F. Blanchet, F. Mercier, E. Blanquet, C. Chapelier, and M. Hofheinz, "Superconducting properties of very high quality NbN thin films grown by high temperature chemical vapor deposition," *Superconductor Science and Technology* **29**, 2 (2016).
- [58] "Sonnet Simulation Software," .
- [59] G. D. Fuchs, V. V. Dobrovitski, D. M. Toyli, F. J. Heremans, and D. D. Awschalom, "Gigahertz dynamics of a strongly driven single quantum spin." *Science (New York, N.Y.)* **326**, 1520 (2009).
- [60] Simon M. Sze and K. K. Ng, Physics of Semiconductor Devices, 3rd ed. (Wiley-Blackwell, 2006).
- [61] A. Ortiz-Conde, F. J. García Sánchez, J. J. Liou, A. Cerdeira, M. Estrada, and Y. Yue, "A review of recent MOSFET threshold voltage extraction methods," *Microelectronics Reliability* **42**, 583 (2002).
- [62] A. Ortiz-Conde, F. J. García-Sánchez, J. Muci, A. Terán Barrios, J. J. Liou, and C. S. Ho, "Revisiting MOSFET threshold voltage extraction methods," *Microelectronics Reliability* **53**, 90 (2013).
- [63] W. G. Van Der Wiel, S. De Franceschi, J. M. Elzerman, T. Fujisawa, S. Tarucha, and L. P. Kouwenhoven, "Electron transport through double quantum dots," *Reviews of Modern Physics* **75**, 1 (2003).
- [64] T. Kobayashi, J. Van Der Heijden, M. G. House, S. J. Hile, P. Asshoff, M. F. Gonzalez-Zalba, M. Vinet, M. Y. Simmons, and S. Rogge, "Resonant tunneling spectroscopy of valley eigenstates on a donor-quantum dot coupled system," *Applied Physics Letters* **108** (2016), 10.1063/1.4945736.

- [65] C. H. Yang, A. Rossi, R. Ruskov, N. S. Lai, F. A. Mohiyaddin, S. Lee, C. Tahan, G. Klimeck, A. Morello, and A. S. Dzurak, "Spin-valley lifetimes in a silicon quantum dot with tunable valley splitting," [Nature Communications](#) **4**, 2069 (2013).
- [66] A. S. D. N. S. Lai , W. H. Lim , C. H. Yang , F. A. Zwanenburg , W. A. Coish , F. Qassemi , A. Morello, "Pauli Spin Blockade in a Highly Tunable Silicon Double Quantum Dot," [Scientific Reports](#) **1**, 1217 (2011).
- [67] X. Hao, R. Ruskov, M. Xiao, C. Tahan, and H. Jiang, "Electron spin resonance and spin–valley physics in a silicon double quantum dot," [Nature Communications](#) **5**, 3860 (2014).
- [68] D. Kotekar-Patil, A. Corna, R. Maurand, A. Crippa, A. Orlov, S. Barraud, X. Jehl, S. De Franceschi, and M. Sanquer, "Pauli spin blockade in CMOS double quantum dot devices," [physica status solidi \(b\)](#) **254**, 1600581 (2017).
- [69] A. C. Johnson, J. R. Petta, C. M. Marcus, M. P. Hanson, and A. C. Gossard, "Singlet-triplet spin blockade and charge sensing in a few-electron double quantum dot," [Physical Review B - Condensed Matter and Materials Physics](#) **72**, 1 (2005).
- [70] A. Zarassi, Z. Su, J. Danon, J. Schwenderling, M. Hocevar, B. M. Nguyen, J. Yoo, S. A. Dayeh, and S. M. Frolov, "Magnetic field evolution of spin blockade in Ge/Si nanowire double quantum dots," [Physical Review B](#) **95**, 155416 (2017).
- [71] A. W. Overhauser, "Polarization of nuclei in metals," [Physical Review](#) **92**, 411 (1953).
- [72] F. H. L. Koppens, J. a. Folk, J. M. Elzerman, R. Hanson, L. H. W. van Beveren, I. T. Vink, H. P. Tranitz, W. Wegscheider, L. P. Kouwenhoven, L. M. K. Vandersypen, and E. Design, "Control and detection of singlet-triplet mixing in a random nuclear field." [Science \(New York, N.Y.\)](#) **309**, 1346 (2005).
- [73] L. Assali, H. Petrilli, R. Capaz, B. Koiller, X. Hu, and S. Das Sarma, "Hyperfine interactions in silicon quantum dots," [Physical Review B](#) **83**, 1 (2011).
- [74] W. A. Coish and F. Qassemi, "Leakage-current line shapes from inelastic cotunneling in the Pauli spin blockade regime," [Physical Review B](#) **84**, 245407 (2011).
- [75] G. Dresselhaus, "Spin-Orbit Coupling Effects in Zinc Blende Structures," [Phys.Rev.](#) **100**, 580 (1955).
- [76] E. I. Rashba, "Properties of semiconductors with a loop of extrema, I. Cyclotron and combined resonances in a perpendicular field," *Sov. Phys. Solid State* , 1109 (1960).
- [77] J. Danon and Y. V. Nazarov, "Pauli spin blockade in the presence of strong spin-orbit coupling," [Physical Review B - Condensed Matter and Materials Physics](#) **80**, 1 (2009).
- [78] K. C. Nowack, F. H. L. Koppens, Y. V. Nazarov, and L. M. K. Vandersypen, "Coherent control of a single electron spin with electric fields." [Science \(New York, N.Y.\)](#) **318**, 1430 (2007).
- [79] C.P.Slichter, *Principles of Magnetic Resonance*, 3rd ed. (Springer-Verlag, 1989).



- [80] A. Abragam, *Principles of Nuclear Magnetism* (Oxford University Press, 1961).
- [81] G. Feher, "Electron Spin Resonance Experiments on Donors in Silicon. I. Electronic Structure of Donors by the Electron Nuclear Double Resonance Technique," *Physical Review* **114**, 1219 (1959).
- [82] D. K. Wilson and G. Feher, "Electron Spin Resonance Experiments on Donors in Silicon. III. Investigation of Excited States by the Application of Uniaxial Stress and Their Importance in Relaxation Processes," *Physical Review* **124**, 1068 (1961).
- [83] F. Qassemi, W. A. Coish, and F. K. Wilhelm, "Stationary and Transient Leakage Current in the Pauli Spin Blockade," *Physical Review Letters* **102**, 176806 (2009).
- [84] E. Kawakami, P. Scarlino, D. R. Ward, F. R. Braakman, D. E. Savage, M. G. Lagally, M. Friesen, S. N. Coppersmith, M. A. Eriksson, and L. M. K. Vandersypen, "Electrical control of a long-lived spin qubit in a Si/SiGe quantum dot," *Nature nanotechnology* **9**, 666 (2014).
- [85] C. P. Poole, *Electron Spin Resonance: A Comprehensive Treatise on Experimental Techniques*, 2nd ed. (Wiley-Interscience, 1982).
- [86] E. H. Poindexter, P. J. Caplan, B. E. Deal, and R. R. Razouk, "Interface states and electron spin resonance centers in thermally oxidized (111) and (100) silicon wafers," *Journal of Applied Physics* **52**, 879 (1981).
- [87] M. Wattenbach and H. Alexander, "EDSR Investigation of n-type silicon deformed under high stress," *Physica Status Solidi (a)* **138**, 607 (1993).
- [88] M. P. Nowak, B. Szafran, and F. M. Peeters, "Resonant harmonic generation and collective spin rotations in electrically driven quantum dots," *Physical Review B* **86**, 125428 (2012).
- [89] M. Pioro-Ladrière, T. Obata, Y. Tokura, Y.-S. Shin, T. Kubo, K. Yoshida, T. Taniyama, and S. Tarucha, "Electrically driven single-electron spin resonance in a slanting Zeeman field," *Nature Physics* **4**, 776 (2008).
- [90] P. Scarlino, E. Kawakami, D. R. Ward, D. E. Savage, M. G. Lagally, M. Friesen, S. N. Coppersmith, M. A. Eriksson, and L. M. K. Vandersypen, "Second-Harmonic Coherent Driving of a Spin Qubit in a Si/SiGe Quantum Dot," *Physical Review Letters* **115**, 106802 (2015).
- [91] A. Dahal, J. Gunasekera, L. Harringer, D. K. Singh, and D. J. Singh, "Metallic Nickel Silicides : Experiments and Theory for NiSi and First Principles Calculations for Other Phases," *Journal of Alloys and Compounds* **672**, 110 (2016).
- [92] D. Connétable and O. Thomas, "First-principles study of the structural, electronic, vibrational, and elastic properties of orthorhombic NiSi," *Physical Review B* **79**, 094101 (2009).
- [93] D. Mangelinck, J. Y. Dai, J. S. Pan, and S. K. Lahiri, "Enhancement of thermal stability of NiSi films on (100)Si and (111)Si by Pt addition," *Applied Physics Letters* **75**, 1736 (1999).

- [94] M. Venkatesan, C. B. Fitzgerald, and J. M. D. Coey, "Thin films: unexpected magnetism in a dielectric oxide," *Nature* **430**, 630 (2004).
- [95] K. K. Bharathi, S. Venkatesh, G. Prathiba, N. H. Kumar, and C. V. Ramana, "Room temperature ferromagnetism in HfO<sub>2</sub> films," *Journal of Applied Physics* **109**, 07C318 (2011).
- [96] O. E. Tereshchenko, V. A. Golyashov, S. V. Eremeev, I. Maurin, A. V. Bakulin, S. E. Kulkova, M. S. Aksenov, V. V. Preobrazhenskii, M. A. Putyato, B. R. Semyagin, D. V. Dmitriev, A. I. Toropov, A. K. Gutakovskii, S. E. Khandarkhaeva, I. P. Prosvirin, A. V. Kalinkin, V. I. Bukhtiyarov, and A. V. Latyshev, "Ferromagnetic HfO<sub>2</sub>/Si/GaAs interface for spin-polarimetry applications," *Applied Physics Letters* **107**, 123506 (2015).
- [97] D. W. Abraham, M. M. Frank, and S. Guha, "Absence of magnetism in hafnium oxide films," *Applied Physics Letters* **87**, 1 (2005).
- [98] U. Devin, "Coherent Oscillations in Silicon Double Quantum Dots due to Meissner-screened Magnetic Field Gradients," *Bulletin of the American Physical Society* (2017).
- [99] J. J. Pla, K. Y. Tan, J. P. Dehollain, W. H. Lim, J. J. L. Morton, F. A. Zwanenburg, D. N. Jamieson, A. S. Dzurak, and A. Morello, "High-fidelity readout and control of a nuclear spin qubit in silicon," *Nature* **496**, 334 (2013).
- [100] Z. Shi, C. B. Simmons, D. R. Ward, J. R. Prance, R. T. Mohr, T. S. Koh, J. K. Gamble, X. Wu, D. E. Savage, M. G. Lagally, M. Friesen, S. N. Coppersmith, and M. A. Eriksson, "Coherent quantum oscillations and echo measurements of a Si charge qubit," *Physical Review B - Condensed Matter and Materials Physics* **88**, 75416 (2013).
- [101] D. Kim, Z. Shi, C. B. Simmons, D. R. Ward, J. R. Prance, T. S. Koh, J. K. Gamble, D. E. Savage, M. G. Lagally, M. Friesen, S. N. Coppersmith, and M. a. Eriksson, "Quantum control and process tomography of a semiconductor quantum dot hybrid qubit," *Nature* **511**, 70 (2014).
- [102] C. Ciccarelli and A. J. Ferguson, "Impedance of the single-electron transistor at radio-frequencies," *New Journal of Physics* **13**, 093015 (2011).
- [103] J. I. Colless, A. C. Mahoney, J. M. Hornibrook, A. C. Doherty, H. Lu, A. C. Gossard, and D. J. Reilly, "Dispersive Readout of a Few-Electron Double Quantum Dot with Fast rf Gate Sensors," *Physical Review Letters* **110**, 046805 (2013).
- [104] M. F. Gonzalez-Zalba, S. Barraud, a. J. Ferguson, and a. C. Betz, "Probing the limits of gate-based charge sensing," *Nature communications* **6**, 6084 (2015).
- [105] M. C. Cassidy, A. S. Dzurak, R. G. Clark, K. D. Petersson, I. Farrer, D. A. Ritchie, and C. G. Smith, "Single shot charge detection using a radio-frequency quantum point contact," *Applied Physics Letters* **91**, 222104 (2007).
- [106] H. D. Cheong, T. Fujisawa, T. Hayashi, Y. Hirayama, and Y. H. Jeong, "Impedance analysis of a radio-frequency single-electron transistor," *Applied physics letters* **81**, 3257 (2002).



- [107] K. Bladh, D. Gunnarsson, A. Aassime, M. Taslakov, R. Schoelkopf, and P. Delsing, “Noise performance of the radio-frequency single-electron transistor,” *Physica E: Low-dimensional Systems and Nanostructures* **18**, 91 (2003).
- [108] T. Duty, G. Johansson, K. Bladh, D. Gunnarsson, C. Wilson, and P. Delsing, “Observation of quantum capacitance in the Cooper-Pair transistor,” *Physical Review Letters* **95**, 206807 (2005).
- [109] B. J. Villis, A. O. Orlov, S. Barraud, M. Vinet, M. Sanquer, P. Fay, G. Snider, and X. Jehl, “Direct detection of a transport-blocking trap in a nanoscaled silicon single-electron transistor by radio-frequency reflectometry,” *Applied Physics Letters* **104**, (2014).
- [110] K. Ono, D. G. Austing, Y. Tokura, and S. Tarucha, “Current Rectification by Pauli Exclusion in a Weakly Coupled Double Quantum Dot System,” *Science* **297**, 1313 (2002).
- [111] M. Jung, M. D. Schroer, K. D. Petersson, and J. R. Petta, “Radio frequency charge sensing in InAs nanowire double quantum dots,” *Applied Physics Letters* **100**, 2 (2012).
- [112] M. D. Schroer, M. Jung, K. D. Petersson, and J. R. Petta, “Radio Frequency Charge Parity Meter,” *Physical Review Letters* **109**, 166804 (2012).
- [113] K. D. Petersson, C. G. Smith, D. Anderson, P. Atkinson, G. A. C. Jones, and D. A. Ritchie, “Charge and spin state readout of a double quantum dot coupled to a resonator,” *Nano Lett.* **10**, 2789 (2010).
- [114] A. C. Betz, R. Wacquez, M. Vinet, X. Jehl, A. L. Saraiva, M. Sanquer, A. J. Ferguson, and M. F. Gonzalez-Zalba, “Dispersively Detected Pauli Spin-Blockade in a Silicon Nanowire Field-Effect Transistor,” *Nano Letters* **15**, 4622 (2015).
- [115] M. F. Gonzalez-Zalba, S. N. Shevchenko, S. Barraud, J. R. Johansson, A. J. Ferguson, F. Nori, and A. C. Betz, “Gate-Sensing Coherent Charge Oscillations in a Silicon Field-Effect Transistor,” *Nano Letters* **16**, 1614 (2016).
- [116] E. Dupont-Ferrier, B. Roche, B. Voisin, X. Jehl, R. Wacquez, M. Vinet, M. Sanquer, and S. De Franceschi, “Coherent coupling of two dopants in a silicon nanowire probed by Landau-Zener-Stückelberg interferometry,” *Physical Review Letters* **110**, 1 (2013).
- [117] A. Crippa, R. Maurand, D. Kotekar-Patil, A. Corna, H. Bohuslavskyi, A. O. Orlov, P. Fay, R. Laviéville, S. Barraud, M. Vinet, M. Sanquer, S. De Franceschi, and X. Jehl, “Level Spectrum and Charge Relaxation in a Silicon Double Quantum Dot Probed by Dual-Gate Reflectometry,” *Nano Letters* **17**, 1001 (2017).
- [118] A. O. Orlov, P. Fay, G. L. Snider, X. Jehl, S. Barraud, and M. Sanquer, “Dual-Port Reflectometry Technique: Charge identification in nanoscaled single-electron transistors,” *IEEE Nanotechnology Magazine* **9**, 24 (2015).
- [119] A. Crippa, M. L. V. Tagliaferri, D. Rotta, M. De Michielis, G. Mazzeo, M. Fanciulli, R. Wacquez, M. Vinet, and E. Prati, “Valley blockade and multielectron spin-valley Kondo effect in silicon,” *Physical Review B* **92**, 035424 (2015).

- [120] A. Cottet, C. Mora, and T. Kontos, “Mesoscopic admittance of a double quantum dot,” *Physical Review B* **83**, 121311 (2011).
- [121] A. Stockklauser, V. F. Maisi, J. Basset, K. Cujia, C. Reichl, W. Wegscheider, T. Ihn, A. Wallraff, and K. Ensslin, “Microwave Emission from Hybridized States in a Semiconductor Charge Qubit,” *Physical Review Letters* **115**, 46802 (2015).
- [122] R. P. Riwar, B. Roche, X. Jehl, and J. Splettstoesser, “Readout of relaxation rates by nonadiabatic pumping spectroscopy,” *Physical Review B - Condensed Matter and Materials Physics* **93**, 235401 (2016).
- [123] R. Lavieville, S. Barraud, C. Arvet, C. Vizioz, A. Corna, X. Jehl, M. Sanquer, and M. Vinet, “Demonstration of Single Hole Transistor and Hybrid Circuits for Multivalued Logic and Memory Applications up to 350 K Using CMOS Silicon Nanowires,” *Advanced Electronic Materials* **2** (2016), 10.1002/aelm.201500244.
- [124] P. Clapera, S. Ray, X. Jehl, M. Sanquer, A. Valentian, and S. Barraud, “Design and Cryogenic Operation of a Hybrid Quantum-CMOS Circuit,” *Phys. Rev. Applied* **4**, 44009 (2015).
- [125] M. Bruel, “Process for the production of thin semiconductor material films,” (1994).
- [126] B. Roche, B. Voisin, X. Jehl, R. Wacquez, M. Sanquer, M. Vinet, V. Deshpande, and B. Previtali, “A tunable, dual mode field-effect or single electron transistor,” *Applied Physics Letters* **100**, 32103 (2012).
- [127] E. Dornel, T. Ernst, J. C. Barbé, J. M. Hartmann, V. Delaye, F. Aussenac, C. Vizioz, S. Borel, V. Maffini-Alvaro, C. Isheden, and J. Foucher, “Hydrogen annealing of arrays of planar and vertically stacked Si nanowires,” *Applied Physics Letters* **91**, 10 (2007).
- [128] J. Choi, Y. Mao, and J. Chang, “Development of hafnium based high-k materials—A review,” *Materials Science and Engineering: R: Reports* **72**, 97 (2011).
- [129] M. R. Visokay, J. J. Chambers, A. L. P. Rotondaro, A. Shanware, and L. Colombo, “Application of HfSiON as a gate dielectric material,” *Applied Physics Letters* **80**, 3183 (2002).
- [130] M. Houssa, L. Pantisano, L.-Å. Ragnarsson, R. Degraeve, T. Schram, G. Pourtois, S. De Gendt, G. Groeseneken, and M. Heyns, “Electrical properties of high- $\kappa$  gate dielectrics: Challenges, current issues, and possible solutions,” *Materials Science and Engineering: R: Reports* **51**, 37 (2006).
- [131] B. Voisin, V.-H. Nguyen, J. Renard, X. Jehl, S. Barraud, F. Triozon, M. Vinet, I. Duchemin, Y.-M. Niquet, S. de Franceschi, and M. Sanquer, “Few-Electron Edge-State Quantum Dots in a Silicon Nanowire Field-Effect Transistor,” *Nano Letters* **14**, 2094 (2014).
- [132] X. Jehl, B. Voisin, T. Charron, P. Clapera, S. Ray, B. Roche, M. Sanquer, S. Djordjevic, L. Devoille, R. Wacquez, and M. Vinet, “Hybrid metal-semiconductor electron pump for quantum metrology,” *Physical Review X* **3** (2013), 10.1103/PhysRevX.3.021012.

- 
- [133] M. Feldman, “Nanolithography: The Art of Fabricating Nanoelectronic and Nanophotonic devices and Systems,” in *Nanolithography: The Art of Fabricating Nanoelectronic and Nanophotonic devices and Systems*, edited by M. Feldman (Woodhead Publishing Limited, 2014).
- [134] E. Prati, M. De Michielis, M. Belli, S. Cocco, M. Fanciulli, D. Koteekar-Patil, M. Ruoff, D. P. Kern, D. A. Wharam, J. Verduijn, G. C. Tettamanzi, S. Rogge, B. Roche, R. Wacquez, X. Jehl, M. Vinet, and M. Sanquer, “Few electron limit of n-type metal oxide semiconductor single electron transistors.” *Nanotechnology* **23**, 215204 (2012).
- [135] Keysight, *The Parametric Measurement Handbook* (2014) p. 213.



# Appendix A

## Device fabrication

Samples fabrication take advantage of established and mature Complementary Metal-Oxide-Semiconductor (CMOS) technology. In particular we employed a derivative of Trigate Silicon-On-Insulator (SOI) platform developed at CEA-Leti [19], which in turn is a close relative to Fully Depleted Silicon-On-Insulator (FDSOI) technology. Devices are MOSFET or multi-gate variation of them. The key point of Trigate geometry is that the active area of a transistor is made by a narrow silicon nanowire (NW) surrounded by the gate on three sides. This nanowire is etched from the thin silicon layer of SOI and lays over the Buried Oxide (BOX) layer of substrate. All fabrication steps are performed in a 300mm top-down facility. This is great advantage, since the fabrication process is massively parallel and a large number of devices can be made. On our typical process, up to about 300 identical dies per wafer are produced. Also we can exploit the modern technological innovations in the microelectronics fabrications and tooling.

Feature patterning is mainly done by optical deep-ultraviolet (DUV) lithography. Critical layers are defined with standard 193nm ArF dry lithography; Critical Dimensions (CD, the smallest feature that can be drawn) of 80nm and a pitch of 170nm can be achieved. If a lower pitch is needed, e-beam lithography can be employed; however the writing time is way longer, so only small surface can be patterned. Typically the pitch is 65nm (so a spacing of 30-35nm) and the CD around 35nm.

### A.1 Fabrication steps

The fabrications starts on the substrate, which is a 300mm SOI wafer made by SmartCut technology [125]. It's made by a 775 $\mu$ m thick slightly boron doped silicon substrate, which provides the mechanical handling and stiffness. Given its low doping at low temperature it's an insulator and we need to shine light to make it conductive [126]. Over that lies the BOX,

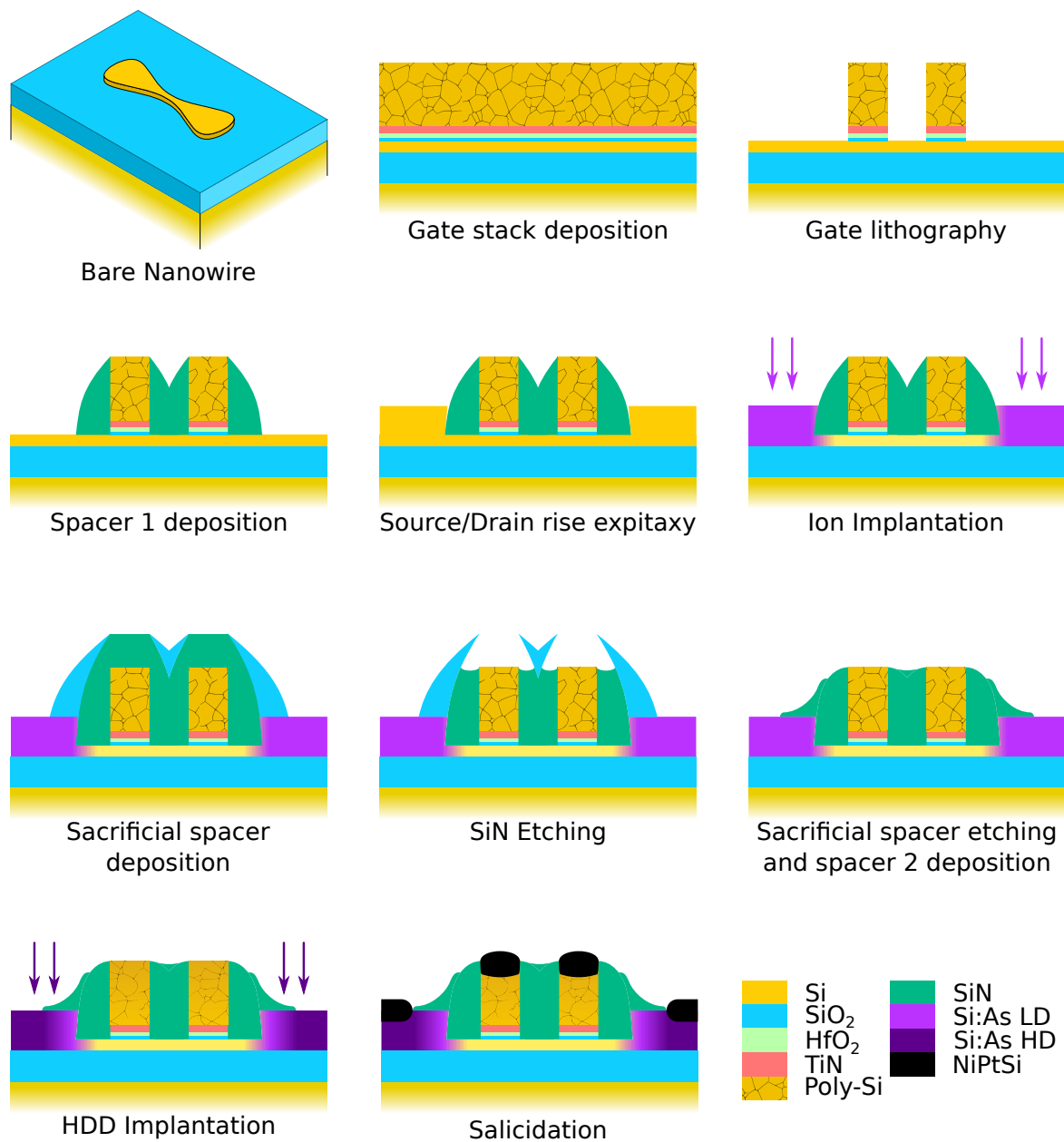


Figure A.1 Fabrications step

which is a 145nm thick layer of silicon dioxide. Finally on the top there is a 16nm layer of intrinsic high-quality silicon.

Initially the silicon is thinned down to 12nm or 8nm by plasma oxidation and subsequent deoxidation with hydrogen fluoride (HF). Then this layer is intentionally slightly doped to have few dopants or acceptors in the MOSFET channel, the so-called *channel doping*. The doping level is typically from  $5 \times 10^{17} \text{ cm}^{-3}$  to  $2 \times 10^{18} \text{ cm}^{-3}$  or either undoped. Phosphorus or arsenic are used for NMOS, while boron is used for PMOS. A spike annealing activate the impurities.

Subsequently the active area (ie. the nanowire) is patterned with DUV lithography. To achieve small NW diameter, after the lithography and before the pattern transfer with plasma, the resist is trimmed. Trimming is a partial etching (performed with Reactive Ion Etching, RIE) of the resist that shrink the dimension of a pattern. The thickness of resist is reduced, as well as the lateral dimensions of shapes. So the CD are lowered from 80nm down to 15nm. Nevertheless the pitch is unaltered and cannot be reduced with this technique. The shape is slightly altered, especially the corners are more rounded. Finally a plasma etch removes the silicon regions not covered by the resist creating in this ways the nanowires. The engraving stops at the BOX interface or slightly below. Nanowires lies over the buried oxide and they are isolated one each other by that; this is called *mesa isolation*. Nanowires are drawn to have their axis aligned to the [110] direction of the silicon.

The cross section shape of the nanowire influence the gate cross-section shape as well. If it's square or rectangular (so with strong 90° corners) it will be a *Tri-gate* or *Pi-gate*, depending on the overetch of the BOX (see figure A.2). Otherwise, if it's rounded with a hydrogen annealing [127], it will be an *Omega-gate*. This has a strong influence on the charge confinement at low temperature.

Then the gates are created. The gate stack is composed by an insulating layer and a metallic layer above that. The insulator is an hafnium-based oxide, which is a *high-k oxide*, where the dielectric constant is larger than the silicon dioxide. In our case it's a 1.9nm thick ALD deposited  $\text{HfO}_2$  ( $\epsilon_k = 22 - 25$  [128]) or either  $\text{HfSiON}$  ( $\epsilon_k = 14$  [129]). Unfortunately the high-k/silicon interface is not optimal [128] [130] and especially at low-temperature it can give rise to noisy environment due to remote coulomb charge traps at the interfaces [131]. For this reason a layer of thermally grown  $\text{SiO}_2$  is interposed between the silicon and the high-k. It create an excellent interface with the nanowire and keep away the offset charges of the high-k. The metal layer is composed by 5nm of ALD deposited TiN and about 50nm of poly-silicon. On the top a 30nm thick layer of SiN acts as hard mask. This stack is patterned and etched in a similar way as the nanowires. The etching is performed with chemicals selective to each layer of the stack and thus is self-limiting. To achieve small pitches, e-beam

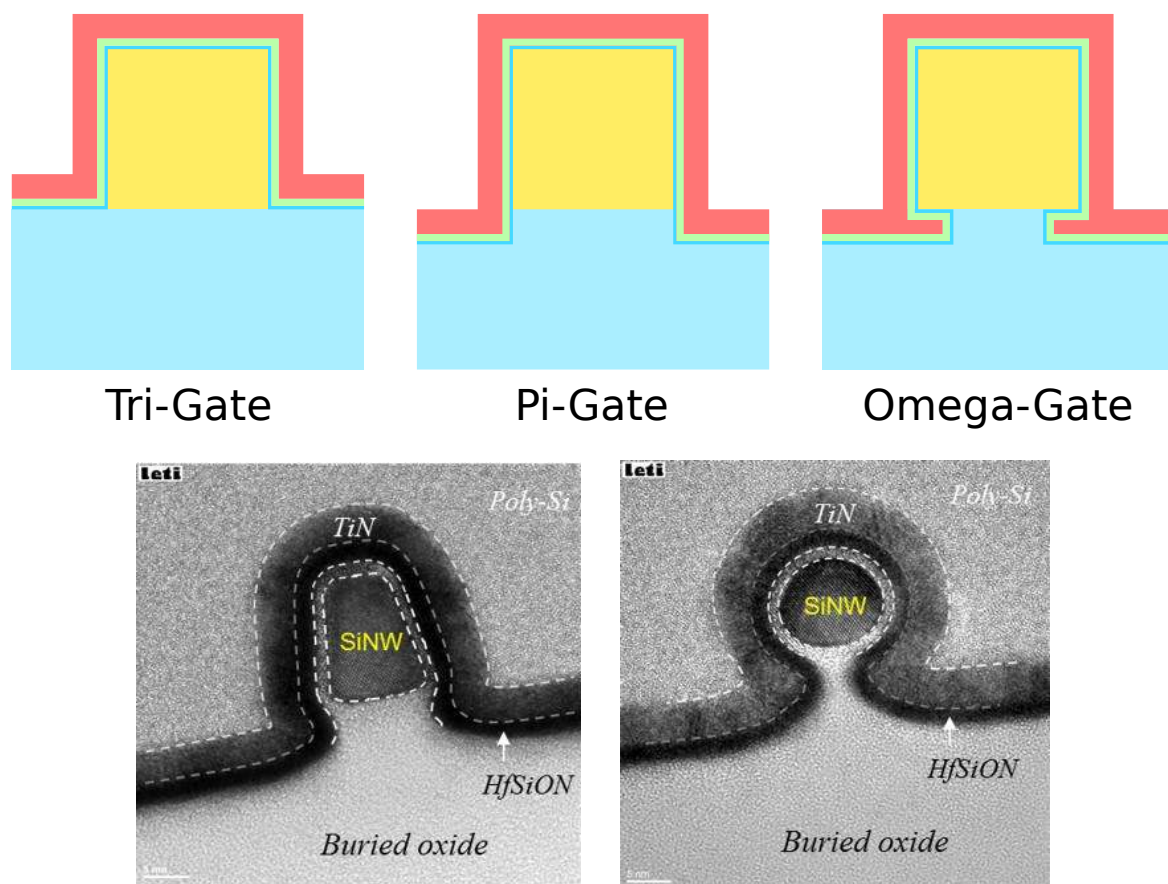


Figure A.2 Different gate shapes



lithography can be used instead of DUV lithography (see A.2)

Now the transistor has its channel and control gate(s) but lacks low-resistance source/drain, since the silicon in the access area is intrinsic. Ion implantation is used to dope the contacts, and the gates are used as a mask to prevent implantation in the active area (*self-aligned gates*). By choosing the chemical species for ion, we can get an NMOS (using arsenic and phosphorus) or a PMOS (with bore).

Gates alone are not sufficient to completely protect the active area, since ion implantation slightly overcomes the corners. To avoid that, self-aligned sidewall spacers are deposited on the sides of the gates. They are made by SiN, which greatly reduces ion penetration. Their dimension is crucial for the creation of the tunnel barriers and quantum dots [35]; in our case they were 25-30nm long, but they can be as short as 9nm or as long as 40nm. With several gates in series, they are crucial to protect the nanowire section between the two gates, otherwise a metallic island (and then an SET) will be created in between [51] [132].

In order to further decrease the access resistance and facilitate the implantation, the thickness of exposed silicon that constitutes the source and drain is increased by 18nm with a selective epitaxy. Only the contacts area is raised, the head of the polysilicon gates is still protected by the nitride layer, which is subsequently removed. The removal of SiN is done after the deposition of a sacrificial oxide spacer, to protect the sidewall nitride spacers from etching. Such spacer is then removed.

The ion implantation is done in two steps, a first low-dose implantation (Low-Doped-Drain, LDD) followed by a high-dose one (High-Doped-Drain, HDD). In between another spacer is deposited. In this way there is smooth gradient of the doping profile to reduce serial resistance, parasitic capacitances and hot-electrons injections. The final doping profile is non-overlapping, with a strong dependence on the spacer size (see B) and the annealing process.

To further improve the contact resistance and to avoid the creation of Schottky junctions and thus have good ohmic contacts, the surface of the contacts is metalized. The metal is an alloy formed by the reaction at high temperature of a deposited metal with the silicon. This kind of alloy are called *silicides* or even *salicides* (self-aligned silicides). In our case the final metal is NiPtSi.

All these steps are part of the front-end-of-line (FEOL) fabrication, which deal with the fabrication of the CMOS devices. It's followed by a commercial copper-based back-end-of-line (BEOL) process, which creates the interconnections and the bonding pads and encapsulate the devices in a protective glass, .

## A.2 E-beam/DUV hybrid lithography

E-beam Lithography (EBL) is a common direct-write lithography tool used to pattern very small features. Ultimate resolution is down to few nanometers [133], although in practice with standard resists, the resolution is about 30-35 nm. Moreover, given that it's a direct write tool, it's more flexible compared to optical lithography; new features and modifications can be made between each iteration of fabrication without re-creating a new set of mask. On the downside it's way slower: its throughput is in the range  $0.0001\text{-}1.0\text{ cm}^2/\text{s}$  compared to  $20\text{-}30\text{ cm}^2/\text{s}$  of optical lithography. Thus it's employed only to write small features on critical layers.

In our case it has been used only on the gate level, in tandem with the DUV lithography, in the so-called *composite EBL/DUV lithography*. In these scheme, some dies are patterned with EBL, and the other with optical lithography. The strategy used here is nicknamed *litho-etch-litho-etch*, meaning that a lithography step (first DUV than EBL) is followed by a etch to transfer the pattern to the gate layer. In this way, each lithography can use its own resist and trim rule. The DUV resist is negative, meaning that the exposed area is left un-etched, so the mask should be the positive of the desired pattern. E-beam dies are fully exposed without mask to be protected from etching. On the contrary, EBL resist is positive. Unexposed dies (DUV ones) are protected and not etched. For the devices on EBL dies, the exposed area should be the negative of the desired pattern. While this is easy to achieve in optical lithography, the same is not true with e-beam due to writing speed limitation. Only a small area around the sample get exposed, so in the end, a large area of the die is left with the gate level un-etched. This is not an issue, but it create a parasitic capacitance with the bonding pads that has to be taken into account and exploited when doing RF measurements (see section 2.1.1).

At the end of the process there two classes of dies: the “DUV” ones (green in figure A.4a) with mostly devices with a simple geometry (like single gate MOSFETs) and the “e-beam” ones (blue ones) with dense multigate samples.

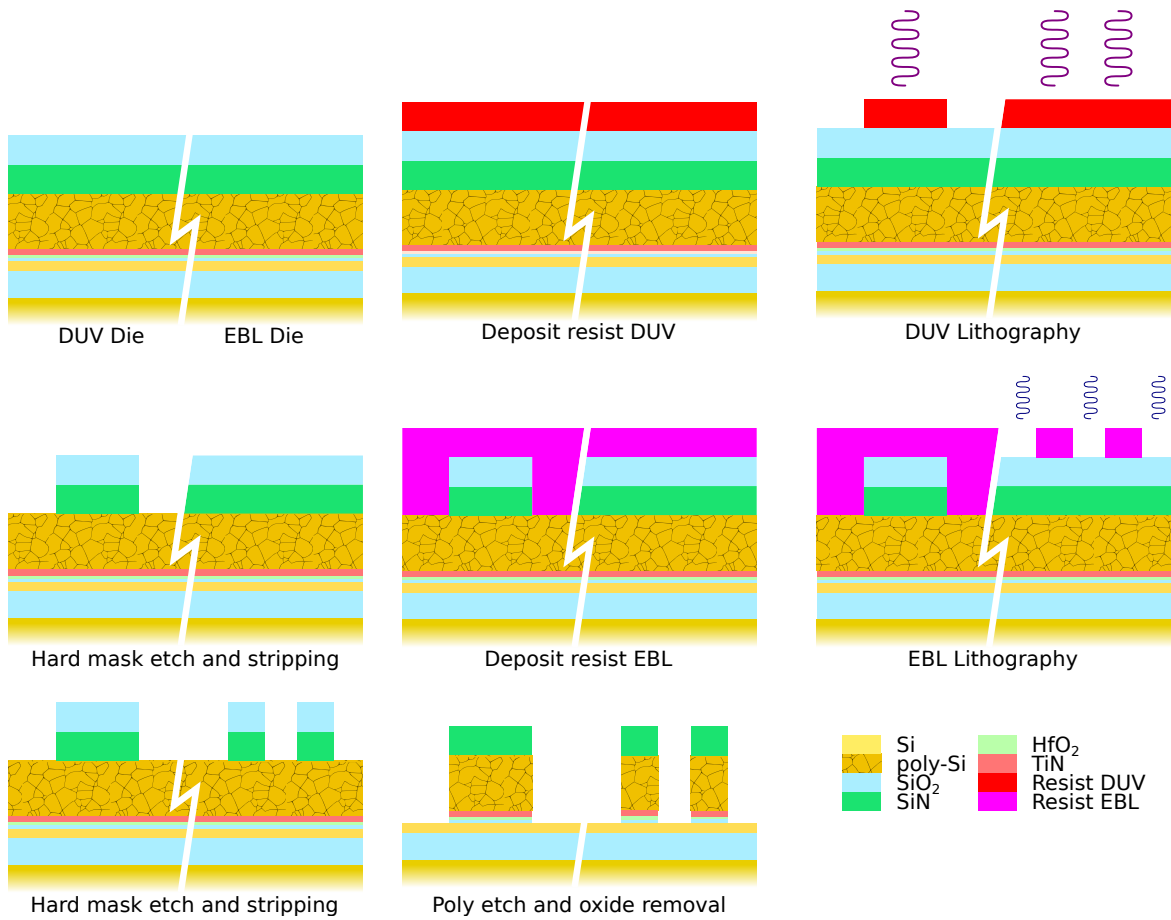


Figure A.3 Composite lithography steps

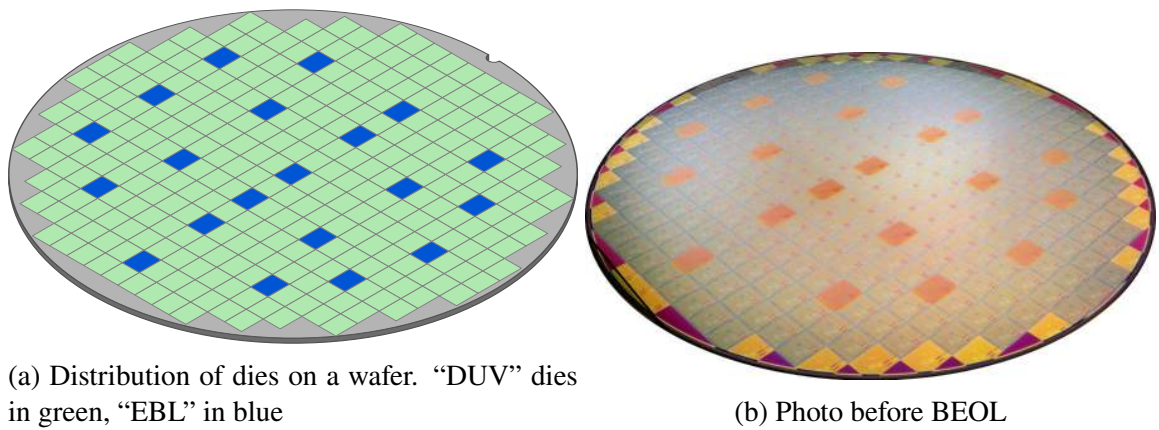


Figure A.4 300mm wafer with composite EBL/DUV lithography



# Appendix B

## Device selection

Devices are produced in batches of 25 wafers. While the fabrication recipe for a given batch is basically the same, usually not all these wafers are equivalent. Some steps are performed differently, in order to have a larger choice. Although these variations may seem minor, they impact significantly the behavior at low temperature. These variations are called *technical splits*. In table B.3 technical splits for batch “SiAM-2” are reported. When selecting a wafer for a specific, there are several key parameters to look at:

- **FET Kind** The first obvious thing to look at, is the FET kind, either NMOS or PMOS. Wafers can be either *Unipolar* or “CMOS”. When it’s unipolar, all the devices are of the same kind; devices are NMOS when LDDN/DSN implantation is performed, PMOS with LDDP/DSP. In full CMOS wafers, both implantations are performed, with a specific mask to determine the kind of each device. This is needed for CMOS circuits, is less useful for isolated devices, like the ones considered in this thesis.
- **Channel doping** The channel of the FET could be slightly doped for researches on dopants. If a system with only quantum dot is preferred, undoped channel is better.
- **CD ZACT** The width of the channel is roughly given by the patterns on the optical mask, and can be finely tuned during the lithography with the resist trimming. Narrower channels (down to 10-15nm) are advised for system with dot in series, in order to have them smaller are more predictable. Wider channels (up to 50nm) are suggested for face-face geometries when dots are in parallel, otherwise the channel might be smaller than the pitch of the gates and one of the gates could not cover the active area (see figure B.1).
- **Gate oxide** In the gate stack, an 0.8nm thick layer of SiO<sub>2</sub> is used as interface between the nanowire and the high-k oxide. At low temperature the charges trapped in the

high-k material can be a source of noise and instability, so the thickness of the silicon dioxide can be increased up to 2.5nm to mitigate this effect. Gate leakage current is usually lowered to undetectable values. The downside is that the electrostatic control is lowered by the greater thickness.

- **First spacer size** Spacer size is a key parameter for a series of aspects. The first one is its role in the formation of tunnel barriers in tandem with the modulation doping [35] [131]. Long enough spacers (roughly 16nm, see supplementary material of [131], “Creating quantum dots using longer spacer”) are needed to create barrier underneath of the spacers and a dot localized on the gate region. Otherwise localization of dot(s) is mostly driven by surface roughness. If the spacers are too long (roughly 30-40nm), the barrier may be too opaque to observe first-electron tunnel events [134]. Conversely, very narrow spacers or no spacers at all, can be used to create a system extremely coupled to the leads [28]. If the system is extremely scaled and/or dominated by surface roughness/offset charges, these rules of thumbs may not apply (see [29] and chapter 1).

In multi-gated devices, spacers are crucial to properly protect the nanowire from ion implantation. For example, in a double gate in series geometry, if the spacer size is less than half of the gate distance (so, more than 15-18nm for a typical gate distance of 30-35nm), the region between the gates will be implanted during leads formation (see figure B.2 b). In this case, at low temperature the system will behave as a metallic SET with tunable barriers [132] [51]. If the spacers are larger than this threshold value, the region between the gates will be undoped, and can act as a tunnel barrier between two dots accumulated under each gate. Lengths of 24-30nm have been proved to provide a good protection of the inter-gate region and a reasonable tunnel barrier with the leads (see figure B.2 a).

In addition to the spacer size, all of these characteristics can be further tuned omitting the LDD implantation and doing only the HDD. In this case the barriers are longer and then more opaque.

- **Second spacer and silicide** Spacer two could be omitted. Usually the area between two gates with a small pitch is protected from salicidation by this spacer. By removing it, an intentional metallic island is formed between the gates. This option is used with short spacers and a so-called “soft-silicide”; the latter one is less aggressive than the standard one to avoid short-circuits in the channel.

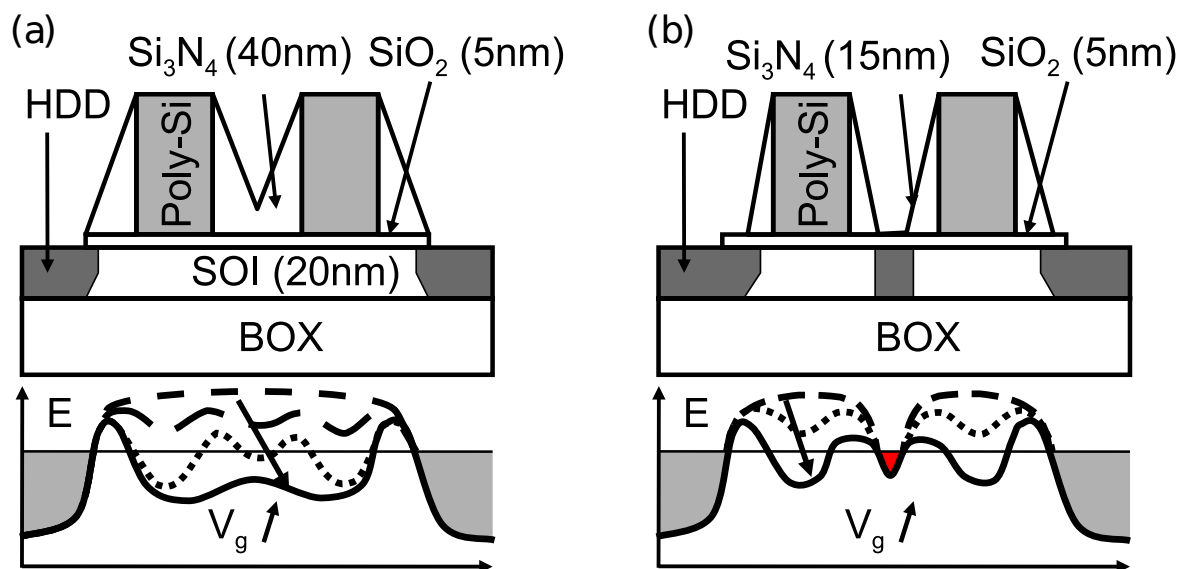


Figure B.2 Implantation profile for long (a) and short spacers. Taken from [28]

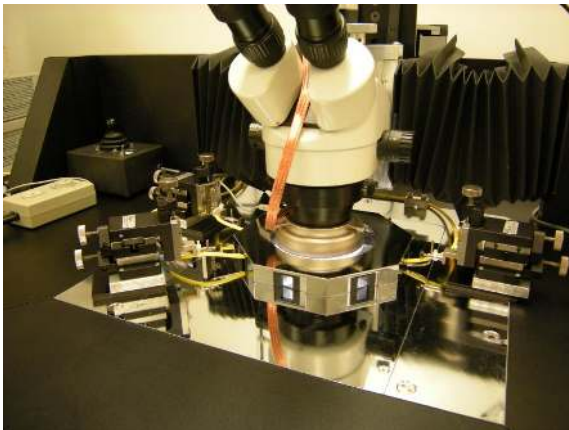
Siam 2 - T14S0788																									
Wafer	1	2	3	4	5	6	7	8	9	17	18	19	20	21	22	23	24	25							
e-beam mark																									
Undoped channel																									
NMOS channel doping ~2x10 <sup>18</sup> cm <sup>-3</sup> (Phosphorus)																									
NMOS channel doping ~2x10 <sup>18</sup> cm <sup>-3</sup> (Arsenic)																									
PMOS channel doping ~2x10 <sup>18</sup> cm <sup>-3</sup> (Boron)																									
PMOS channel doping ~5x10 <sup>17</sup> cm <sup>-3</sup> (Boron)																									
CD ZACT ~18nm																									
CD ZACT ~50nm																									
Gate stack (SiO <sub>2</sub> 2.5nm/HfO <sub>2</sub> 1.9nm/TiN 5nm)																									
CD POLY DUV ~20nm																									
CD POLY e-beam ~30-35nm																									
First spacer size ~9nm																									
First spacer size ~15nm																									
First spacer size ~30nm																									
Epitaxy 18nm																									
LDDP																									
LDDN																									
Second spacer																									
DSP																									
DSN																									
Silicide "standard"																									
Silicide "soft"																									
No Backend																									

Figure B.3 Technical splits for batch "Siam2" (T14S0788). Wafers from 10 to 16 were scrapped.

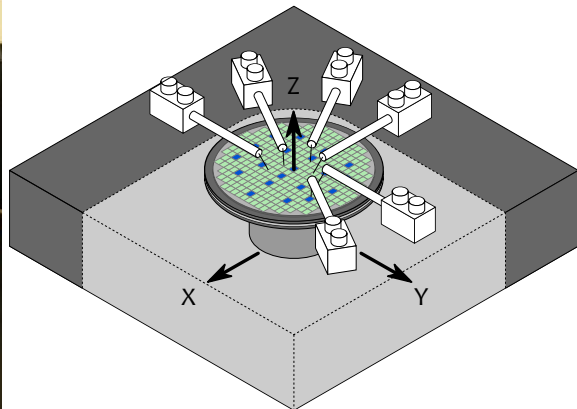
## B.1 Probe station

After a wafer and a sample geometry has been chosen, samples can be tested at room temperature to choose the best candidate for low-temperature measurements and infer some general behavior. On a single wafer, the same geometry is implemented identically several times (from a minimum of 20 for devices made with e-beam A.2 up to several thousand for simpler ones). Measuring manually all the devices could be an difficult task; to overcome this issue, samples are tested in a semi-automatic 300mm probe station B.4.

The probe station is made by a movable plate (chuck) that host the wafer. Its movement are servo-controlled and it can move along all the three axes with a precision of few micrometers. On top of that, there are the needle assemblies, which holds in place the needles that contacts the pads of the samples. Once the needles are put in place, the wafer is automatically moved to touch and then measure each device. The measurements are performed by a parametric analyzer [135]. This instrument has 6 Source/Measurement Units (SMU), each one is capable to apply a voltage(current) bias to a port and read the current(voltage). The whole system is shielded and uses triaxial cables and interconnections. In this way, we can perform low-current low-noise measurement with a noise level down to 0.1 pA. We measure the IV characteristics for each device up to 4 gates (plus two leads); each gate or lead is biased and its current is read, thus providing a complete picture of the currents that flow in the system. A gate (or less common, the drain) is swept while others voltages are kept constants. The set of measurement performed on each device depends on the geometry of the device and on the technical split, and it's explained when relevant.



(a) Photo



(b) Schematics

Figure B.4 Our probe station



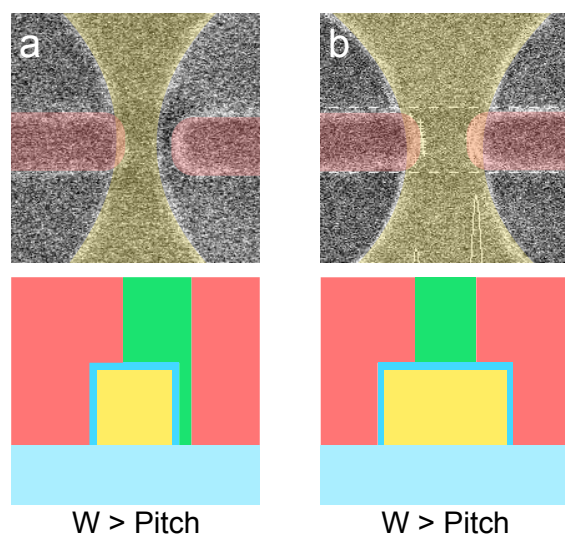


Figure B.1 Cross section of a face-face device for narrow (a) and wide nanowire (b). In the first case, not both gates cover the NW

